N84-34694

CONTRIBUTION TO THE PERFORMANCE DETERMINATION OF MICROJETS

Dieter Hayn

1. Report No. NASA TM-77730	2. Government Accession No.	3. Recipient's Catalog No.
4. Title and Subtitle CONTRIBUTION TO THE PERFORMANCE OF MICROJETS		5. Report Date September, 1984
		6. Performing Organization Code
7. Author(s) Dieter Hayn		8. Performing Organization Report No.
		10. Work Unit No.
9. Performing Organization Name and Address SCITRAN Box 5456 Santa Barbara, CA 93108		11. Contract or Grant No. NASw 3542
		12. Type of Report and Period Covered Translation
12. Sponsoring Agency Name and Address National Aeronautics and Space Administration Washington, D.C. 20546		14. Sponsoring Agency Code

15. Supplementary Notes

16. Abstract

Theoretical investigations are made on the performance of microjets, and a description is given of experiments with micropropulsion units to correlate the results obtained in the first part of the report. Execution of performance measurements is discussed, and error calculations are presented.

17. Key Words (Selected by Author(s))	18. Distribution Statement Unclassified and Unlimited

19. Security Classif. (of this report) Unclassified	20. Security Classif. (of this page) Unclassified	21. No. of Pages	22. Price

CHAIR FOR SPACE TECHNOLOGY
TECHNICAL UNIVERSITY MUNICH

CONTRIBUTION TO THE PERFORMANCE
DETERMINATION OF MICROJETS

Dieter Hayn

Born June 17, 1950
in Montabaur

Complete copy of the DISSERTATION approved by the Faculty
for Mechanical Engineering of the Technical University
Munich to obtain the academic degree of

DOCTOR IN ENGINEERING

P R E F A C E

The work here reported was performed at the Chair for Space Technology of the Technical University of Munich.

I would like to express my special gratitude to my professors, the Chair's Titular Prof. Dr. Eng. Harry O. Ruppe and Prof. Dr. Eng. Robert H. Schmucker, without whose example and support this work would never have been performed.

My gratitude goes also to Chair C for Thermodynamics, Prof. Dr. Eng. Edgar Winter, for making a laboratory available.

I would furthermore like to thank my colleague Rainer Ondrusch for his extensive support in building the cold gas propulsive unit; graduate engineer Ulrich Weishaupt for his decisive support in the development in the data gathering system; the Gerold Wendl company for their generous tool provision; the Philipp Basche company for their excellently performed galvanizations; and all those colleagues and collaborators whose so energetically assisted me. Finally, I thank my friend, graduate engineer Walter Gehringer, who first as student and after his graduation as a free collabora-tor for years contributed substantially to the success of the task here undertaken.

<div align="right">Dieter Hayn</div>

TABLE OF CONTENTS

SYMBOLS AND ABBREVIATIONS USED

A   = Surface area

a   = velocity of sound

b   = characteristic width

bl   = boundary layer

C_F = thrust coefficient

c   = velocity

c*   = characteristic velocity

c_{eff} = effective discharge velocity

c_f = thrust stress coefficient

F   = thrust; force

GEO   = geostationary orbit (24 hour orbit)

g_0 = acceleration due to gravity

Hz   = vibrations per second

h   = enthalpy

i   = inclination

I   = impulse

LEO   = low Earth orbit

M   = Mach number

m   = instantaneous mass of the gas storage container

m_{mol} = molecular weight

$\dot{m}$ = Mass throughput

N_2 = molecular nitrogen (here purified)

Nu   = Nusselt number

n   = Direction of the normal (perpendicular) to a surface

ODE   = one-dimensional shifting equilibrium

ODF   = one-dimensional frozen equilibrium

ODK   = one-dimensional kinetic flow

Pr   = Prantl number

p   = pressure

R   = Special gas constant

$\Re$ = general gas constant

Re   = Reynolds numerator

St   = Stanton number

6

s	= coordinate tangential to the wall; entropy
T	= temperature
TD	= two-dimensional
TW	= propulsive plant
t	= time
v	= velocity
x	= nozzle axis coordinate
y	= velocity distribution coordinate
z	= altitude coordinate

Subscripts

acc	= acceleration
ax	= axial
c	= combustion chamber
c_D	= constriction coefficient; throat throughput coefficient
ch	= characteristic
D	= drag
1-d	= one-dimensional
2-d	= two-dimensional
del	= delivered
e	= end cross-section; end condition
F	= thrust
i	= initial condition
inj	= injector
lam	= laminar
n/v	= inviscid
r	= radial
sp	= specific
t	= throat
tan	= tangential
th	= theoretical
turb	= turbulent
ver	= vertical
vis	= viscous

W   = balance

∞   = environment condition (vacuum chamber or laboratory)

Greek letters

α = heat transfer coefficient

α_e = exit cone angle (divergent portion)

α_i = exit cone angle (convergent portion)

γ = isentropy exponent (c_p/c_v)

δ = boundary layer thickness

δ^* = displacement density

δ_H = energy density

ϵ = surface ratio; eccentricity

η = viscosity

Θ = impulse loss density

λ = thermal conductivity

λ = geographical longitude

μ = micro (10^{-6})

ν = cinematic viscosity

ρ = density

τ = thrust stress

χ = compressibility

ψ = discharge coefficient

Ω = rising node

ω = rotation rate

∂ = differential operator

1 INTRODUCTION

At the present time, the areas of application of communications
satellites include national and international telephone connec-
tions, long-distance data transmission, radio and television
signals, navigation for ships and aircraft, meteorological
monitoring, satellite tracking and uses in development tasks.

The optimum orbit is determined by the task posed. Synchronous
satellites occupy an exceptional position, since they travel in
their orbit at the same angular velocity as Earth (geostationary
orbits). If such an orbit occupies the equatorial plane, then
the subsatellite point remains always over the same location
on the Earth's surface: synchronous satellite.

But conditions along a satellite orbit are not as ideal as one
could hope. Reality is far removed from the assumption of a
dynamic two-body system that can in addition be represented by
point masses. Hence a satellite suffers a series of distortions
such as those caused by
- atmospheric resistance
- anisotropies in Earth's gravitational potential
- gravitational effects of other masses, especially the
  sun and the moon
- radiation pressure due to direct solar irradiation,
  Earth radiation and albedo, as well as the satellite's
  own radiation
- errors in the application of the control impulses
- discharge of refuse, degassing, uncontrolled fuel re-
  leases
- feedback coupling with attitude control systems
- interactions with the environment (cosmic radiation,   /2
  the Earth's magnetic field, etc.)
- relativistic effects.

---

* Numbers in the right margin indicate foreign pagination

Under the effect of these disturbances the satellite is not going to maintain its anticipated orbit. In the case of geostationary satellites this means that the subsatellite point no longer remains stable in one location, but wanders in an uncontrolled manner.

Among the disturbing effects listed above, three have proven to be predominant, for geostationary satellites:

1) Anisotropy of the Earth's potential
2) Solar radiation pressure
3) Gravitational effects of the sun and the moon

Starting from the orbit distortions caused by these three influences, the velocity adjustment can be calculated that is necessary to return to the initial position, once the satellite has achieved a known deviation from that position [13,34,39,42-44,66, 79,81,82, 85-87,93,98,110,129,131,152,164,166,173-175).

The Tables below provide a rough overview on the order of magnitude of the gravitational distortion due to other bodies, on the geostationary orbit, and of that due to solar radiation pressure:

TABLE 1 GROSS ACCELERATIONS DUE TO GRAVITATIONAL FORCES, OF BODIES IN THE PLANETARY SYSTEM, ON A SYNCHRONOUS SATELLITE

	Acceleration (m/s^2)
Sun	5.931×10^{-3}
Mercury	2.546×10^{-9}
Venus	1.898×10^{-7}
Earth	2.244×10^{-1}
Earth's moon	3.320×10^{-5}
Mars	6.951×10^{-9}
Jupiter	3.201×10^{-7}
Saturn	2.324×10^{-8}
Uranus	7.816×10^{-10}
Neptune	3.708×10^{-10}
Pluto	9.626×10^{-12}

TABLE 2 COMPARISON OF THE PERTURBING ACCELERATIONS DUE TO SOLAR RADIATION PRESSURE AND DUE TO THE GRAVITATION OF THE SUN AND MOON

Disturbance	Acceleration (m/s^2)
Solar gravitation	6.40×10^{-7}
Grav. due to moon	2.44×10^{-6}
Solar wind	
A/m = 2.05 m^2/kg	6.25×10^{-6}
4.10	1.25×10^{-5}
6.40	1.95×10^{-5}
20.50	6.25×10^{-5}

The distortions mentioned are calculated with the aid of the
variation in orbit elements, even though at point 1 the validity
of the numerically determined results is limited, since the
higher terms describing the Earth's potential field are affected
by large uncertainties. The Earth's potential anisotropy and the
sun's radiation pressure essentially cause distortions only in
the orbital plane, while the influence on changes in inclination
in relation to point 3, above, can be neglected.

The consequence of equatorial ellipticity is a periodic motion
around one of two stable points of the orbit, which are found on
an extension of the equatorial ellipse's smaller semi-axis in
both directions, at approximately 57° E and 123° W of geograph-
ical longitude. The largest distortions occur at a satellite
position 45° away from such a stable point, attaining a radial
deviation of ±41.7km and an overall E-W deviation of 90°. The
distortion's period is approximately 580 days. Due to the Earth's
flattening, the radius of a synchronous orbit is increased
marginally, by approximately 0.5 km. However, this is not relevant
to orbit control.

Orbit control becomes necessary when the satellite has reached
a certain angular distance from its desired position. The return
is accomplished by means of a classical Hohmann transition. The
necessary velocity demand is independent of the number of control
maneuvers but depends on the satellite's initial position with
respect to the closest stable point. If this distance is 45°,
then the velocity demand attains a maximum of

$$\Delta v_{pot} = 5.17 \ m/sec/yr.$$

How large the distortion due to solar wind results for the
satellite depends on the ratio of its cross-sectional area A
and its mass m.

For A/m = 10^{-3} m^2/kg, the maximum angular deviation from an ar-
bitrary initial point is $\Delta\lambda$ = 0.25° and a maximum radial deviation

is r = 17.7 km. If an angular deviation of 0.1° is allowed, as
is customary with current communications satellites, then a
yearly velocity demand of

$$\Delta v_{sol} = 3.75 \text{ m/sec/yr}$$

must be satisfied.

The gravitational forces of the sun and the moon (point 3)
cause a distortion normal to the orbit's direction that becomes
manifest as a change in inclination. This distortion has a period
of p = 53.6 yr and a maximum deviation of 14.7 degrees. The
initial change of inclination occurs at $\Delta i = 0.865°$/yr. Applying
a simple impulse, after a certain time and angular change the
satellite is returned to its old position. During a five-year
mission, with a permissible inclination change of 0.25°, the
velocity demand is

$$\Delta v_{grav} = 48.55 \text{ m/sec/yr}.$$

By applying the "phase angle technique" this value can be reduced
to

$$\Delta v_{grav} = 45.85 \text{ m/sec/yr}.$$

Normally orbital control is accomplished by means of chemical
propulsion systems. This does not apply to the attitude control
of geostationary satellites, which generally are equipped with
a combined system of mechanical devices (gyroscopes) and reaction
equipment. For this reason it is not possible to provide a
precise value for the velocity demand for attitude control. At   /6
a permissible deviation of 0.1° a realistic value of

$$\Delta v_{att} = 1 \text{ m/sec/yr}$$

may be assumed.

Thus, if a satellite is on a weakly elliptical orbit of inclination i = 0, on a synchronous Earth orbit, with an allowed longitudinal deviation of 0.1° and a 0.25° allowed lateral deflection, then a yearly velocity demand of at least

$$\Delta v_{tot} = 55.77 \text{ m/sec/yr}$$

must be provided for, assuming the orbital distortions are additive, in regard to the Δv due the sun, moon and Earth.

The requirement for high precision in maintaining a satellite's orbital position leads to the installation of orbit and attitude control systems.

Orbit control compensates for center-of-mass distortions, while the function of attitude control is to insure that the satellite retains its alignment with a certain target point. A system that satisfies both functions is highly desirable, but this goal has not been achieved, as yet.

In recent years a number of chemical and electrical [21,92,151] propulsion systems have been developed (as well as gyroscope systems for attitude control) and successfully installed in operational satellites. Many others are still in the planning stage. Consideration was also given to using the solar wind or the light pressure for orbit and attitude control. The extensive activities precisely in the filed of control are not surprising, /7 since due to the high cost of space travels any possibility for savings must be taken advantage of.

One look at the basic equation of rocketry, $\Delta v = c_{eff} \cdot \ln (m_o/m_e)$ makes it very clear that for a given velocity demand and minimization of the fuel mass $(m_o - m_e)$, the highest possible exhaust velocity must be adopted. However, the consequent demand for the use of stable two-component systems of intermediate energy meets a series of technological restrictions: the required control

14

precision of the satellite with regard to orbit and attitude leads to the application of a large number of correction maneuvers with individual burning durations (typically 10,000 per year). Simultaneously, in order not to reduce the operating time per propulsion impulse to unrealistically brief periods of time, the propulsion unit's thrust must be correspondingly low. While for N/S corrections two-component systems can still be used (for instance, MBB propulsion unit at 10 Newton; I_{sp} = 290 sec), there are limits on miniaturization in the range of 0.5 to 2 N. Today, N_2H_4 single-component fuel systems are used here (without heating, I_{sp} = 230 sec; with electric heating: I_{sp} = 295 sec). Even smaller thrusts (50 mN), as required by precision attitude control, are accomplished by means of cold gas propulsion units (for instance, He of GN_2 [gaseous N_2]), since even the catalytic hydrazine devices can not be arbitrarily miniaturized. The low specific impulse of the engines (for nitrogen, typically 70 sec) forces an optimization of them with respect to combustion chamber pressure, expansion ratio, number of operating periods and overall consumption.

It is the purpose of this investigation to provide a contribution in this regard.

During the execution of the PAEHT study [56-63], the lack of computer programs adequate to precise performance prediction of chemical rocket propulsion units became very clear, in Europe [2,6,10,18,32,36,37,48,76,77,83,85,86,88,109,116,120,121,130, 132,137,138,148,149,156,162]. The programs developed in the US /8 under the superordinate concept JANNAF Procedures (ODE, ODK, TDK,BLIMP) could be obtained but were only partially usable (not sufficiently) in Europe [16,22].

For these reasons the current study was initiated at the conclusion of the studies performed for the PAEHT Project by the Chair for Space Technology of the Technical University Munich.

15

The first main portion of the task consisted in the development of a simplified, explicit procedure for performance prediction, in the foreground, and the comparison with available theoretical results from the procedures mentioned above. On the basis of these results, the final objective was a collection of easily manipulated estimation formulas, such as those required in the design of rocket propulsion plants. Naturally, this also requires the corresponding comparisons with measured values. However, during the course of the studies already mentioned, considerable gaps were found also in the area of reliable, available performance measurement values for the case of small propulsion units as they are particularly in the foreground, here.

This gap is partially closed by means of the test program related to cold gas propulsion units, presented in Section 2.

2.1 Prediction by extrapolation of data from implemented propulsion units

There are two methods, in principle, for the prediction of performance parameters (not only of propulsion units) of future systems: extrapolation, starting from data of actually implemented equipment, or by determining the physical laws and interactions that govern the individual components.

The first of these requires extensive data collections for implemented systems, including parallel developments of different devices. Only thus can hasty judgements be prevented. The advantage of this way is that it is not necessary to delve very deeply into the individual systems and the physical laws that govern them, provided it is assured that the groups or companies participating have or had available the necessary experience. As applied to the chemical propulsion units (more especially, of low thrust) currently at the focus of our interest, however, the following serious problems occur, which we shall mention here only in terms of keywords:

- large numbers of different concepts
- few parallel developments
- To date, no large areas have been covered; rather, almost always special applications are placed in the foreground of a given development
- large differences in the technical implementation
- performance differences among participating groups
- insufficient documentation of the results.

For this reason we have preferred following the second way.

2.2 Performance prediction by determination of individual losses

The starting point for the determination of individual losses in a rocket propulsion unit is the zero-loss, one-dimensional "shifting equilibrium" flow [ODE], whose performance values represent the upper theoretical limit. It is assumed that the gas composition corresponds in each case to the pressure and temperature conditions during expansion in the nozzle, and that the necessary reactions occur without delay time. The energy equation provides the isentropic exhaust velocity:

$$I_{sp,ODE,vac} \, g_0 = \sqrt{2(h_c - h_e)} \quad \text{with} \quad v_c = 0 \rightarrow \sqrt{2(c_{p,c} T_c - c_{p,e} T_e)} \tag{1}$$

However, in the real flow a series of performance-reducing factors occur, as a consequence of departure from the ideal condicions, $I_{sp,ODE,vac}$ (see also Figures 1, below and 2.1).
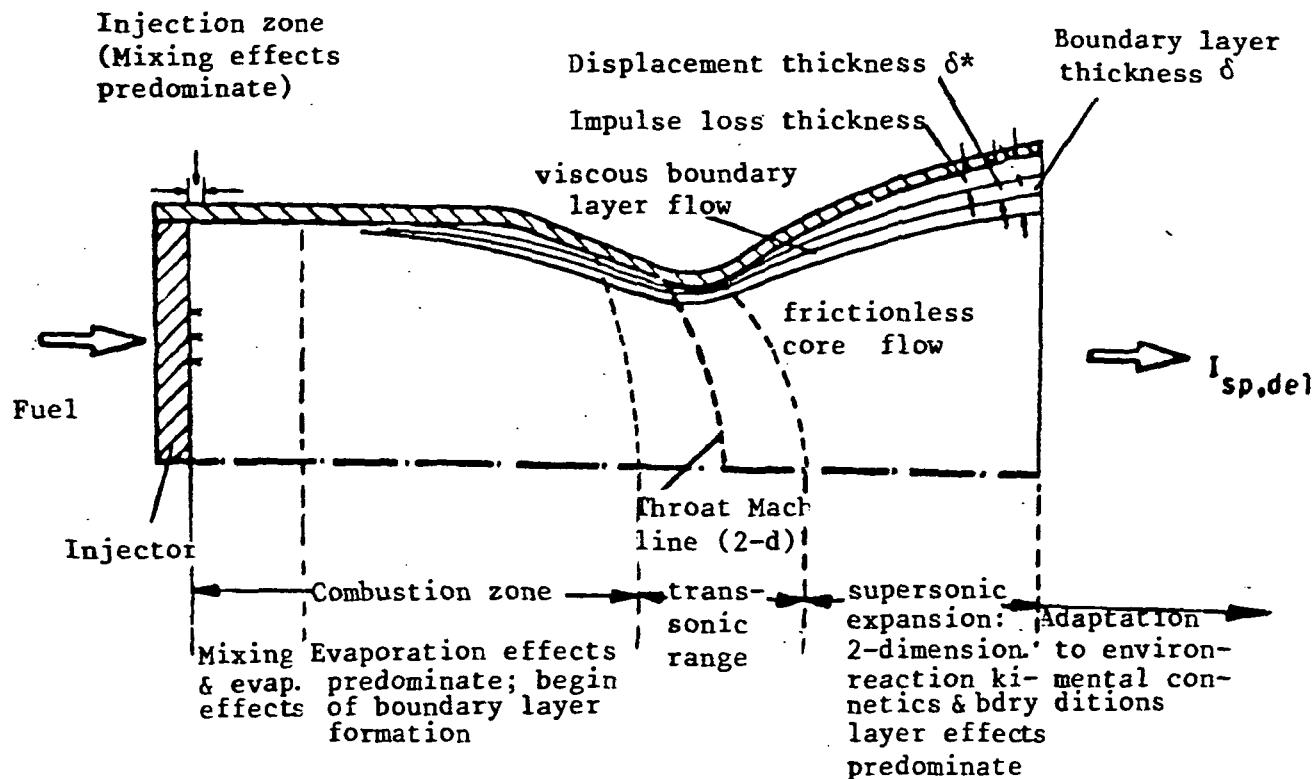

Figure 1 Processes in the combustion chamber and nozzle

$$I_{sp,del} = I_{sp,ODE,vac} \cdot \eta_{er} \cdot \eta_{kin} \cdot \eta_{part} \cdot \eta_{2-d,(3-d)} \cdot$$

$$\cdot \eta_{bl} \cdot \eta_{adapt} \cdot \eta_h \qquad (2)$$

2.2.1 Energy conversion in the combustion chamber

The first efficiency term on the right side is called energy conversion efficiency (energy release) of the injector-combustion chamber system. In the general case of the chemical multicomponent rocket propulsion unit it is not possible to obtain the total, theoretically possible energy yield, starting from the chemicals injected into the combustion chamber. Because of the finite dwell time in the combustion chamber ($v_c \neq 0$), incomplete mixing and fuel preparation, as well as due to technical implementation restrictions, η_{er} can not become equal to 1.0. However, implemented systems (SSME) today reach 0.997. Since here GN_2 occurs only as a single-component system and no reaction takes place, we can here set $\eta_{er} = 1.0$, however.

2.2.2 Kinetic efficiency

During the gas expansion process within the nozzle flow, the thermodynamically limiting parameters - such as T, p, ρ, λ, η - undergo significant changes and hence the combustion chamber conditions of the chemical condition ODE are no longer applicable. For instance, at high T_c dissociate molecules tend to recombine, as T decreases. Similarly, charged atoms and molecules (ions) are converted into neutral particles, by charge exchange. In addition, the state of excitation in the combustion chamber can initiate vibration processes in molecules, given a sufficently high Δh. All of these phenomena have in common that if the pressure or the temperature of the working fluid decrease, given the availability of a sufficiently long period of time, recombination or respectively, a relaxation of the excited degrees of freedom would occur. However, if this time - which depends very critically

19

on the gas component's characteristics, in each case - is not made possible by assuming an infinitely large expansion velocity, then we refer to a one-dimensional frozen equilibrium [ODF]. It represents a lower theoretical chem-thermodynamic performance value, because the energy contained in the gas' dissociation, ionization and vibration is not available - in contrast to the ODE flow - for expansion work and hence, the required gas acceleration; rather, it is still contained in the gas stream beyond the nozzle, after leaving it, in the form of internal energy, without contributing positively to the thrust. In the "technical nozzle flow" the so-called ODK flow [one-dimensional kinetic equilibrium] always lies between ODE and ODF (see Figure 2.2).

Hence in general the dwell time is sufficient to include a part (but of course not all) of the difference h(ODE-ODF) in the expansion work. The lower kinetic performance value can be expressed as

$$I_{sp,ODF,vac} = \frac{c^*_{ODF} \; c_{F,ODF,vac}}{g_0} \qquad (3)$$

Usually, to facilitate individual calculations, the total kinetic efficiency η_{kin} can be broken down into the product

$$\eta_{kin} = \eta_{k,dis} \cdot \eta_{k,ion} \cdot \eta_{k,vib} \qquad (4)$$

At this point it must be recalled, in general, that in the area of chemical kinetics considerable gaps still exist in the sense of an applicable engineering approximation. For some very special cases (molecules or gases, respectively, at certain specific pressure and temperature conditions) there are indications, in the literature, on reaction and recombination constants, but the quantitative theoretical statements contradict each other [71] as well as the few available measurement results. As an example we shall consider only the simplest case of the biatomic gas N_2 in the excited state.

According to Landau and Teller [53] the energy exchange between
the vibrational and translational degrees of freedom can be
described by means of the following linear differential equa-
tion (based on the model of the harmonic oscillator)

$$\frac{D\, e_v}{D\, t} = \frac{e_{v,Equi} - e_v}{\tau_v} \qquad (5)$$

where e_v is the vibrational energy per unit mass of gas;
$e_{v,\,equi}$ is the value of e_v when the molecule's vibration and
translation are at equilibrium; and τ_v is the relaxation time
for the exchange of vibrational and translational energy.

Assuming a Boltzmann distribution for the vibration energy steps,
vibration temperatures T_v can be calculated for them and then e_v
will be determined by

$$e_v = \frac{R\, h\, \nu}{k\, \mu_0 (e^{h\nu/kT_v} - 1)} \qquad (6)$$

Hence τ_v can be derived using the local pressure p as parameter
and compared to measured experimental data, for instance with
the aid of Raman spectroscopy. The results of this comparison
(the experiments were performed several times, by different
authors) are a surprise until this day, and are still awaiting
clarification. According to Landau-Teller the time τ_v would be
higher by a factor of 70 than the measured relaxation time.

Sebacher hence foregoes a theoretically derived function and
determined a compensating function adapted purely to empirical
values:

$$\tau_v\, p = 3 \cdot 10^{-12}\, e^{(181\, T^{-1/3})} \text{ (bar sec)} \qquad (7) \qquad \text{/14}$$

which here is typically 10 sec (T is the absolute gas tempera-
ture, here, NOT to be confused with T_v above).
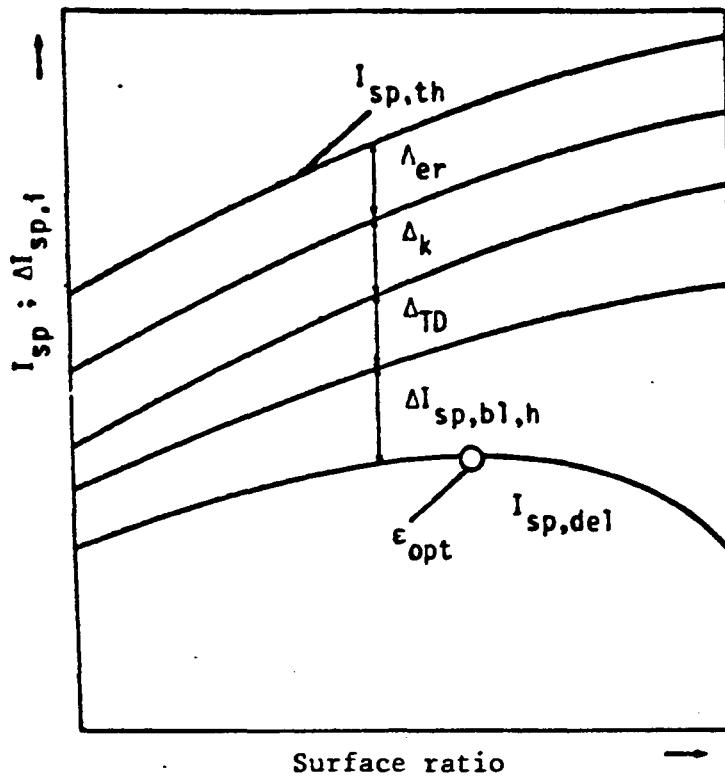
Figure 2.1 Qualitative course of the impulse, taking the various
losses into consideration

Comparison with the residence time of the gas in the propulsion
unit

$$t_{st} \approx \frac{1}{c^*} \left(\frac{\varepsilon \ F}{p_c}\right)^{0,5} \ \rightarrow \ \text{typically} \ 10^{-5} \ \text{sec} \qquad (8)$$

shows that in practice the flow becomes "frozen" shortly behind
the throat area, such that k_{reco} in the recombination equation

$$\eta_k = k_{reco} + \frac{I_{sp,ODF,vac}}{I_{sp,ODE,vac}} (1 - k_{reco}) \qquad (9)$$

can be set equal to 0, and we thus finally arrive at $\eta_k = 1.0$
for the case here under consideration.

This allows us to complete all remaining comparison calculations
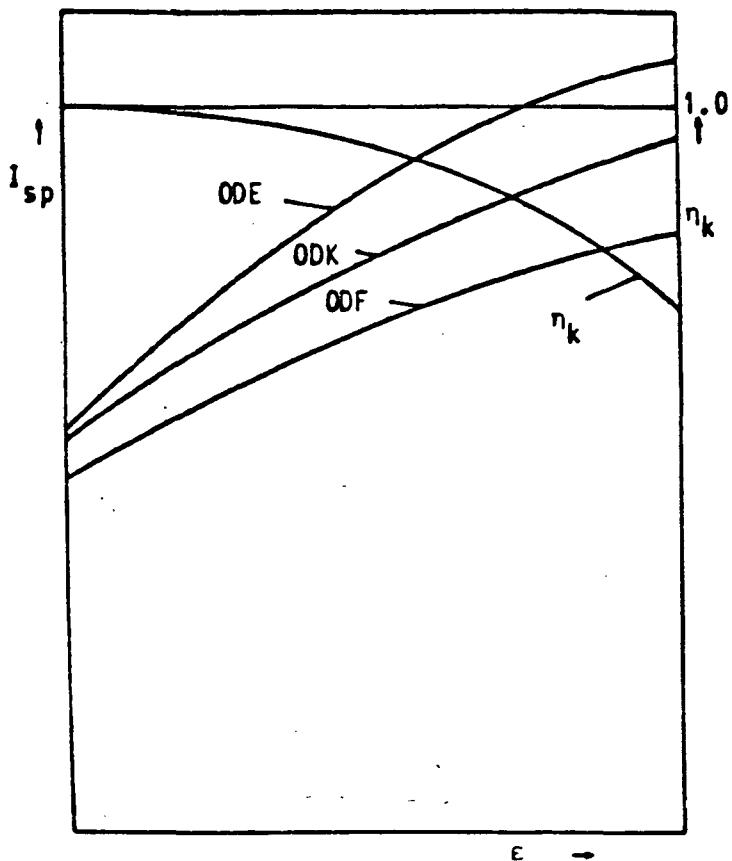
Figure 2.2 Qualitative courses of ODE, ODK and ODF impulses, as well as
kinetic efficiency, as a function of the surface ratio [47]

with ODF parameters, which is very advantageous because then
subsequent performance calculations can be separated from the
kinetics problem. It is certain that also in the future chemical
kinetics will considerably complicate total performance calcula-
tions for more complex gas combinations [33,91,112,125,138,157-
160]

2.2.3 Particle flow   /16

In the case of the monopropulsion unit, gas particle flow as it
occurs in modern solid fuel propulsion units (high Al proportion)
, as well as condensed droplets, such as they occur in liquid
fuel engines, do not take place. Nor was it possible to observe
any wear in the galvanized nozzle wall (not even in the espe-
cially endangered throat region). Hence, $\eta_{part}=1.0$ shall be used.

2.2.4 Multidimensional flow losses

2.2.4.1 Divergence losses
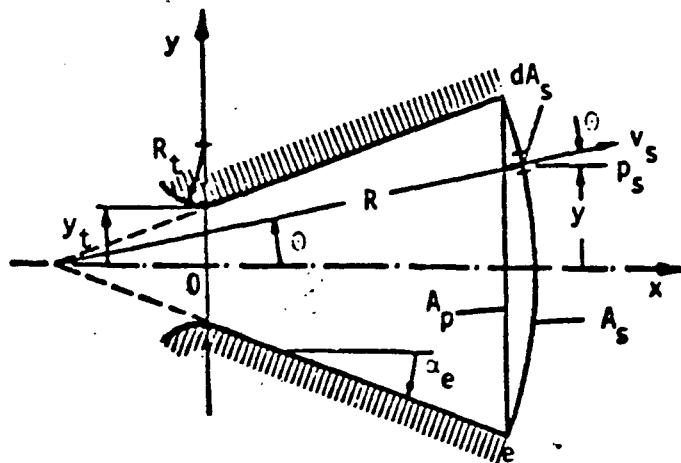
Figure 3   Geometry model to determine divergence losses

Due to radial divergence of the flowlines in the nozzle cross-
section as well as the distribution of the velocity and pressure
across the end cross-section surface area, there is an impulse
loss (in relation to 1-d flow). (3-d effects, such as vortex
formations due to asymmetry of the propulsion unit geometry, in
general can be disregarded as very small). In the case of the
bell nozzle, these multidimensional flow processes are usually
numerically simulated by means of characteristics procedures
[144]. In order to estimate TD losses in conical nozzles, how-
ever, the really rather voluminous computer programs are not
necessary. Starting from a source flow (such as, for instance,
the potential theory, [161]), the thrust fraction of the annular
spherical surface element dA_s in Figure 3, above,[119,179] is

$$dF = d\dot{m}\, v_s \cos \theta + (p_s - p_\infty)\, dA_s \cos \theta \qquad (10) \qquad \text{/17}$$

With $d\dot{m} = \rho_s v_s dA_s$ and $dA_s = 2 \pi R^2 \sin \theta\, d\theta$ and integrating once,

$$F_{TD} = 2 \pi R^2 \int_0^{\alpha_e} \left[\rho_s v_s^2 + (p_s - p_\infty) \right] \cos \theta \sin \theta\, d\theta \qquad (11)$$

24

Assuming that ρ_S, v_S and p_S are constant over the spherical surface A_S, and with

$$A_s = -2 \pi R^2 \cos 0 \Big|_0^{\alpha_e} = 2 \pi R^2 (1 - \cos \alpha_e) \tag{12}$$

$$(A_p = \pi R^2 \sin^2 \alpha_e)$$

equation (11) is rewritten as

$$F_{TD} = (\frac{1 + \cos \alpha_e}{2}) A_s [\rho_s v_s^2 + (p_s - p_\infty)] \tag{13}$$

With $\dot{m} = \rho_s A_s v_s$ the expression between brackets becomes

$$F_s = \dot{m} v_s + (p_s - p_\infty) A_s \tag{14}$$

F_s is the 1-dimensional thrust derived from the source flow model. The divergence factor η_{TD} corrects the 1-dimensional thrust taking into account the divergence losses and depends   /18 only on the opening angle α_e of the divergent portion of the nozzle:

$$\eta_{TD} = 0.5 (1 + \cos \alpha_e) \tag{15}$$

and hence

$$F_{TD} = \eta_{TD} F_s \tag{16}$$

With the aid of a Fortran program [144] available at the Chair for Space Technology it could be shown that the simplifying assumptions that led to the η_{TD} determined above for conical nozzles, are justified. The differences between the η_{TD} factor determined explicitly by means of the characteristics procedure and the simplified theory is less than 0.3% for a 15° conical nozzle [14,51,54,72,73,89,95,112,122-124,135,138,144,147,154,157).

25
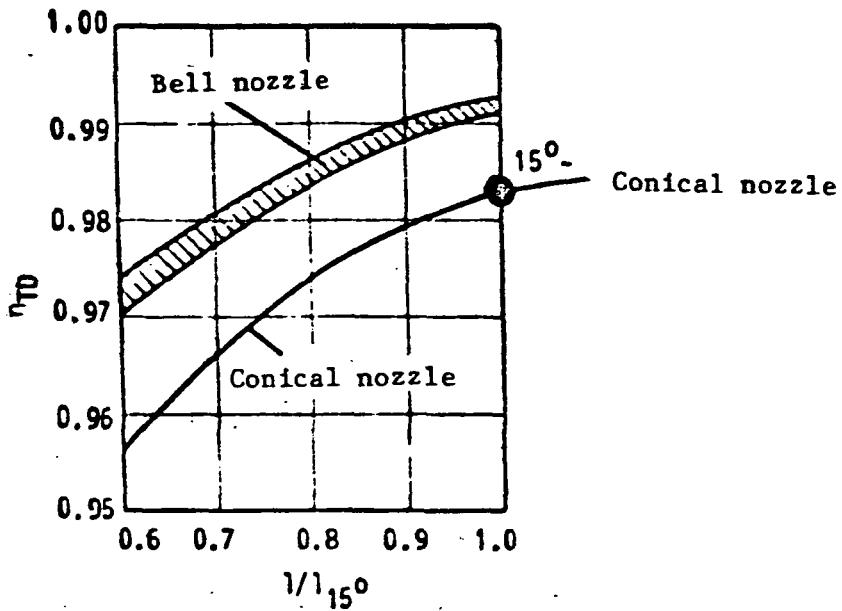
Figure 4   Two-dimensional flow losses for bell and conical
            nozzles as a function of normalized nozzle length

Figure 4, above, shows typical comparative results of the η_{TD}
calculation for conical and bell nozzles.

2.2.4.2 Mass throughput reduction   /19

Because of constriction and boundary layer effects the actual
mass throughput is reduced, with respect to $\dot{m}_{ODE}$.

In the LRT characteristics program already mentioned, a TD throat
isobar is determined, starting from a Sauer-Nicholson procedure,
which actually serves as a starting point for the entire pro-
cedure. It is not only possible to optimize the TD flow, thereby
(including wall pressure distribution), but a TD-$\dot{m}$-efficiency
can also be calculated, which usually lies between 0.993 and
0.996 (it does not include friction or boundary layer influences,
yet). Based on the work of Back et al. [3-5], for instance, in
addition the dependence of $\eta_{\dot{m}}$ on the throat's radius of curvature
can be determined. The result is shown in Figure 5 (page 27),
normalized with respect to r_t. It can be seen that the lowest $\dot{m}$
loss occurs when the throat's transition radius r_r is equal to

26
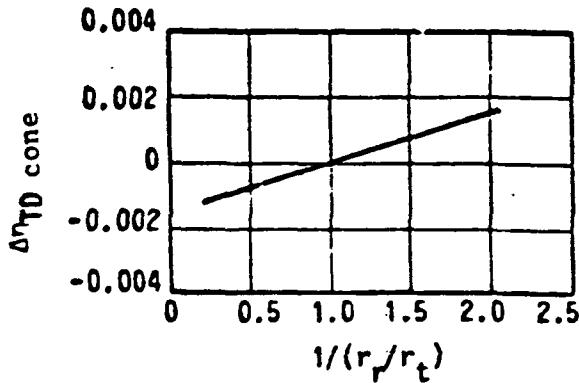
Figure 5 Effect of the throat transition radius
r_r on the TD losses [27,69]

r_t. The most substantial decrease in the ODE mass flow can be
attributed to viscous distortion effects, which "clog" the
nozzle throat area.

Hall et al [53] proposed the following equations for discussion:

$$c_D = \frac{\dot{m}_v}{\dot{m}_{ODE}} = 1 - (\gamma + 1)(\frac{r_t}{r_r})^2 \left[96 - \frac{8\gamma + 21}{4608} (\frac{r_t}{r_r}) + \right.$$

$$\left. + \frac{754\gamma^2 + 1971\gamma + 2007}{552960} \cdot (\frac{r_t}{r_r})^2 - \ldots\ldots \right] \tag{17}$$

Sauer, Oswatitsch and Rothstein[114,133,134] had already tried
a similar equation, which does not require the second and third
terms in the square bracket. Kuluva and Hosack [89] propose a
somewhat different representation,

$$c_D = (\frac{r_r + 0,05\ r_t}{r_r + 0,75\ r_t})^{0,019} \cdot \left[1 - (\frac{r_r + 0,1\ r_t}{r_t})^{0,21} \cdot (\frac{1}{Re})^{0,5} \cdot f(\gamma) \right], \tag{18}$$

which in a second range, of $30 < Re < 10^5$ agrees well with the

27

. experimental data. Figure 6, below, provides an overview; it
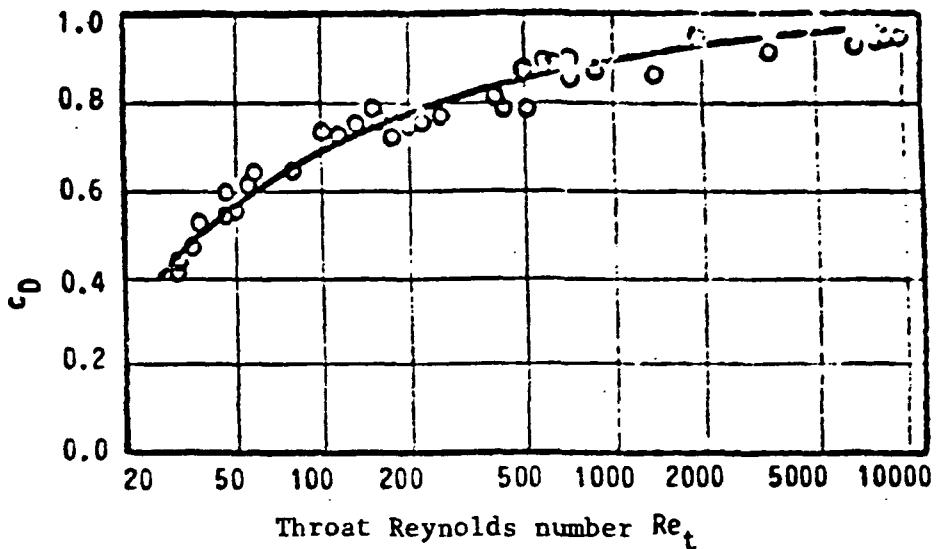
Figure 6   Mass throughput coefficient c_D as a function of Reynolds number
in the throat. Experimental data: $r_r/r_t = 4.42$; $\gamma = 1.4$. Solid
curve using equation (18)

can be seen that even at Re = 2,300, $c_D \simeq 0.90$, which differs
from other results reported. All of the statements found in the
literature have in common that they were obtained with substan-
tially larger nozzles (throat diameters) and a stronger influence
of local heat flows. In the case of the small diameter here
investigated, with a throat of 0.2 mm, and adiabatic conditions
in the flow range along the walls, the characteristic throughput
values depart from the equation above (see section 4.2). As was
the case in the correction procedure mentioned in section
2.2.5.3 for the determination of u_v, in the determination of c_D
we can resort directly to the available boundary layer quantity
δ^* and Θ. Since here - in contrast to nearly all procedures
reported in the literature - in the area of the throat $\delta^* \neq 0$
and $\Theta \neq 0$ (see also section 2.2.8), the contraction (or throat   /21
throughput) coefficient $c_D = \dfrac{A^*_{t,v}}{A_{t,n/v,ODE}}$ can be calculated with

sufficient accuracy by numerical methods. In anticipation of
sections 4.2 and 5, this way proves to be fully justified.

28

2.2.5 Boundary layer loss calculation

Because of gas viscosity and surface roughness on the propulsion unit's inner walls, boundary layers are formed, with the effect of reducing performance. (In large propulsion units these losses are merely a few (1-2) %, while they are substantially higher for smaller engines.) The first decision in the calculation of boundary layer problems requires an answer to the question of whether the flow is laminar or turbulent (see also [11,24,26,29, 30,38,41,65,94,95,99,100,103,104,107,108,112-114,117,118,122-124, 126,135,157,170,172,177,179]).

2.2.5.1 Flow condition

Normally, laminar flow can be assumed for nozzles of small dimensions. Because of the high flow velocities, the large Reynolds numbers would permit turbulent flow and it hence must be shown whether the large acceleration causes a laminarization of the boundary layer, within the nozzle. According to Boldman et al. [15], the following criterion can be used:

$$K_{acc} = (\frac{\nu_\infty}{u_\infty^2} \frac{du_\infty}{dx} + 0.352 \frac{\nu_\infty}{u_\infty r} \frac{dr}{dx}) > 2.88 \cdot 10^{-6} \qquad (19)$$

It can be readily shown that in the case of small nozzles the acceleration parameter K_{acc} is several-fold above the critical value. Hence, all boundary layer calculations presented will be based on a laminar velocity profile.

2.2.5.2 Impulse equation

The starting point for boundary layer calculations is the impulse equation for axisymmetrical nozzle flow [1,7-9,96,97,136,146,167]

$$\frac{d\Theta}{dz} = \frac{c_f}{2} \left[1 + (\frac{dr}{dz})^2 \right]^{1/2} - \Theta \left[\frac{2 - M^2 + \delta^*/\Theta}{(1 - \frac{1-\gamma}{2} M^2)M} \cdot \frac{dM}{dz} + \frac{1}{r} \frac{dr}{dz} \right] \qquad (20)$$

where

$$\delta^* = \delta_r - \delta_p = \int_0^{\delta_r} (1 - \frac{\rho u}{\rho_\infty u_\infty}) \, dy$$

is the displacement thickness of the boundary layer (Figure 7):
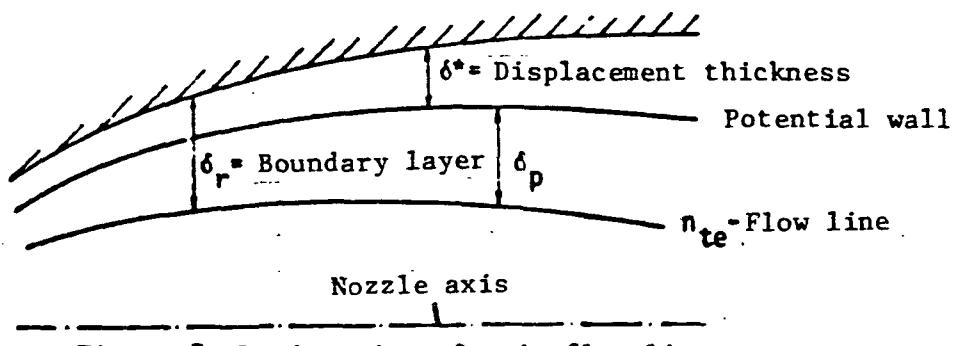
Figure 7   Designation of main flow lines

$$0 = \int_0^{\delta_r} \frac{\rho u}{\rho_\infty u_\infty} (1 - \frac{u}{u_\infty}) \, dy \qquad (22)$$

is the impulse loss thickness, and

$$c_f = \frac{\tau_w}{\frac{\rho_\infty u_\infty^2}{2}} \qquad (23)$$

the dimensionless friction coefficient with respect to wall shearing stress, $\underline{M}$ the Mach number of the core flow, $\underline{r}$ the local nozzle radius and d/dz the differential with respect to the nozzle axis coordinate.

In order to calculate the Mach number, we shall resort to an equation that can be solved only by iteration, for a given surface ratio ε:

30

$$\epsilon = \frac{1}{M} \left[\frac{2}{\gamma+1} \left(1 + \frac{\gamma-1}{2} M^2 \right) \right]^{\frac{\gamma+1}{2(\gamma-1)}} \qquad (24)$$

$$M = f(\epsilon, \gamma) \qquad (25)$$

2.2.5.2.1 Geometry determination

For the boundary layer calculation to be sufficiently precise, it is necessary to simulate the exact nozzle contour, without edges or obstructions. In the EGVP program here developed, the task $(R = f(z))$ is solved by a subroutine in six sections, with the aid of the main geometry points shown in Figure 8, below.
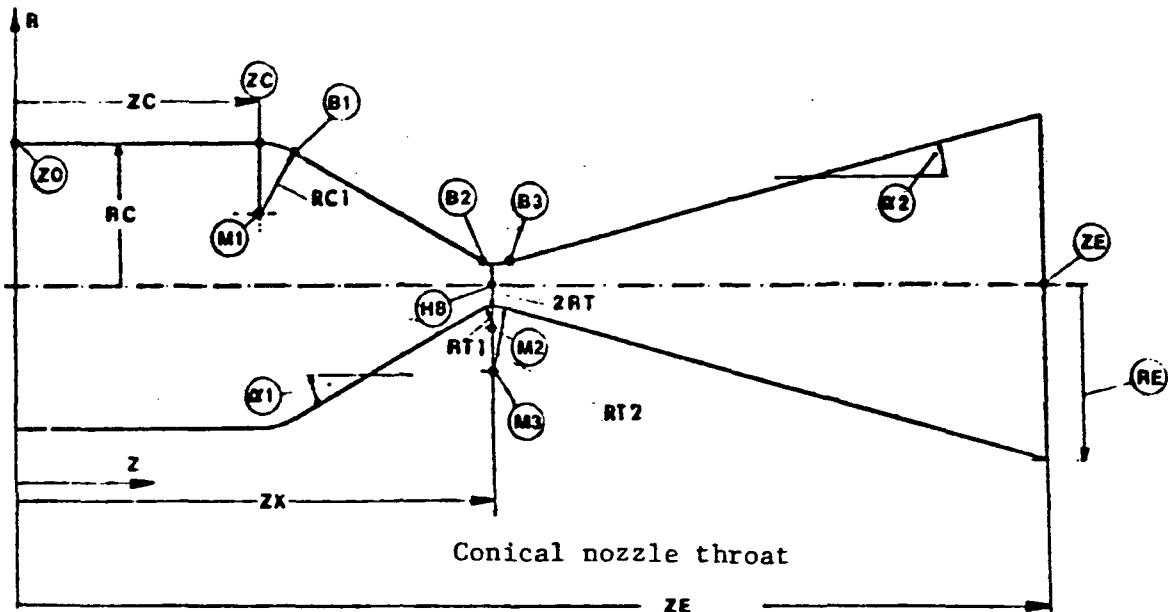
Figure 8   Nozzle geometry

```
1st section: Z0 to ZC
2nd section: ZC to B1
3rd section: B1 to B2
```

31

4th section: B2 to H8

5th section: H8 to B3

6th section: B3 to ZE

In contrast to most authors, who start the boundary layer
calculations at the nozzle's narrowest cross-section - which
seems justified in the case of large propulsion units, because
the severe contraction of the flow at the throat reduces the
boundary layer thickness to practically 0, at the narrowest
cross-section - here we begin at the combustion chamber head.
It is shown that even for small throat diameters (< 1 mm) the
boundary layer thickness appears to be negligible in the throat
region (see Figure 9, below). Nevertheless, including the subsonic
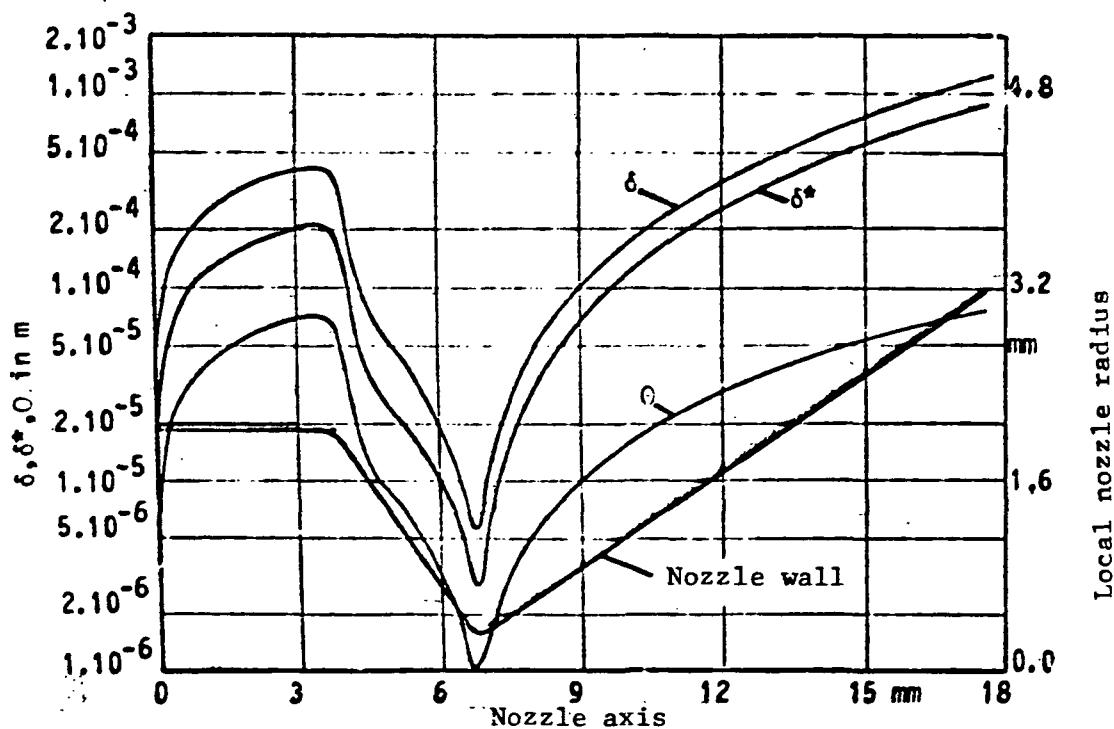
Figure 9   Boundary layer parameter development along the nozzle wall

range in the boundary layer calculation of nozzles represents a
physical expansion and numerical completion.

In general, for locally constant viscosity the shearing stress at the wall is

$$\tau_w = \eta_w \left(\frac{\partial u}{\partial y}\right)_w \tag{26}$$

where η_w is the gas viscosity at the wall, which is a function of the temperature:

$$\eta_w = f(T_w) = f(M, u_\infty, T_c, \gamma, \varepsilon) \tag{27}$$

The shearing stress coefficient is defined as

$$c_f = \frac{\tau_w}{\frac{\rho_w}{2} u_\infty^2} = 2 \frac{\eta_w}{\rho_w} \frac{1}{u_\infty^2} \frac{\partial u}{\partial y} \tag{28}$$

Figures 10 and 11, below, show the nomenclature, in further
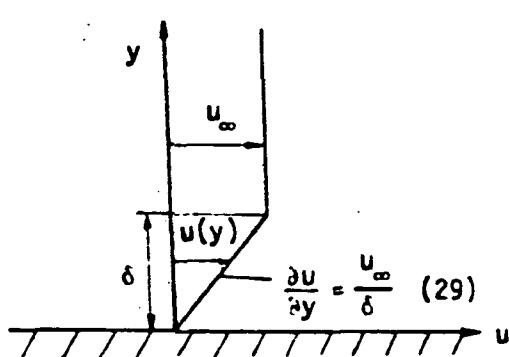
Figure 10 Linear velocity profile

$$\frac{\partial u}{\partial y} = \frac{u_\infty}{\delta} \tag{29}$$
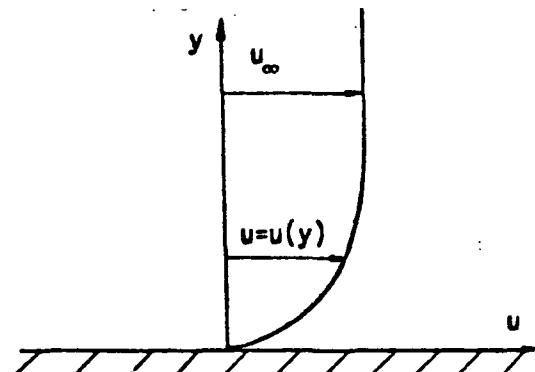
Figure 11 Parabolic velocity profile

considerations, for a general and a linear velocity profile within the boundary layer.

The gas density at the wall is derived from /27

33

$$\frac{\rho}{\rho_g} = \frac{T_g}{T} = \frac{1}{1 + \frac{\gamma-1}{2} M_g^2 \left\{ 1 - \left(\frac{u}{u_g}\right)^2 \right\}} \quad \text{with} \tag{30}$$

$$\frac{T_c}{T_g} = 1 + \frac{\gamma-1}{2} M_g^2 \quad \text{and} \tag{31}$$

$u = u_w = 0$ we can determine ρ_w, the density at the wall.

$$\rho_w = \rho_c \left(\frac{T_g}{T_c}\right)^{\frac{\gamma}{\gamma-1}} \tag{32}$$

where the subindices refer to:

c = chamber conditions,
g = edge of the boundary layer (to the core flow),
w = wall.

We must now take into account the temperature dependence of the viscosity, $\eta = \eta(T)$. Anticipating experimental results, we shall assume that no heat is removed through the wall. With

$$\frac{T}{T_g} = 1 + \frac{\gamma-1}{2} \left[M_g^2 \left[1 - \left(\frac{u}{u_g}\right)^2 \right] \right] \quad \text{and} \tag{33}$$

$$u = u_w = 0; \quad M_w = 0 \quad \text{we obtain}$$

$$T_w = T_c \quad \text{and hence also} \quad \eta_w = \eta_c \tag{34}$$

With equations (29) and (32), the shearing stress coefficient c_f /28 becomes:

34

$$c_f = \frac{2,0}{\delta u_\infty} \cdot \frac{\eta_c}{\rho_c \left(\frac{\vartheta}{T_c}\right)^{\frac{\gamma}{\gamma-1}}} \qquad (35)$$

The temperature dependence of the GN_2 viscosity is approximated by means of

$$\eta = \eta_c \left(\frac{T}{T_c}\right)^x \qquad (36)$$

where

$$T_c = 300 \text{ K}$$
$$\eta_c = 1,769 \cdot 10^{-5} \text{ kg/msec}$$
$$x = 0,71976$$

A variety of expressions is used in the literature:

$$c_f = \frac{0,5533}{Re_\Theta} \qquad \text{(Ziebland (177))} \qquad (37)$$

$$c_f = \frac{0,571}{Re_\Theta} \qquad \text{(Bartz (9))} \qquad (38)$$

/29

(general; see Figure 12;[61])

Here Re_Θ represents the Reynolds number related to the impulse loss thickness.

$$c_f = \frac{K_1}{Re_\Theta} \qquad (39)$$

$$c_f = \frac{0.664}{\sqrt{Re_z}} = \frac{0.664}{\sqrt{\dfrac{u_\infty z}{\nu}}} \qquad \text{(Schlichting (136))}$$

$$c_f = \frac{0.664}{\sqrt{Re_z}} - \frac{0.01085}{\sqrt{Re_z}} M_\infty^{3/2} \qquad \text{(Shapiro (150))}$$
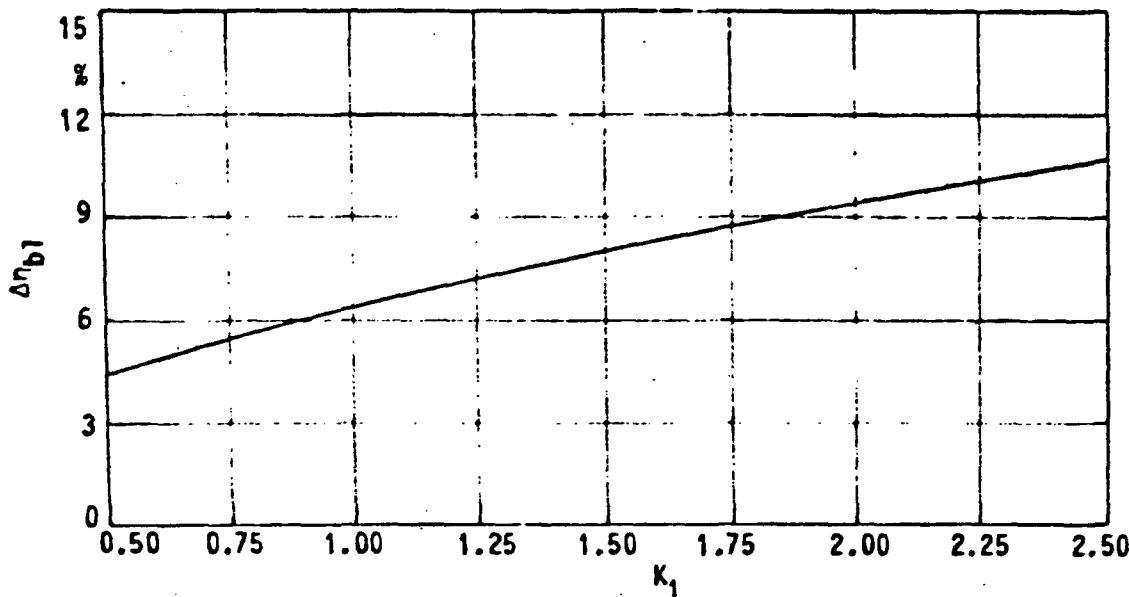
Figure 12   Effect of the shearing stress coefficient K_1
on the boundary layer losses

2.2.5.2.3 Derivation of the boundary layer shape factor, δ^*/θ /30

Using the usual integral equations of the boundary layer theory
for the displacement and impulse loss thicknesses,

$$\delta^*/\delta = \int_0^1 \left(1 - \frac{\rho}{\rho_g}\frac{u}{u_g}\right) d\left(\frac{y}{\delta}\right) \tag{42}$$

$$\theta/\delta = \int_0^1 \frac{\rho}{\rho_g}\frac{u}{u_g}\left(1 - \frac{u}{u_g}\right) d\left(\frac{y}{\delta}\right) = \int_0^1 \frac{\rho}{\rho_g}\frac{u}{u_g} d\left(\frac{y}{\delta}\right) - \int_0^1 \frac{\rho}{\rho_g}\frac{u^2}{u^2_g} d\left(\frac{y}{\delta}\right) \tag{43}$$

where ρ and $\underline{u}$ are the density within the boundary layer, ρ_g
and u_g the corresponding values at its edge, and $\underline{y}$ is the

coordinate perpendicular to the wall, the ratio δ^*/θ is sought, which is necessary for the integration of the impulse equation.

By introducing the ideal gas equation and using equation (38), it is possible to rewrite equation (29) thus

$$\frac{\rho}{\rho_g} = \frac{T_g}{T_c - T_g} \cdot \frac{1}{\frac{T_c}{T_c - T_g} - (\frac{u}{u_g})^2} \qquad (44)$$

Using the linear velocity distribution on which equation (36) is based (a comparison with the exact distribution is shown in Figure 13, below), the integral equation can be rewritten:
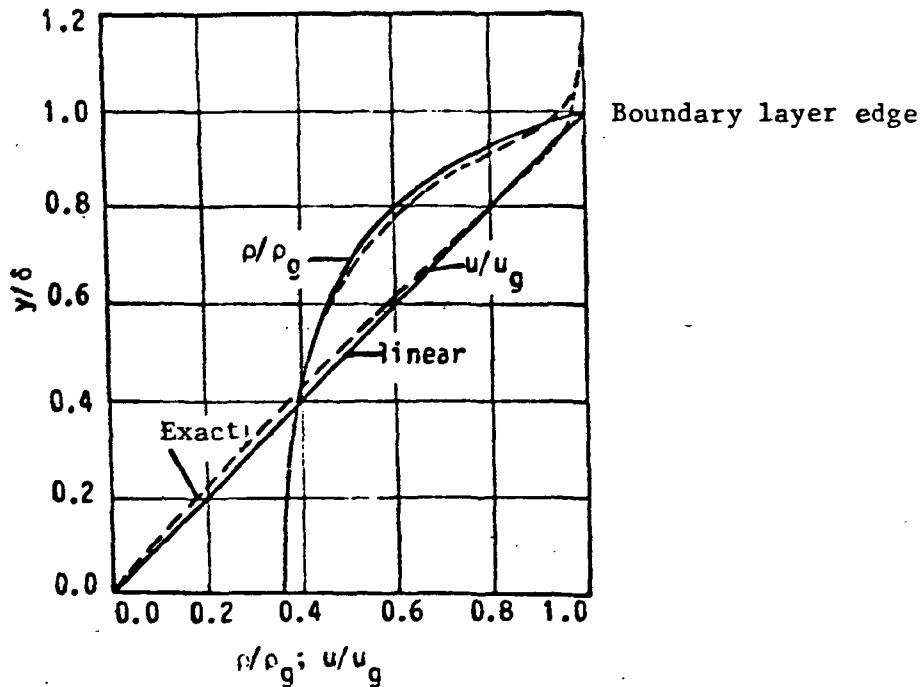
Figure 13   Comparison between the simplified linear and actual velocity distribution with respect to the course of density and velocity within the boundary layer

$$\int_0^1 \frac{\rho}{\rho_g} \frac{u}{u_g} d(\frac{y}{\delta}) = \frac{T_g}{\Delta T} \int_0^1 \frac{(y/\delta)}{\frac{T_c}{\Delta T} - (\frac{y}{\delta})^2} d(\frac{y}{\delta}) \quad \text{and} \qquad (45)$$

37

$$\int_0^1 \frac{\rho}{\rho_g} \frac{u^2}{u_g^2} \, d(\tfrac{y}{\delta}) - \frac{T_g}{\Delta T} \int_0^1 \frac{(y/\delta)^2}{\frac{T_c}{\Delta T} - (\tfrac{y}{\delta})^2} \, d(\tfrac{y}{\delta}) \quad , \text{ where} \qquad (46)$$

$$\Delta T = T_c - T_g \qquad\qquad (47)$$

For equation (45), integration yields

$$(48) \qquad\qquad -\frac{T_g}{2\Delta T} \ln\left(1 - \frac{\Delta T}{T_c}\right) \qquad \text{and for equation (46)}$$

$$\frac{T_g}{2\Delta T}\left[(\tfrac{T_c}{\Delta T})^{0.5} \cdot \ln \frac{(\tfrac{T_c}{\Delta T})^{0.5} + 1}{(\tfrac{T_c}{\Delta T})^{0.5} - 1} - 2\right] \qquad (49)$$

With these intermediate results, the shape parameter δ^*/θ can be given in a form that now only depends on the corresponding temperatures, T_c and T_g.

$$\frac{\delta^*}{\theta} = \frac{-\dfrac{2\,(T_c - T_g)}{T_g} - \ln \dfrac{T_g}{T_c}}{\ln \dfrac{T_g}{T_c} - 2 + (\tfrac{T_c}{T_c - T_g})^{0.5} \cdot \ln \dfrac{(\tfrac{T_c}{T_c - T_g})^{0.5} + 1}{(\tfrac{T_c}{T_c - T_g})^{0.5} - 1}} \qquad (50)$$

Figure 14 (page 39) shows a plot of this parameter for increasing Mach numbers (or ϵ, respectively), with γ as the parameter.

For a non-adiabatic wall, the wall temperature will be lower than the stagnation temperature, and the gas density near the wall will be higher than in the adiabatic cases. Therefor δ^* will be smaller and also δ^*/θ, because
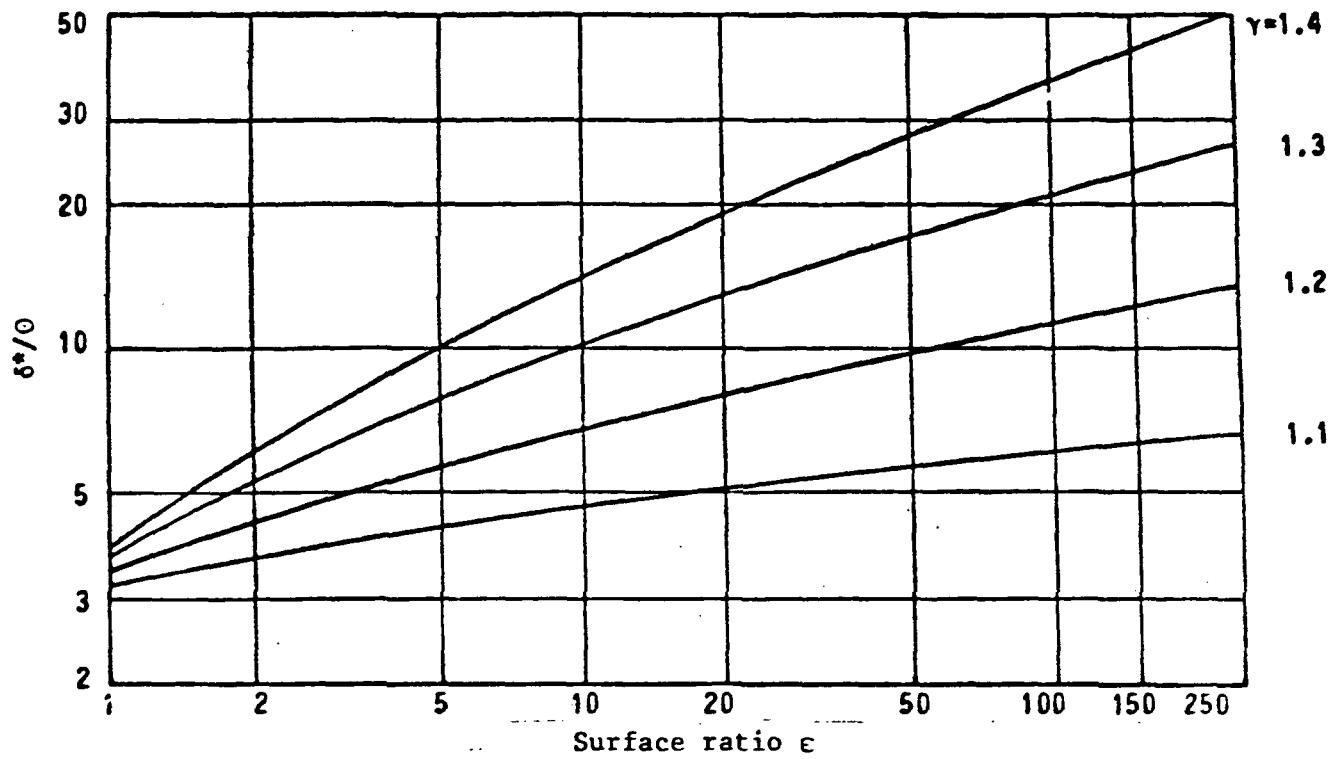
Figure 14   Increase in boundary layer shape parameter $\delta*/\Theta$ as a function of ϵ with γ as parameter

$$\left.\int_0^1 \frac{\rho}{\rho_g} \frac{u}{u_g} d\left(\frac{y}{\delta}\right)\right|_{adiabatic\ wall} < \left.\int_0^1 \frac{\rho}{\rho_g} \frac{u}{u_g} d\left(\frac{y}{\delta}\right)\right|_{Non-adiabatic\ wall} \tag{51}$$

The gradient $\delta*/\Theta$ is not much affected, however, precisely for the case of large surface ratios, in which the stationary wall temperature is considerably below either the combustion chamber or the stagnation temperature.

2.2.5.3 Nozzle shape correction

Due to the formation of the boundary layer, the inviscid geo-metrical cross-sectional area of the nozzle is reduced by the

39

impulse loss thickness. To determine the resulting thrust loss
it is necessary to determine the fully viscous velocity distri-
bution, which can be derived assuming that the mass throughput
through the narrowest cross-section also flows through the
nozzle end cross-section (contiguity equation)

$$\dot{m}_v = \dot{m}_{n/v} = \dot{m} \tag{52}$$

Including the usual boundary layer quantities, we obtain: for
the mass throughput

$$\dot{m} = \pi \cdot u_{g,v} \cdot \rho_{g,v} (r_e - \delta)^2 + 2\pi (r_e - \frac{\delta}{2}) \cdot \rho_{g,v} \cdot u_{g,v} \cdot$$

$$\cdot \delta \cdot \int_0^1 \frac{u \cdot \rho}{u_{g,v} \cdot \rho_{g,v}} d(\frac{y}{\delta}) \tag{53}$$

and for the thrust,

$$F = \pi \cdot u_g^2 \cdot \rho_g (r_e - \delta)^2 + 2\pi (r_e - \frac{\delta}{2}) \cdot \rho_g \cdot u_g^2 \cdot \delta \cdot$$

$$\cdot \int_0^1 \tilde{\rho} \tilde{U}^2 d\tilde{y} \tag{54}$$

with the abbreviations

$$
\begin{aligned}
u_{g,v} &= u_v \\
\rho_{g,v} &= \rho_v \\
\rho/\rho_{g,v} &= \tilde{\rho} \\
u/u_{g,v} &= \tilde{U}
\end{aligned}
$$

We can now rewrite equations (53) and (54), as

$$\pi u_v \rho_v (r - \delta)^2 + 2\pi (r - \frac{\delta}{2}) \rho_v u_v \delta (1 - \frac{\delta^*}{\delta}) = \pi r^2 \rho_{n/v} \cdot u_{n/v} \tag{55}$$

40

$$F_v = \pi u_v^2 \cdot \rho_v (r_e - \delta)^2 + 2\pi \; (r_e - \tfrac{\delta}{2}) \rho_v u_v^2 \cdot \delta \cdot (1 - \tfrac{\delta^*}{\delta} - \tfrac{\Theta}{\delta}). \qquad (56)$$

The viscous thrust (includes: boundary layer behavior due to
gas viscosity and wall friction) will be, expressed in abbrevia-
tions:

$$F_v = \underbrace{\pi \cdot r_e^2 \cdot u_{n/v}^2 \cdot \rho_{n/v}}_{F_{n/v}} - \Delta F_{bl} \qquad (57)$$

Using the customary definition for specific impulse: $I_{sp} = \dot{F}/\dot{m} \, g_0$ we obtain from equation (57), taking into consideration
equations (55) and (56), the following loss of impulse

$$\Delta I_{sp,bl} \cdot g_0 = u_{n/v} - \frac{u_v^2 \cdot \rho_v}{u_{n/v} \cdot \rho_{n/v}} (1 - \tfrac{\delta}{r})^2 - 2 \frac{u_v^2 \cdot \rho_v}{u_{n/v} \cdot \rho_{n/v}} \cdot \qquad (58)$$

$$\cdot \frac{\delta}{r} (1 - \tfrac{\delta}{2r}) \cdot (1 - \tfrac{\delta^*}{\delta} - \tfrac{\Theta}{\delta})$$

/36

$$\Delta I_{sp} \cdot g_0 = u_{n/v} - \frac{u_v^2 \cdot \rho_v}{u_{n/v} \cdot \rho_{n/v}} \underbrace{\left[(1 - \tfrac{\delta}{r})^2 + \tfrac{2\delta}{r}(1 - \tfrac{\delta}{2r})(1 - \tfrac{\delta^*}{\delta} - \tfrac{\Theta}{\delta}) \right]}_{K_\Theta} \qquad (59)$$

The denominator of the factor in the square bracket (K_Θ) can
also be transformed, with the aid of equation (55), in a form
that depends only on the boundary layer parameters

$$\rho_{n/v} \cdot u_{n/v} = \frac{\pi \cdot u_v \cdot \rho_v (r-\delta)^2 + 2\pi \; (r - \tfrac{\delta}{2})\rho_v u_v \delta \; (1 - \tfrac{\delta^*}{\delta})}{\pi \, r^2} \qquad (60)$$

or respectively,

41

$$\rho_{n/v} \, u_{n/v} = \rho_v \, u_v \, K_{\dot{m}} \tag{61}$$

Equation (59) for the loss of impulse now becomes

$$\Delta I_{sp} \cdot g_o = u_{n/v} - u_v \cdot \frac{K_o}{K_{\dot{m}}} \tag{62}$$

The determination of the velocity ratio

$$\frac{u_v}{u_{n/v}} = \frac{\rho_{n/v}}{\rho_v} \frac{1}{K_{\dot{m}}} \tag{63}$$

occurs by means of the relationship already presented in equation (30), and with the known definition of the Mach number

$$M_g^2 = \frac{u_g^2}{\gamma \, R \, T_g} \tag{64}$$

To begin with, we shall divide our considerations into two cases

$$T_g = T_{n/v} \quad \hat{=} \text{ Case 1}$$

$$T_g = T_v \quad \hat{=} \text{ Case 2}$$

Case 1):

$$\frac{T_c}{T_{n/v}} = 1 + \frac{\gamma-1}{2} M_{n/v}^2 = 1 + \frac{\gamma-1}{2} \frac{u_{n/v}^2}{\gamma \, R \, T_{n/v}} \quad \text{with} \tag{65}$$

$$K_{T_c} = \left(\frac{\gamma-1}{2 \, \gamma \, R \, T_c} \right)^{-0.5} \quad \text{therefore} \tag{66}$$

$$u_{n/v} = K_{T_c} \left(1 - \frac{T_{n/v}}{T_c} \right)^{0.5} \tag{67}$$

42

The abbreviation K_{T_c} is a constant for local nozzle points.

A similar treatment follows for Case 2):

$$u_v = K_{T_c} (1 - \frac{T_v}{T_c})^{0,5} \qquad (68)$$

Now the velocity ratio in equation (63) can be expressed in a form that depends only on T

$$(\frac{u_v}{u_{n/v}})^2 = (T_c - T_v)/(T_c - T_{n/v}) \qquad (69)$$

With equation (61) and the general gas law, as well as a rewritten equation (69)

$$(70) \qquad \frac{T_v}{T_{n/v}} = \frac{T_c}{T_{n/v}} \left[1 - (\frac{u_v}{u_{n/v}})^2 \right] + (\frac{u_v}{u_{n/v}})^2 \qquad \text{therefore}$$

$$\frac{u_v}{u_{n/v}} = \frac{1}{K_m} \frac{p_{n/v}}{p_v} \frac{T_v}{T_{n/v}} \qquad (71)$$

Since the pressure can be determined from a temperature function

$$p^{\frac{\gamma-1}{\gamma}} = T \qquad \text{or} \qquad p = T^{\frac{\gamma}{\gamma-1}} \qquad (72)$$

we conclude

$$\frac{u_v}{u_{n/v}} = \frac{1}{K_m} (\frac{T_{n/v}}{T_v})^{\frac{1}{\gamma-1}} \qquad (73)$$

But since the viscous temperature T_v is not known explicitly, it is replaced by equation (70) and equation (73) now becomes

$$\frac{u_v}{u_{n/v}} = \frac{1}{K_m} \left[\frac{\dfrac{K_{T_c}^2 - u_{n/v}^2}{K_{T_c}^2}}{1 - \dfrac{u_v^2}{K_{T_c}^2}} \right]^{\frac{1}{\gamma-1}} \qquad \text{or respectively,} \qquad (74)$$

43

$$(u_v \, \kappa_{\dot{m}})^{\gamma-1} \, (\kappa_{T_c}^2 - u_v^2) = (\kappa_{T_c}^2 - u_{n/v}^2) \, u_{n/v}^{\gamma-1} = A \qquad (75)$$

The right hand side of this equation is already known, through the quantities that can be determined by the potential theory and hence the fully viscous velocity u_v sought must be determined by iteration from the final equation, which can not be solved explicitly,

$$u_v^{\gamma-1} \, \kappa_{T_c}^2 - u_v^{\gamma+1} = \frac{A}{\kappa_{\dot{m}}^{\gamma-1}} \qquad (76)$$

By means of the very important quantity u_v here determined, it
is now possible to incorporate the influence of boundary layer development on the core flow within the nozzle, directly into the computer program.

2.2.5.4 Correction of the compressive thrust term

In analogy to the influence by the viscous velocity development, the compressive thrust portion must be corrected to include the boundary layer conditions.

The entire loss of thrust due to boundary layer effects is expressed by

$$\Delta F_{bl} = \Delta F_{bl,I_{sp}} + A_{e,2-d} \, (p_{e,n/v} - p_{e,v}) \qquad (77)$$

Taking into account the results of the $u_v = f(u_{n/v})$ determination, the following relationship exists between the pressure equation and the velocity distribution

$$\left(\frac{u_{n/v}}{u_v}\right)^2 = \frac{1 - \left(\frac{p_{e,n/v}}{p_c}\right)^{\frac{\gamma-1}{\gamma}}}{1 - \left(\frac{p_{e,v}}{p_c}\right)^{\frac{\gamma-1}{\gamma}}} \qquad (78)$$

Rearranging and solving by viscous and inviscid terms yields

$$1 - \frac{1}{(\frac{u_{n/v}}{u_v})^2} + \frac{(\frac{p_{e,n/v}}{p_c})^{\frac{\gamma-1}{\gamma}}}{(\frac{u_{n/v}}{u_v})^2} = (\frac{p_{e,v}}{p_c})^{\frac{\gamma-1}{\gamma}} \cdot K_p \qquad (79)$$

The right-hand side includes only magnitudes already determined /41
and hence the fully viscous end pressure $p_{e/v}$ now depends only
on p_c, γ and the already determined value K_p.

$$p_{e,v} = p_c \, K_p^{\frac{\gamma}{\gamma-1}} \qquad (80)$$

2.2.5.5 Connection between nozzle end values and boundary layer losses

Based on the preceding considerations and the Fortran IV computer
programs built on them, all required fully viscous nozzle end
values can be numerically obtained with sufficient precision. On
this basis, the total integrated boundary layer loss for super-
sonic flow can be obtained

$$\Delta I_{sp} \cdot g_0 = u_{n/v,e} - \frac{u_{v,e}^2 \cdot \rho_{v,e}}{u_{n/v,e} \cdot \rho_{n/v,e}} \left[(1 - \frac{\delta_e}{r_e})^2 + \frac{2\delta_e}{r_e} \cdot \right.$$

$$\left. \cdot (1 - \frac{\delta_e}{2r_e}) (1 - \frac{\delta_e^*}{\delta_e} - \frac{\theta_e}{\delta_e}) + A_e (p_{e,n/v} - p_c \cdot K_p^{\frac{\gamma}{\gamma-1}}) \right] \qquad (81)$$

or, related to a 1-dimensional loss free theoretical impulse

$$\eta_{bl} = \frac{I_{sp,n/v} - \Delta I_{sp,bl}}{I_{sp,n/v}} \qquad (82)$$

A review of the numerical treatment of the functions and differ- /42
ential equations in the preceding portion is contained in the

45

form of a flow diagram, in the Appendix. The integration of the impulse differential equation (see section 2.2.5.2) is performed applying an explicit differences procedure, based on the Lax-Wendroff method [35,84,94,107,115].

2.2.5.6 Polynomial for the velocity profile

In order to prove that the simplified linear theory of the velocity profile described above does not represent an impermissible imprecision, a polynomial profile will be used in addition, derived from laminar flow (Pohlhausen) [136,165],

$$\frac{u_g}{u} = (2\eta - 2\eta^3 + \eta^4) + \frac{\Lambda}{6} (\eta - 3\eta^2 + 3\eta^3 - \eta^4) \qquad (83)$$

$$\Lambda = \frac{\delta^2}{\gamma} \cdot \frac{du}{dz} \quad \text{and} \quad \eta = \frac{\delta}{y} \quad \text{for } 0 < y < \delta \qquad (84)$$

The $\Delta\eta_{bl}$ results thus obtained show no decisive departures from the results obtained with the linear profiles and hence all subsequent cases will be investigated using it.

2.2.5.7 Roughness equation

To include the effect of the roughness of the nozzle's inner wall on the formation of the boundary layer, at each computation stage in the core flow, $Re_{n/v}$ will be compared to the values known for pipe flow. As is known, at Reynolds numbers >2,300, Colebrook-White's equation [161] is valid for the transition range of the pipe friction number

$$\frac{1}{\sqrt{\lambda}} = -2 \log \frac{2,51}{Re_{n/v} \sqrt{\lambda}} + 0,27 \frac{Rau}{2 R} \qquad (85)$$

In contrast, by calculation of the laminarization parameter it is now known that laminar flow predominates. Hence, the calculated

Reynolds number (> 2,300) must be recalculated - with the aid
of the pipe friction coefficients - to the Reynolds numbers of
a laminar pipe flow Re_k, which is possible with

$$Re_k = \frac{64}{\lambda} \qquad (86)$$

The effect of roughness is seen by correction of the viscosity
parameter

$$\eta_{g,k} = \eta_g \frac{Re_{n/v}}{Re_k} \qquad (87)$$

In the calculation processes, wall friction is taken into con-
sideration by means of

$$c_f = \frac{k}{Re_z} \quad \text{with} \quad Re_z = \frac{p_c \, \delta^*}{c^* \, \eta_g \, \epsilon} \qquad (88)$$

(k = 0.5 in the smooth case).

In this model the factor k = f(rough) is connected with a $\qquad$ /44
Reynolds number that takes into account the displacement thick-
ness δ^* and indirectly - through the corresponding surface ratio
ϵ - also includes the geometry. If we set k = f(rough/R), then
the roughness is correlated directly with the geometry (Figures
15 and 16), as generally customary in pipe friction theory.

Other possibilities for a roughness equation are listed below.
A roughness expression in terms of the wall shearing stress coef-
ficient c_f seems most appropriate, since it is affected by the
roughness of the surface layer. Thus, all possibilities that can
expand c_f by means of an additive or multiplicative term, are
open.

An additive term

$$c_f = \frac{0,5}{Re_{n/v}} + \frac{k_1}{Re_y} \qquad (89)$$

47
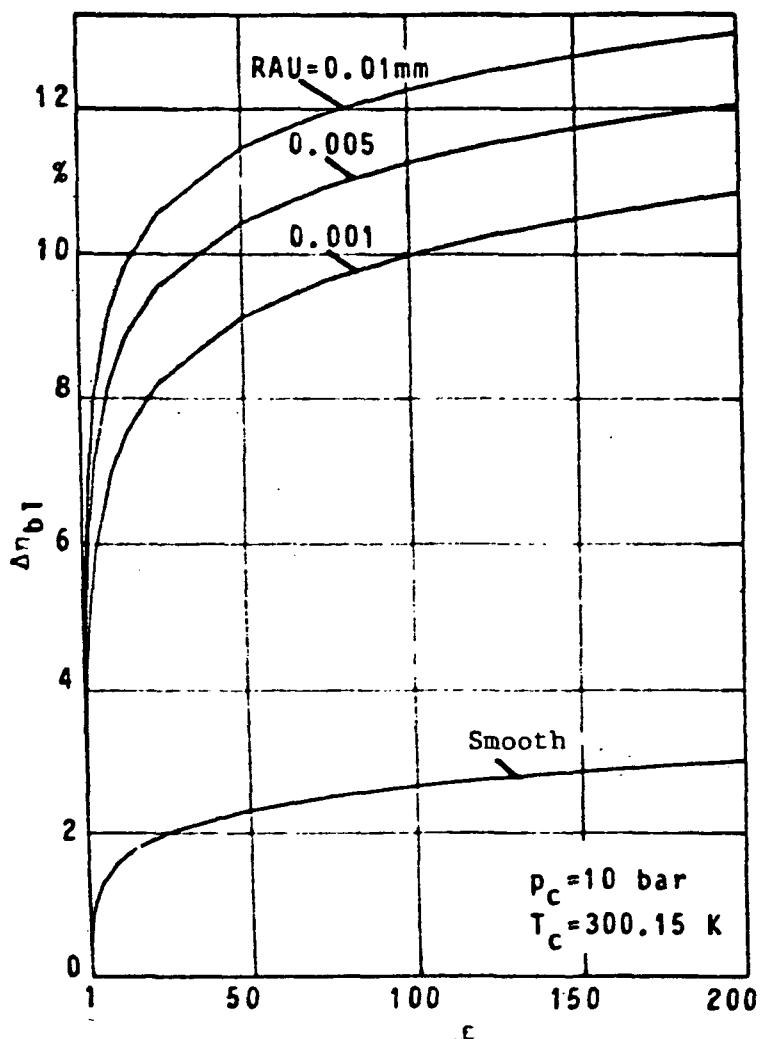
Figure 15 Effect of roughness calculated using REKOR. Nozzle 5

offers the possibility of introducing k_1 = f(rough) and to form the Reynolds number Re_y with the core flow velocity, or the velocity at the height of maximum roughness; Reynolds numbers formed on the basis of mean velocity values are also conceivable. A multiplicative term $c_f = \frac{0.5}{Re_{n/v}} k_2$ makes it possible to define a kind of loss efficiency of the wall roughness, in which the height of the roughness is related to length, to form k_2. Suitable lengths are δ^*, r_t or a combination of both. The literature does not offer any suitable roughness expression that would be universally applicable to small nozzles with Re > 2300 (laminar).

48
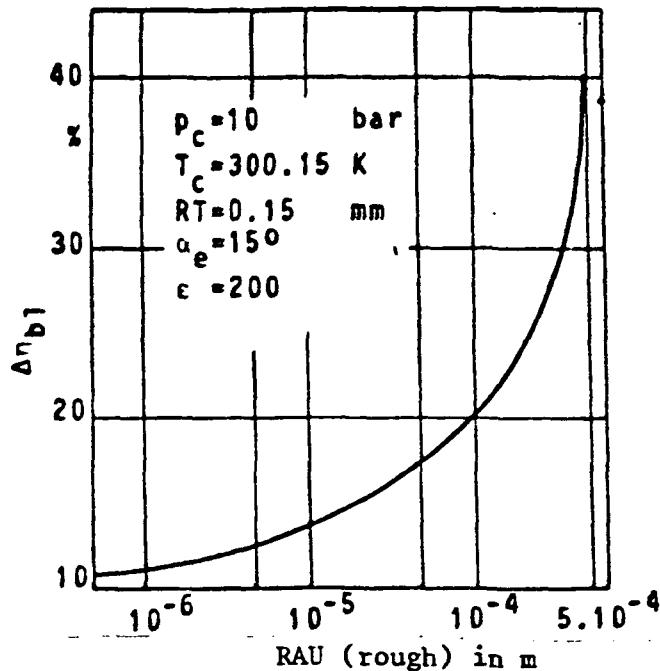
Figure 16   Effect of roughness calculated using pipe friction expression
(REKOR)

Hence, the best suited must be found by measurements [15].

Anticipating the results of the tests here described, we find
that roughness has no substantial effect on $\Delta\eta_{bl}$, which confirms   /45
the approximate expression used earlier. The explanation for
this could be that the relatively large boundary layer thick-
nesses in the case of small diameters extend far beyond the
maximum roughness heights, such that the latter are unable to
develop any large loss effects, i.e., the roughness effects come
to rest within the viscous boundary layer. (Microscopic measure-
ments of the manufactured propulsion units show an absolute
roughness of < 1/1000 mm).

2.2.6 Adaptation losses due to environmental pressure effects   /47

For a given pressure distribution within the propulsion unit,
the thrust can be determined by means of

$$\vec{F} = \int_{(A)} (p_i - p_\infty)\, d\vec{A} \qquad (90)$$

49

Integrating over the entire inner surface of the engine, we obtain, in a scalar decription for 1-dimensional flow,

$$F = \dot{m}c + (p_e - p_\infty) A_e \qquad (91)$$

The first term represents the so-called impulse thrust, while the second term, formed by the pressure difference between the nozzle end and the environmental pressure, determines the compressive thrust portion.

Since the expansion ratio of a nozzle is not infinite at any time, p_e always has a finite value greater than 0. Since in addition in the actual test case p_∞ is greater than 0, the propulsion unit's measured thrust must be corrected to attain the vacuum thrust necessary for performance specific comparisons. An additional precondition to this is that during experimental operation fully formed nozzle flow is maintained, without separation phenomena and compression shock within the nozzle, such as those occurring in the case of superexpanded propulsion units $p_e \ll p_\infty$.

(For large nozzles, the Summerfeld criterion can be applied to good approximation: $p_e > 0.4\ p_\infty$; in the present case this ratio is shifted downwards - see also section 4.2). Since in reality the pressure distribution across the end cross-section A_e is   /48 not constant, a 2-dimensional pressure distribution is used to correct the measured F values, based on the calculation method and the theory described in connection with section 2.2.5.

2.2.7 Heat losses

In contrast to the large chemical propulsion units, which show a substantial decrease in wall temperature along the axial direction, here a homogeneous temperature distribution is assumed. The following boundary conditions must be mentioned, in this context:

a) Large propulsion unit heat capacity

b) Large heat capacity of suspension and supply lines

c) Short test duration

d) Good insulation of the entire assembly in the vacuum chamber

e) Small temperature differences between thrust chamber and environment

f) Radiation loss remains small, due to T_c

As a consequence of the last three points mentioned, heat losses can be neglected, in the comparative calculations for propulsion unit performance. Performance measurements already carried out, in conjunction with high-resolution temperature sensors for the control of adiabaticity, show this to be permissible.

2.2.8 Results of performance prediction calculations

For all the propulsion units examined in the course of the experiments, the most important thermodynami and fluid dynamics parameters were determined using the EGVP procedure introduced. For better visibility (and also due to efficiency considerations), these parameters were plotted as a function of ϵ, using a specially develeoped boundary layer program (or alternatively, as a function of the nozzle axis coordinate).

Figure 17 (page 52) shows the pressure, temperature, viscosity   (/50) and density for nozzle No. 2, as an example. In addition, both in this and the two subsequent diagrams the nozzle shape was also drawn in.

Figure 18 (page 53) represents the changes in the core flow   (/51) velocity, Mach number and laminarization parameter, as a function of the nozzle length z [45,46].

The courses of the boundary layer parameters shown in Figure 19 (page 54) show that the boundary layer thickness in the throat
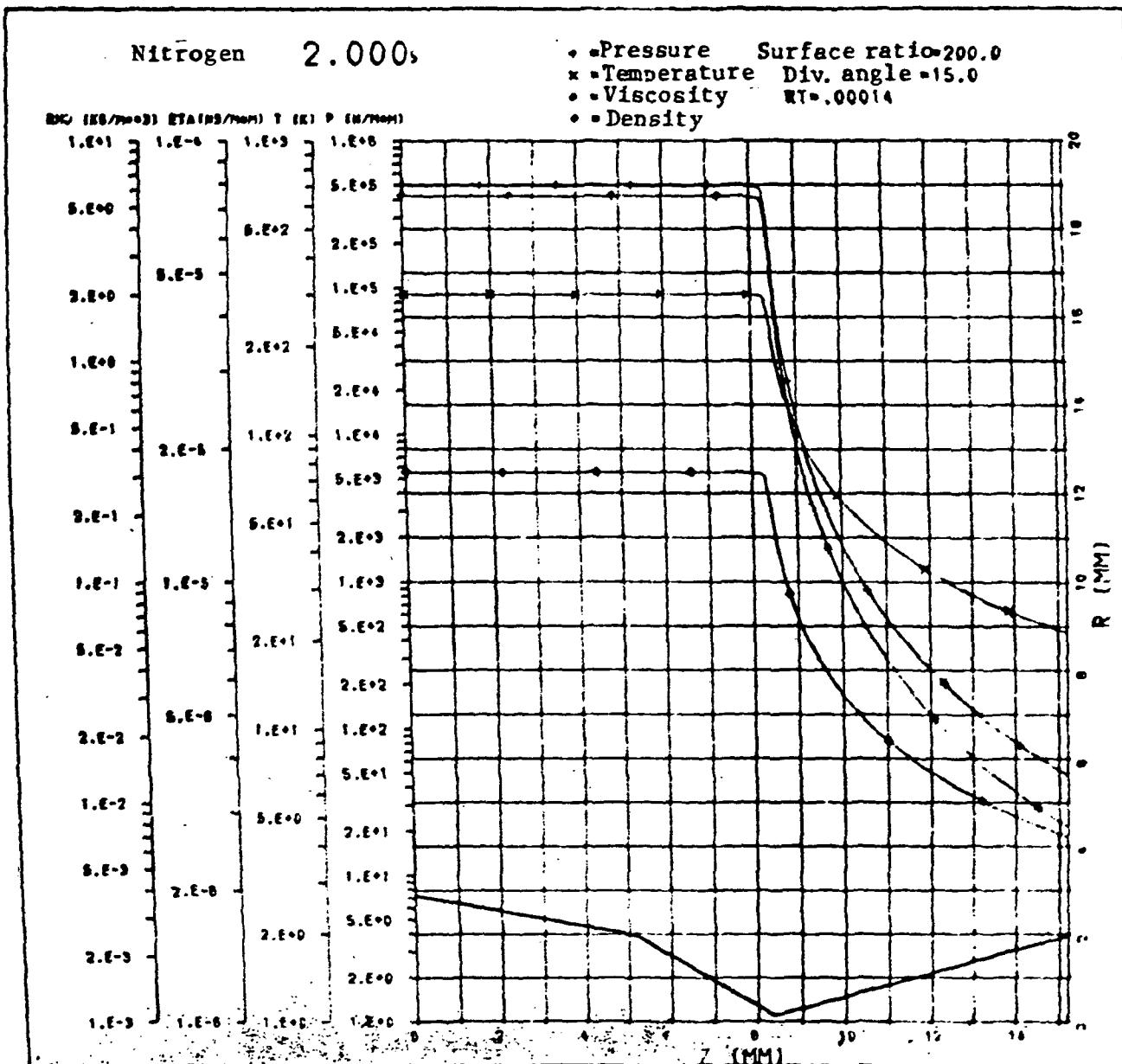
Figure 17 Course of the pressure, temperature, viscosity and density
in nozzle No. 2

has been reduced to practically zero, in the convergent portion
of the nozzle, by the predominating strong acceleration of the
gases in the previous range (see also section 2.2.5.2.3).

With the two velocity profile expressions introduced in section   (/52)
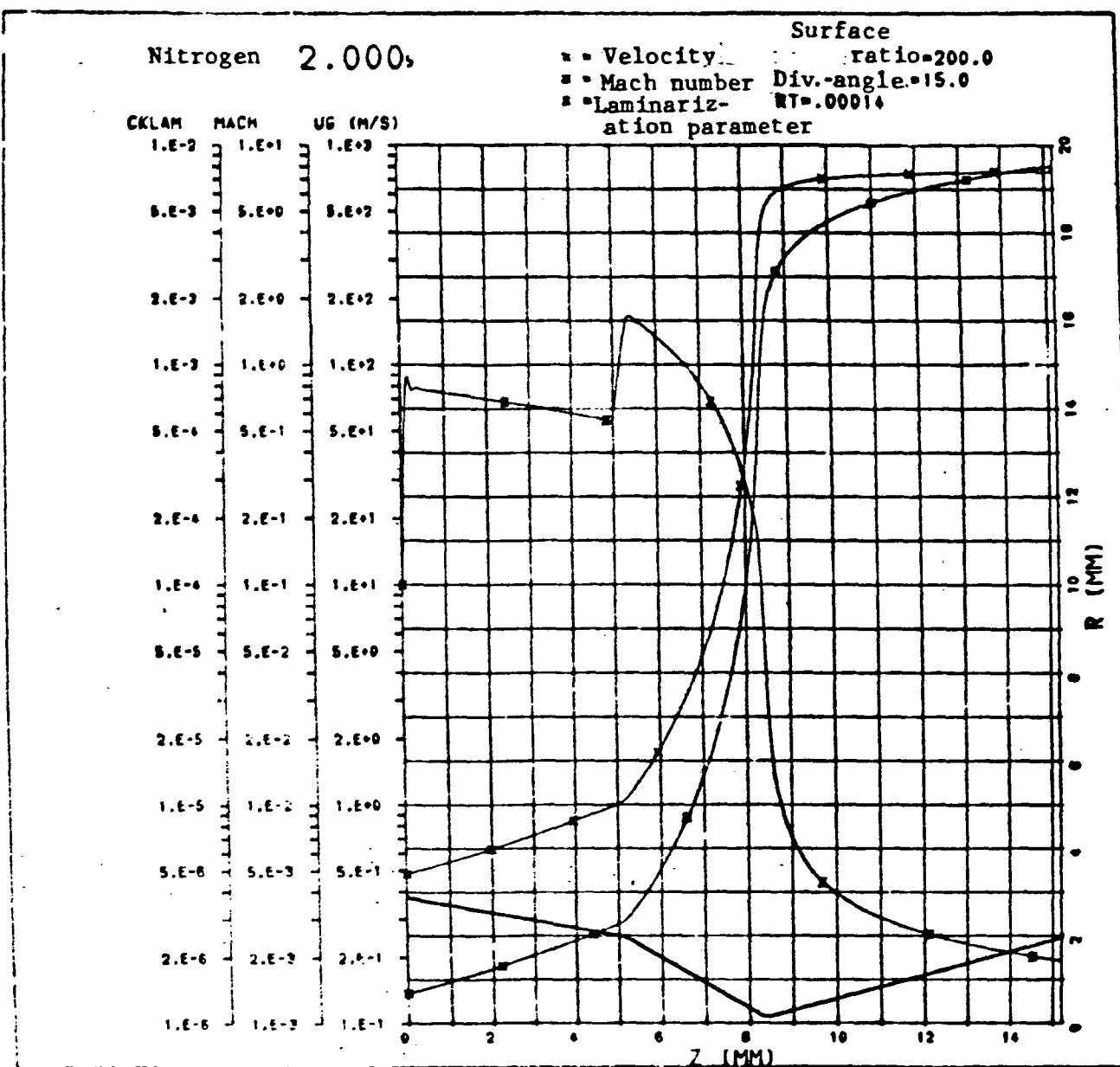
Figure 18 Course of the core flow velocity, Mach number and laminarization parameter K_{acc} along the nozzle axis (Nozzle No. 2)

2.2.5 and with p_c as parameter, Figure 20 (page 55) shows typical boundary layer losses, using nozzle No. 2 as an example. It can be seen that the linear and polynomial velocity expressions have no qualitative effect on the results. As p_c increase, there is a considerable decrease in $\Delta\eta_{bl}$ losses. The quantitative difference (a factor of approximately 2) is based only on the expression
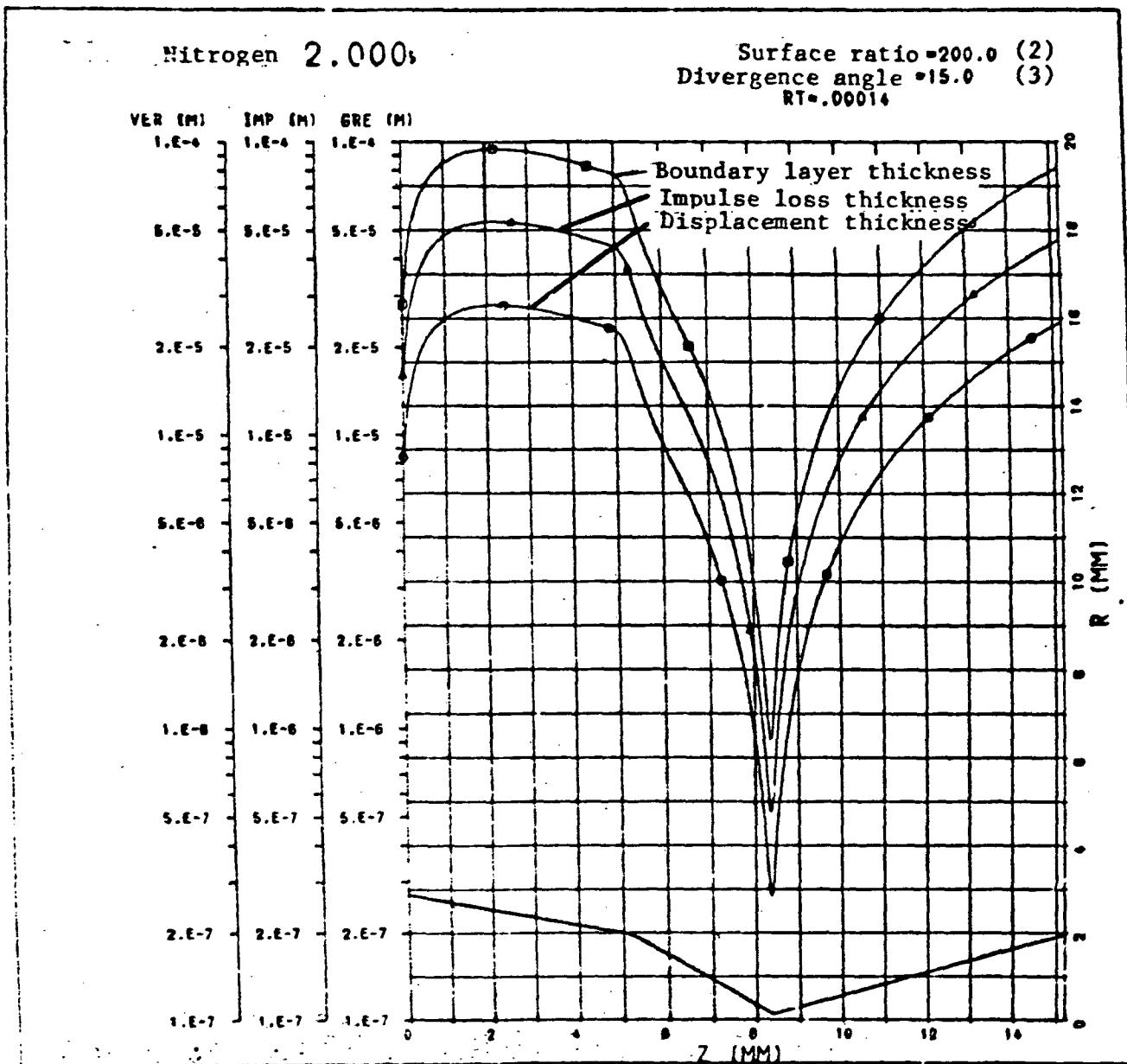
Figure 19 Boundary layer parameters δ, δ^*, θ as a function of z

of Λ and can be readily adapted (see also section 2.2.5.6).

Figure 21 (page 56) provides a comparative representation of   /53
the losses $\Delta\eta_{bl}$ in various media. Qualitatively, the boundary
layer losses as a function of ϵ can be interpreted as reflecting
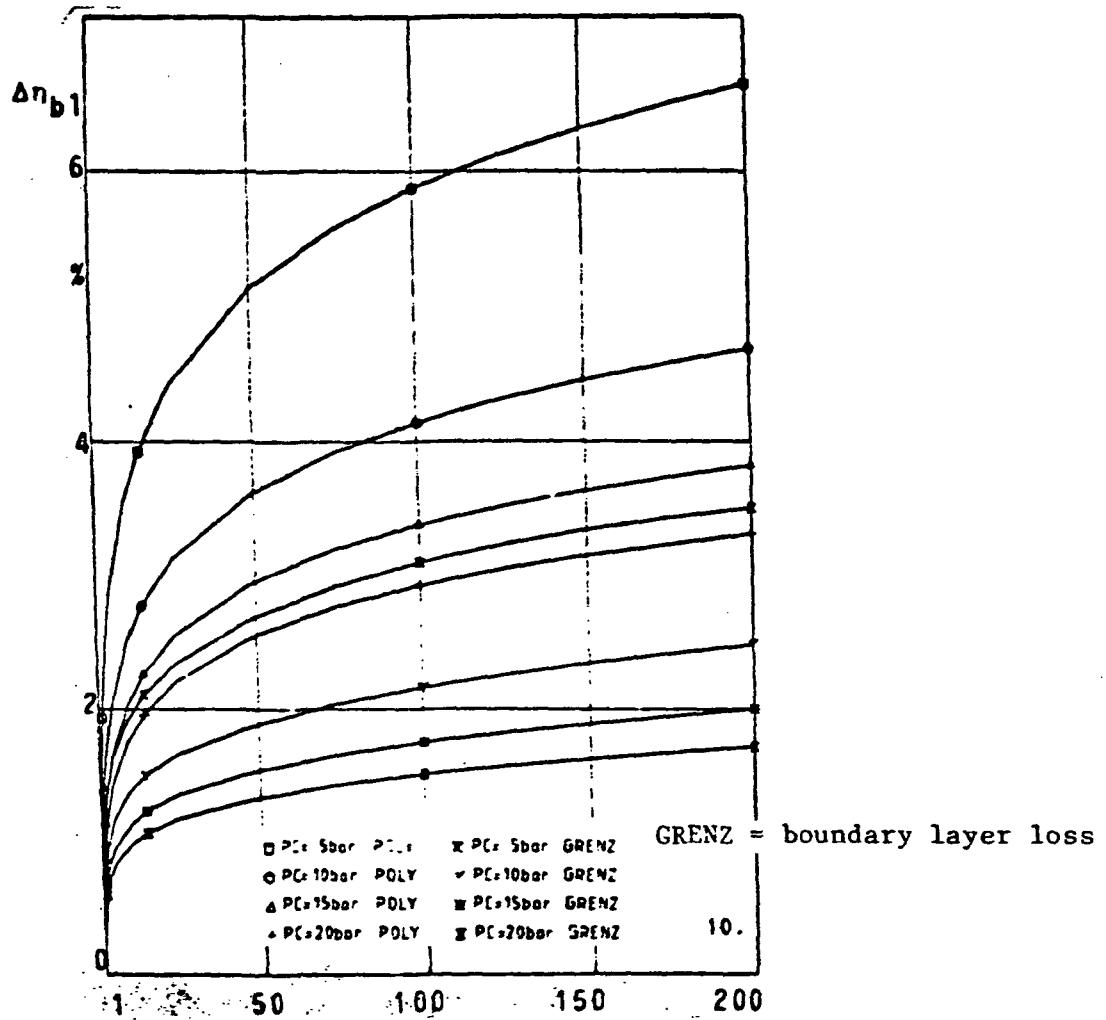
Figure 20 Boundary layer losses without roughness correction

the effect of the different viscosities (see also section
2.2.10). The only exception to the general trend (increase of
$\Delta\eta_{bl}$ for increasing ϵ) is that of the curve for $(N_2H_4)_{x_{dis} = 1.0}$
Due to the strong cooling of the originally fully dissociated
ammonia, a recombination to NH_3 is initiated, with the simul-
taneous release of energy, allowing the gas better expansion
performance. Consequently the $\Delta\eta_{bl}$ losses decrease, percentually.

In contrast to large propulsion units (F-1, J-2, SSME), an addi-   /54
tional design optimization is necessary with small propulsion

55
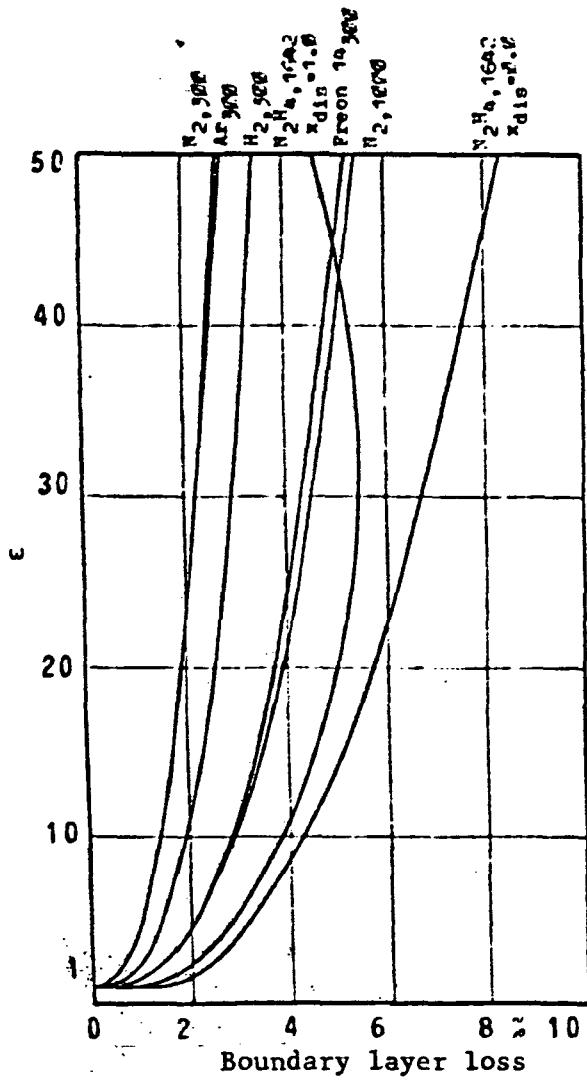
Figure 21   Surface ratio as a function of boundary layer loss for various types of gas. $\alpha_e = 15°$

units, because of the greater influence of the boundary layer losses: the optimization of the surface ratio ε with respect to η_{TD} and η_{bl} (not to be confused with the ε-optimization of carrier rocket propulsion units with respect to $p_\infty = f(H)$ and $p_e = f(p_c, \varepsilon, t, H)$). In general the $\Delta\eta_{TD}$ losses increase with increasing α_e. Since the specific impulse $I_{so,ODE,vac}$ steadily increases with increasing ε, an optimization calculation has to be performed to obtain the optimum ε. This must be followed by

56
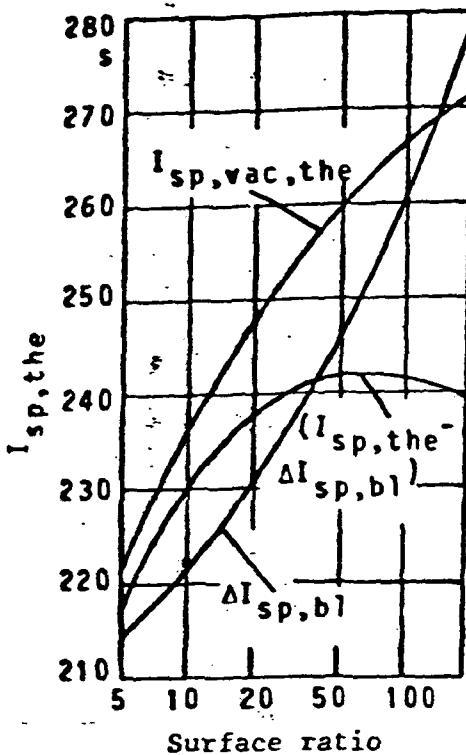
Figure 22   Boundary layer loss effect on the determination of the
optimum surface ratio (N_2H_4, r_t = 0.3 mm, α_e = 15 °)

a second optimization, to take the influence of α_e into account:
while at an assumed constant ε, for an increase in α_e, $\Delta\eta_{TD}$ becomes
larger (conical nozzle), at the same time the absolute cone length
decreases and hence the development of the boundary layer is fore-
shortened. The mathematical formulation is

$$I_{sp,ODE,vac} \cdot \left[1 - \frac{\eta_{bl}}{100} \right] \cdot \left[1 - \frac{\eta_{TD}}{100} \right] = I_{sp,max,vac} \tag{92}$$

or

$$\frac{d}{d\varepsilon}\left[I_{sp,ODE,vac} \cdot \left(1 - \frac{\eta_{bl}}{100} \right) \right] = 0 \tag{93}$$

Figure 23 (page 58) shows the result of the ε_{opt} study for the
N_2H_4 nozzle, as an example (56 ÷ 63).

57
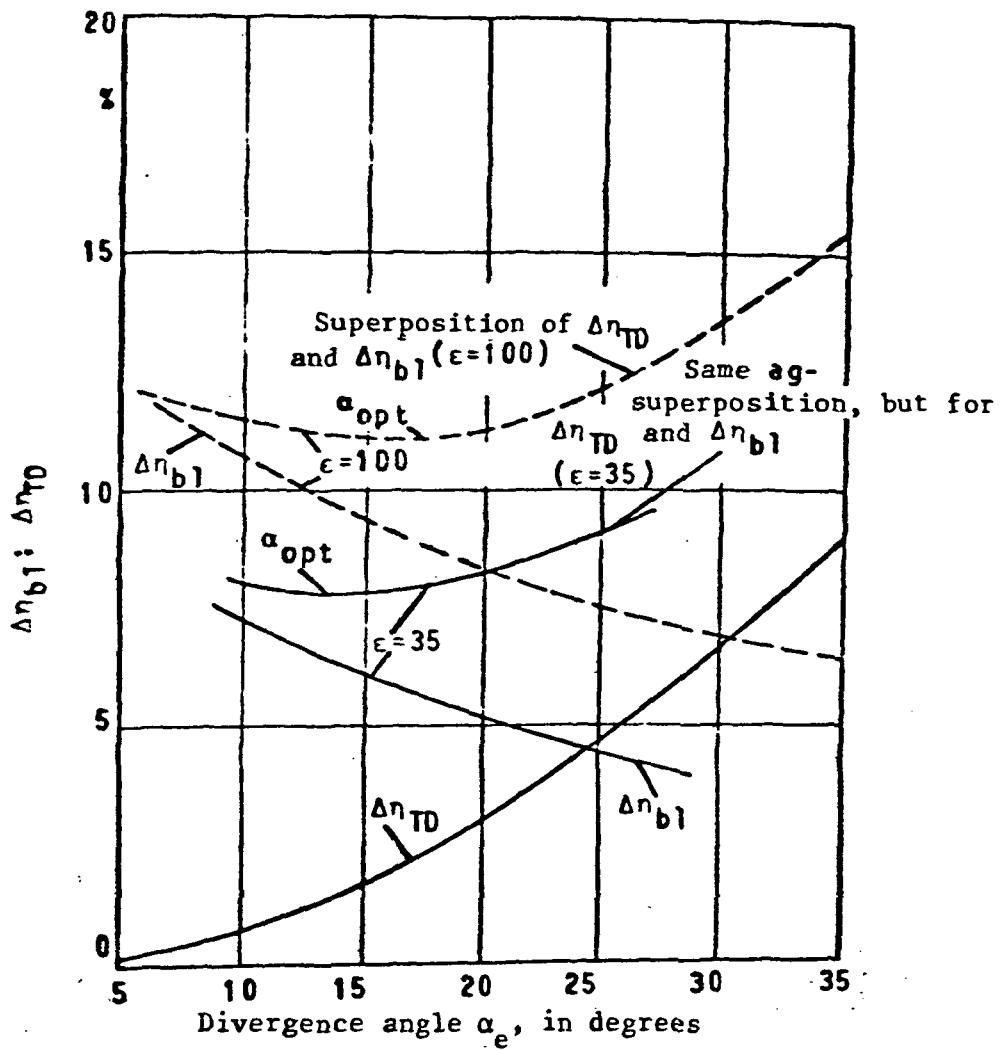
Figure 23 Optimum divergence angle taking the boundary layer and multi-
dimensional losses into consideration, with ε as parameter (N_2H_4)

Since the optimized $I_{sp,del}$ curve shows a very flat maximum at
$\varepsilon = 80$ approximately, and in addition the effect of various
errors is restrictive (for instance, the true degree of dissocia-
tion and the recombination behavior as a function of the expansion
and the residence time in the TW [Triebwerk = propulsion unit],
a fairly large bandwidth must be assumed here.

Figures 24 and 25 (pages 59 and 60) show the optimization   /56
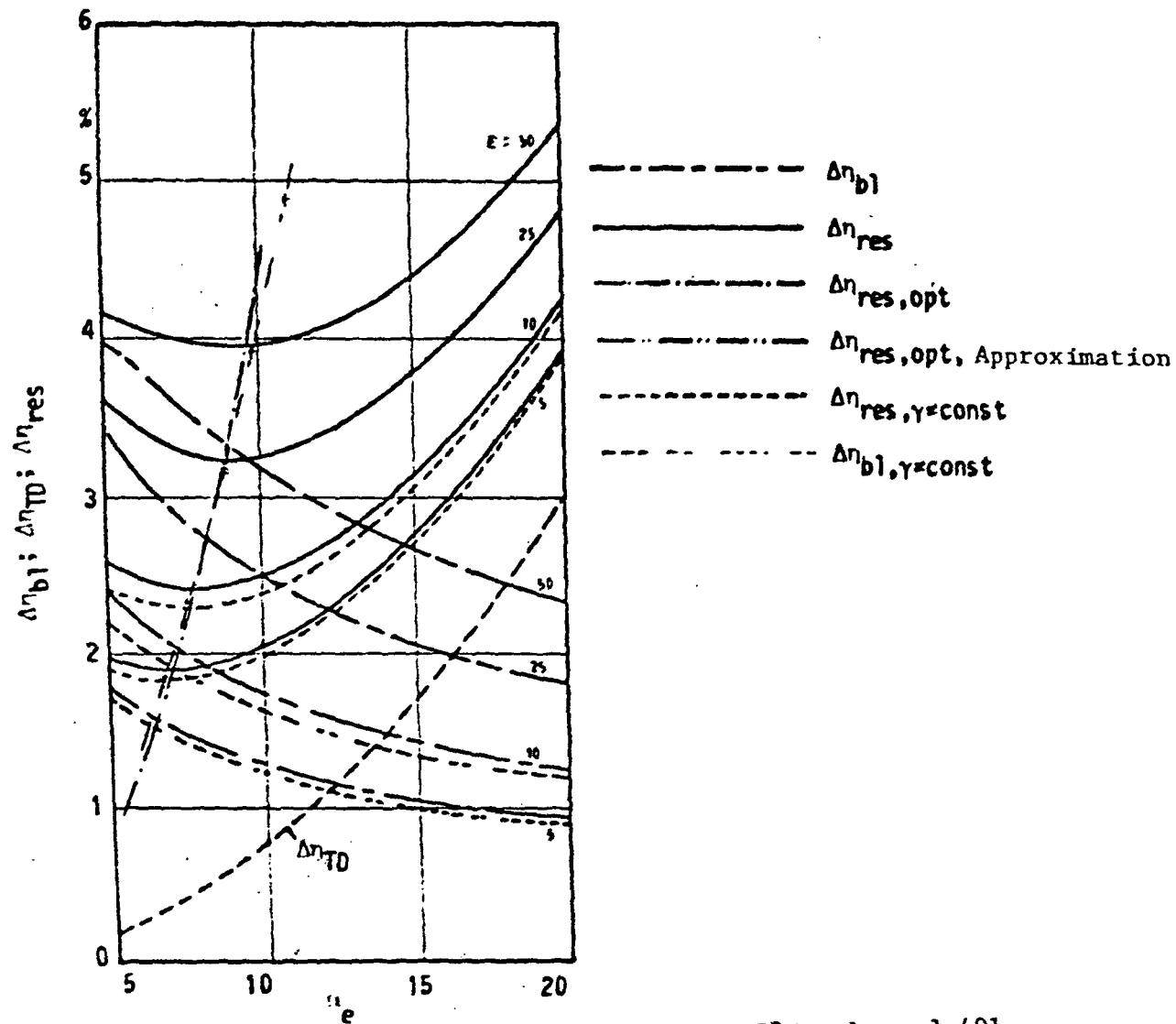
Figure 24 N_2 losses as a function of α_e, at $T_c = 300.15°K$ and $\gamma = 1.401$ and $\gamma \neq const$

results for nitrohen. In addition to the line connecting the corresponding ε_{opt} points according to the explicit theory, Figure 24, above, also shows the line obtained connecting the points resulting according to the simple approximation equation (see section 2.2.10). The good agreement is apparent. The computation time decreases by three orders of magnitude, in the process. Figure 25 (page 60) shows the resulting ε_{opt} values, as a function of r_t, for a constant value of α_e. Due to the low
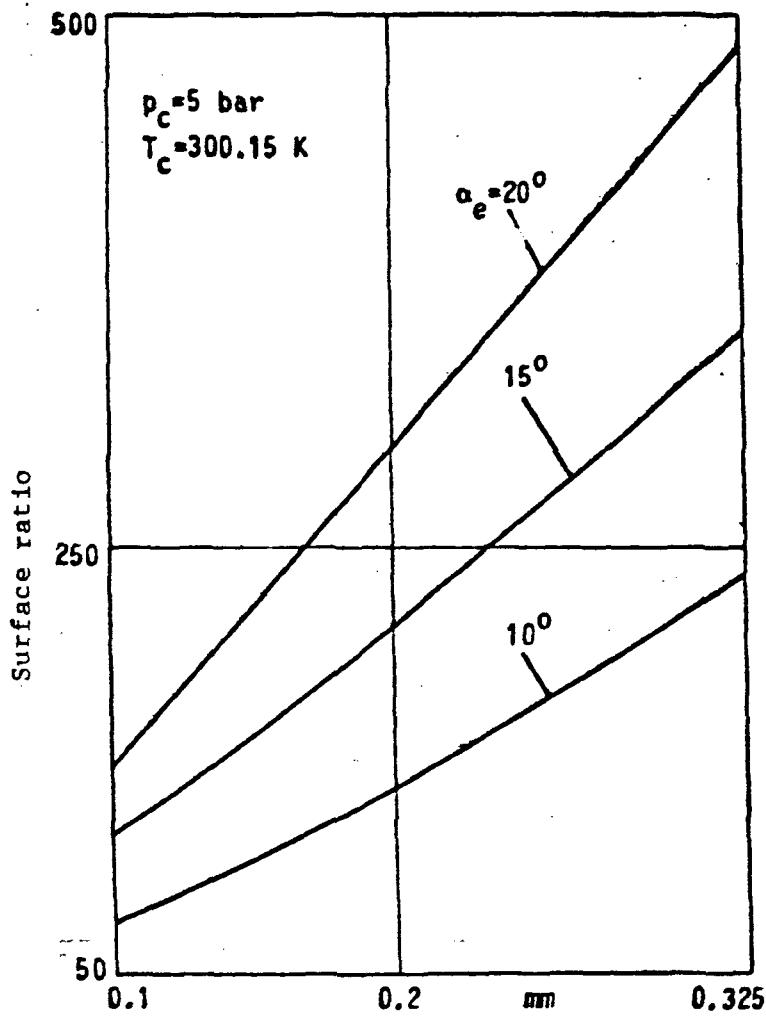
Figure 25 Optimum surface ratio

viscosity of N_2 in comparison to, for instance, H_2 or N_2H_4-decomposition products, the optimized *surface ratio becomes displaced towards larger values.*

2.2.9 Comparison of the results presented in section 2.2.8 with   /58
      those from other procedures (Cline, BLIMP [Boundary Layer
      Integral Matrix Procedure])

The flow mechanics quantities calculated by the EGVP program
- pressure p_g, temperature T_g, velocity u_g and Mach number M -
are compared to those from the program VNAP (Cline [22,23,153]),

a program for 2-dimensional, compressible, time-dependent, fully
viscous nozzle flow. Figures 26 to 29 (below and pages 62-64)
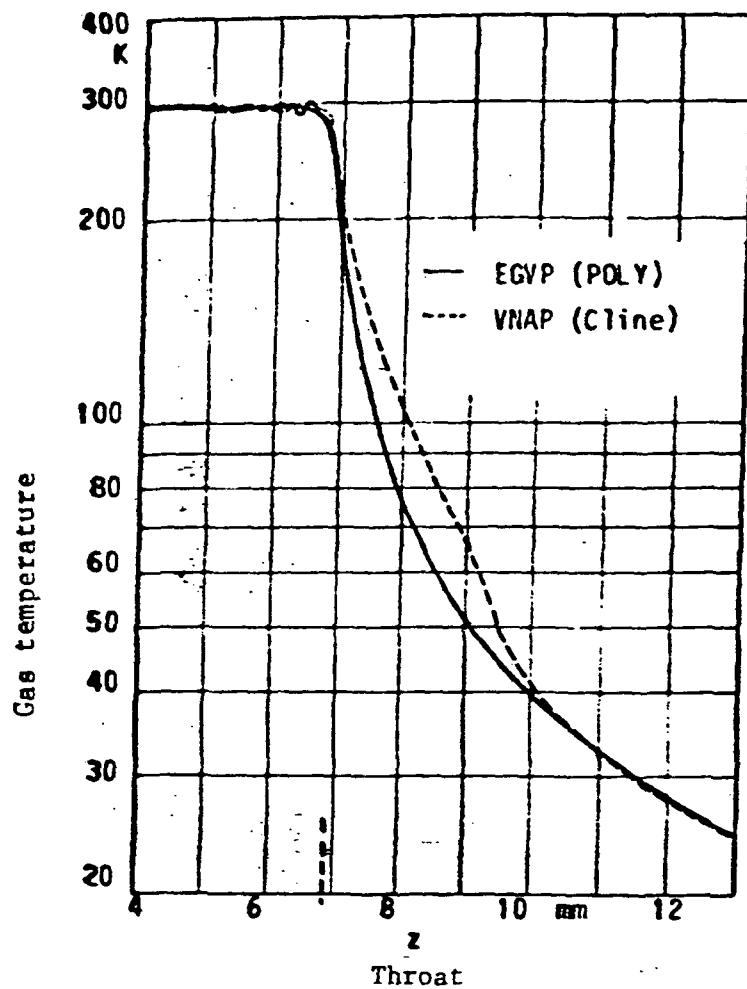
Figure 26   Comparison of programs EGVP and VNAP with respect to T_g, for
N_2 nozzles

show the results. In the calculations with VNAP, the values of
the core flow present discontinuities just before the nozzle
throat; at high surface ratios they coincide with the values
calculated by EGVP, which also shows good agreement in the
throat region [50].

We have no explanation for the oscillations before the throat, in
the values calculated by VNAP. The departures behind the throat
could conceivably stem from the fact that VNAP uses only a throat
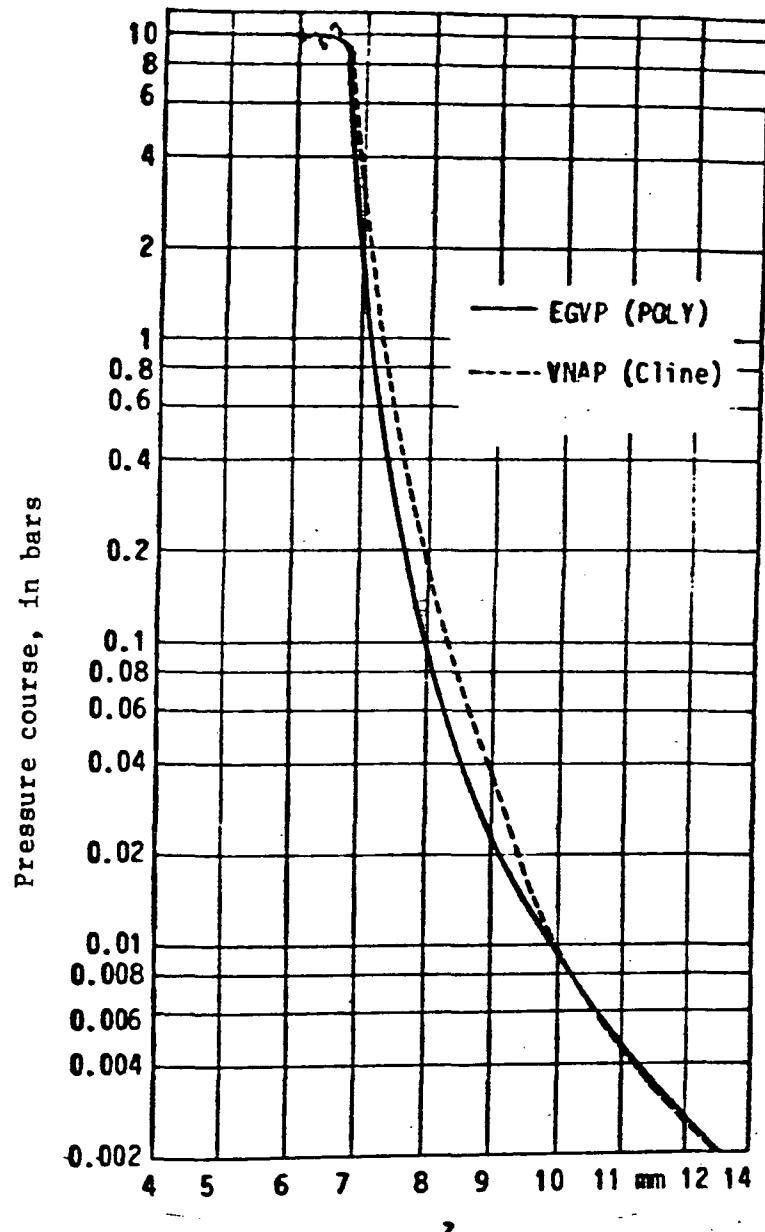
Figure 27   Comparison of the programs EGVP and VNAP with respect to the
course followed by the pressure

transition radius and hence is unable to describe the optimum
nozzle geometry with sufficient precision [70,102,105,106].

Since both the EGVP and the VNAP programs determine fully viscous
flow mechanics data, and since $\Delta\eta_{bl}$ can be derived from them, we
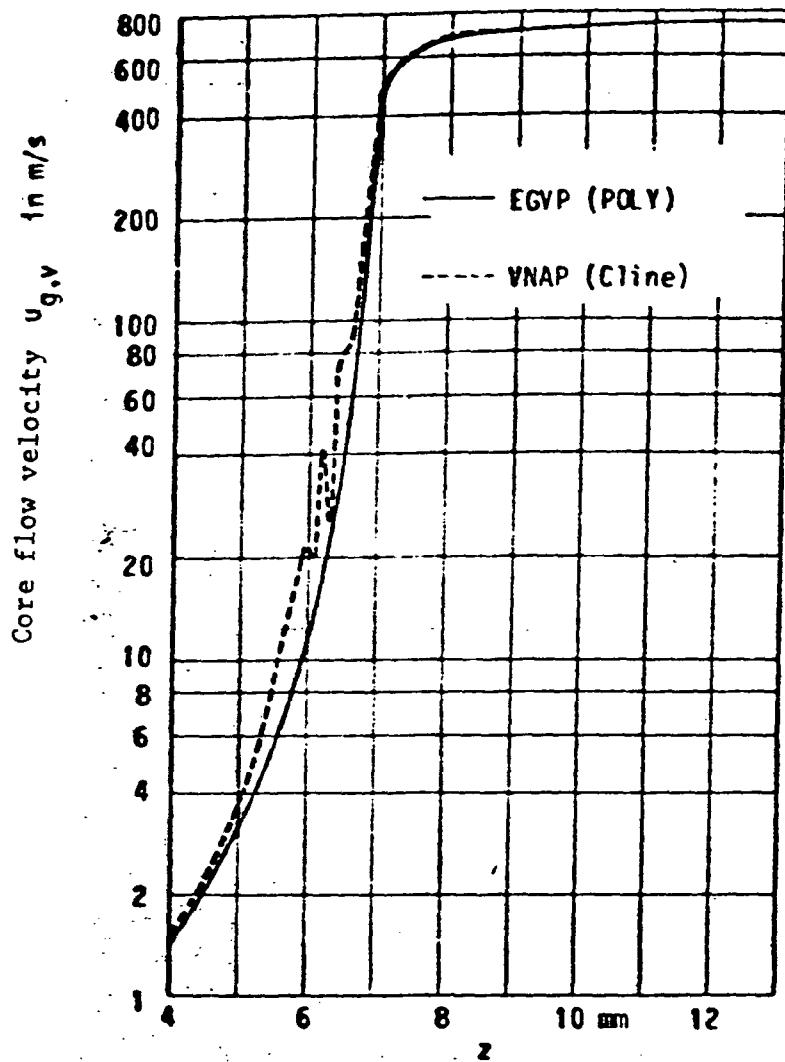
Figure 28 Comparison of the programs EGVP and VNAP with respect to the
core flow velocity $u_{g,v}$

conclude from the agreement of u_g, M, p_g and T_g found above, that
the boundary layer development is comprehended with a similar
degree of agreement.

While work with the Cline procedure seemed relatively simple,
due to correct program listings and a very precise description
and good collaboration with the author, this can unfortunately
not be extended to the second main comparison program, BLIMP
[16,113].

Through at first fortunate circumstance, the Boundary Layer
Integral Matric Procedure (BLIMP) reached the Chair for Space

63
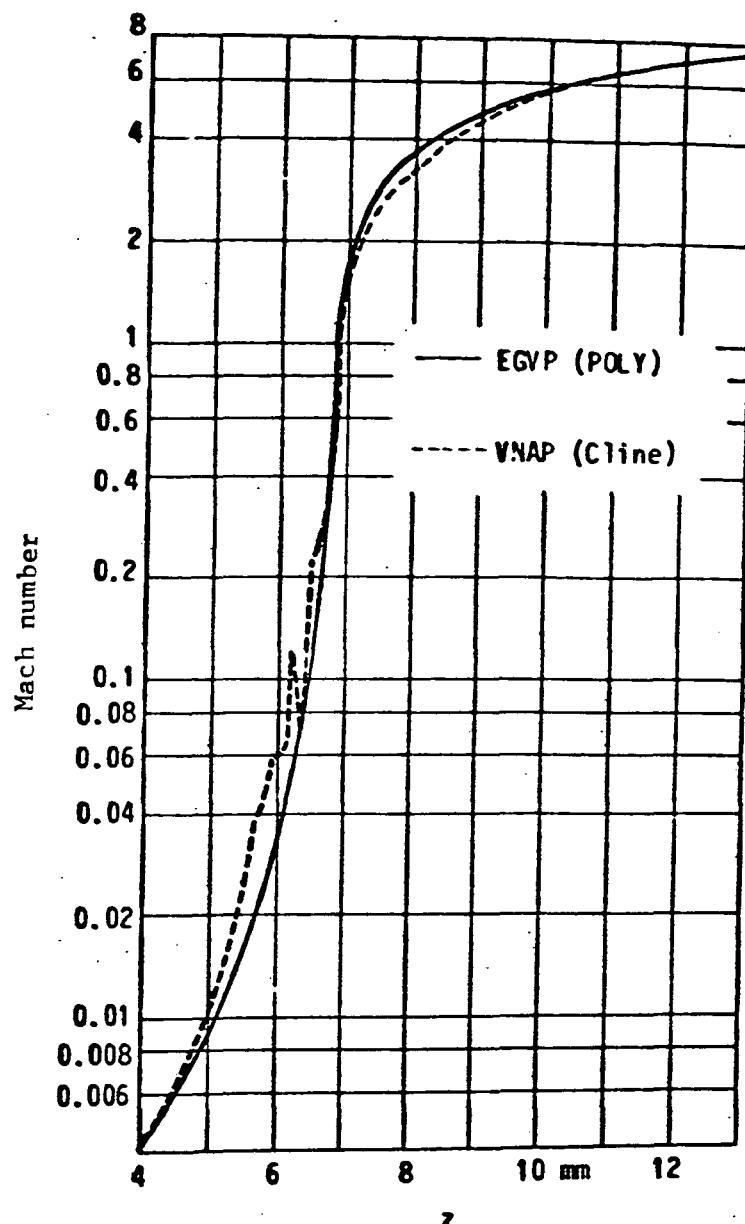
Figure 29   Program comparison EGVP-VNAP with respect to the
Mach number

Technology. This program had been developed during the Seventies
in the US, involving large expenditures in materials and leading   /59
specialists, in the context of JANNAF, for application to many
gas dynamics problems: from the flow over a flat surface under
subsonic conditions, to 3-dimensional, non-stationary supersonic
flow in rocket propulsion units. Since the documentation is
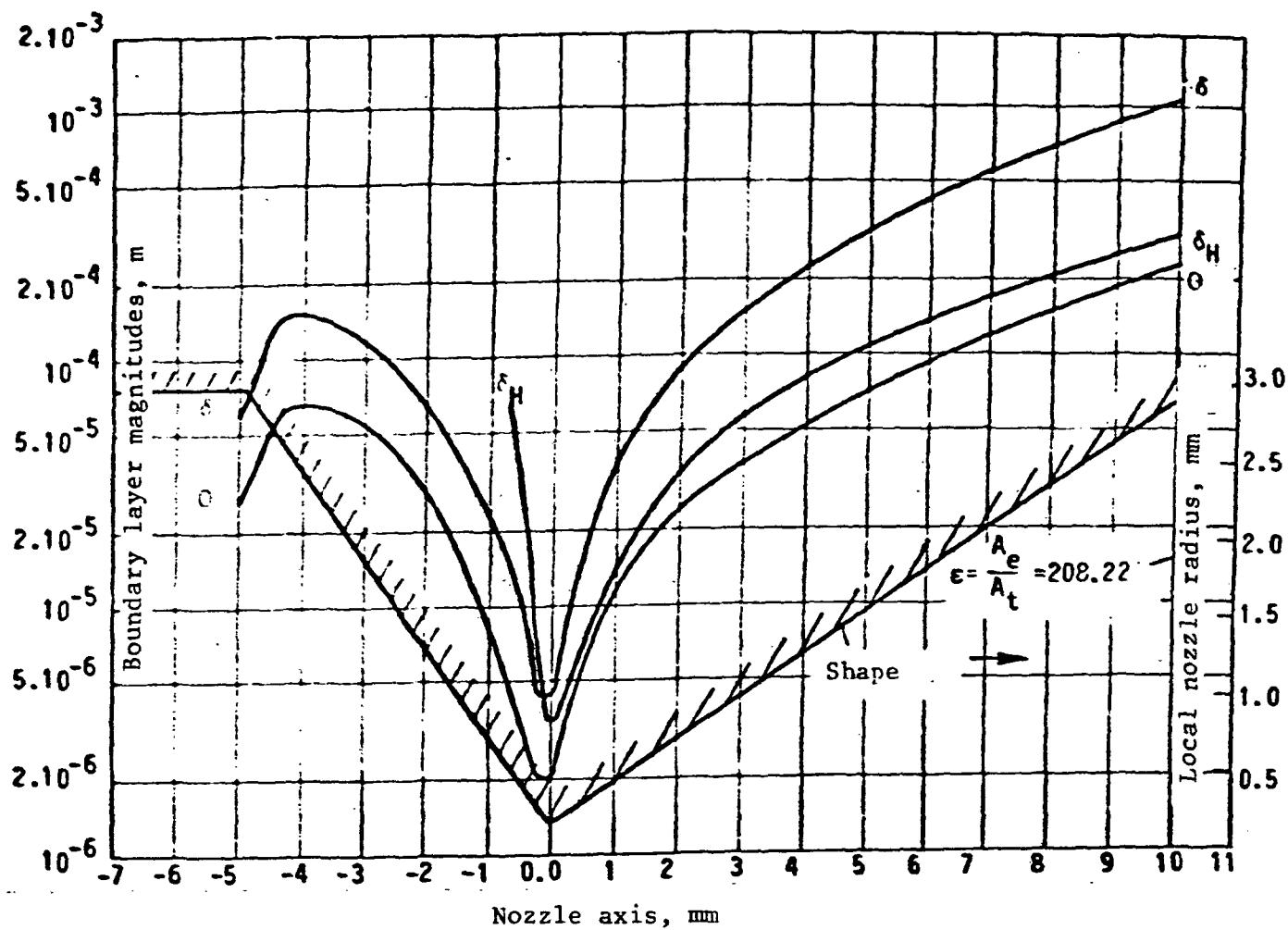
Figure 30   Course of boundary layer parameters obtained using BLIMP
p_c=10 bar; T_c=2300 K; r_t=0.2 mm; α_e=15°; N_2H_4

insufficient and additional, machine-specific problems arose at
the Leibnitz Computer Center of the Bavarian Academy of Sciences,
we have to date been unsuccessful in our attempts to use the
BLIMP program at the Technical University Munich. The example
shown in Figure 30, above, was obtained directly in the US. It
shows the boundary layer quantities δ, θ and δ_H (energy thick-
ness) for a combustion chamber pressure of 10 bar, T_c = 2,300 K,
r_t = 0.2 mm, α_e = 15° and N_2H_4 (decomposed and heated). With the
help of the energy thickness δ_H (see for instance Truckenbrodt
[161]), it is possible to provide more comprehensive $\Delta\eta_{bl}$ loss

statements than with δ*, otherwise (EGVP) used here. The mathematical formulation follows a similar principle and causes no additional problems. The comparison of BLIMP and EHVP data in regard to N_2H_4 propulsion units shows sufficient agreement, and hence additional justification for the simplified EGVP procedure and the system developed in section 2.2.10 is not necessary. It must still be remarked that a BLIMP calculation requires an initial data set provided with the aid of ODE, ODK (Gordon McBride) and TDK. After the first run of the BLIMP system the nozzle shape is corrected and the procedure is repeated. Customarily satisfactory convergence is established after two passes. Depending on the geometry and the reaction chemistry, the computer time required varies from 30 min to 2h CPU time. For comparison purposes, EGVP requires from 5 to 30 seconds.

2.2.10 Simplified performance prediction model

While the computer program for predicting the performance of small rocket propulsion units, described in the preceding section, is considerably more modest, in regard to computer time and expense (by a factor of 100, compared to BLIMP), it still does not satisfy the criteria of simple engineering "rule of thumb" equations. This shall be attempted in the example of boundary layer losses, below.

2.2.10.1 Derivation of the approximation equation $\Delta\eta_{bl}$

The starting point is also the impulse equation, slightly modified for 1-dimensional flow,

$$\frac{d\Theta}{dz} = \frac{c_f}{2\cos\alpha} - \frac{\Theta\tan\alpha}{r_t\,\varepsilon^{0,5}}\cdot\frac{3 + 2\,\delta^*/\Theta - M^2}{M^2 - 1} \tag{94}$$

using the Reynolds number related to the impulse loss thickness

$$Re = \frac{p_c\,\Theta}{c^*\,\varepsilon\,\eta_g} \tag{95}$$

and with the viscosity function

66

$$\frac{\eta_{g,c}}{\eta_g} = k_{n,1} \, \epsilon^{k_{n,2}} \tag{96}$$

(The ϵ-dependence occurs because of the application of the ODE theory to T_g/T).

The shearing stress coefficient is determined as

$$c_f = \frac{c^* \, \eta_{g,c} \, \epsilon^{1+k_{n,2}}}{p_c \, \Theta} \, k_{c_f,2} \tag{97}$$

The impulse equation can now be rewritten

$$\frac{d\Theta}{dz} = \frac{c^* \, \eta_{g,c}}{p_c} \, \epsilon^{1+k_{n,2}} \, \frac{1}{\Theta} \, k_{\Theta,1} \tag{98}$$

The surface ratio ϵ is replaced by $\epsilon = k_\epsilon \, (\frac{z}{r_t})^2$. Using $\Theta_o = 0$ (start of integration at the narrowest cross-section), we obtain

$$(99) \qquad \frac{\Theta^2}{2} = \frac{c^* \, \eta_{g,c} \, r_t}{p_c} \, k_{\Theta,2} \int_0^z (\frac{z}{r_t})^{2(1+k_{n,2})} \, d(\frac{z}{r_t}) \qquad \text{or}$$

$$\Theta = \left(\frac{c^* \, \eta_{g,c} \, r_t}{p_c}\right)^{0,5} k_{\Theta,4} \, \epsilon^{(0,75 + 0,5 \, k_{n,2})} \tag{100}$$

We can now determine $\Delta\eta_{bl}$ as

$$\Delta\eta_{bl} = \left(\frac{c^* \, \eta_{g,c}}{p_c \, r_t}\right)^{0,5} \epsilon^{(0,25+0,5k_{n,2})} \, k_{n,bl,1} \, (1+\delta^*/\Theta - \delta^2/2r_e\Theta) \tag{101}$$

Introducing the throat Reynolds number

$$Re_t = \frac{p_c \, 2 \, r_t}{c^* \, \eta_{g,c}} \tag{102}$$

67

the expression for the boundary layer losses can be strongly
compressed:

$$\Delta \eta_{bl} = \frac{k_{n,bl}}{Re_t^{0.5}} \epsilon^k \qquad (103)$$

2.2.10.2 Loss estimates for various working fluids

With increasing Reynolds numbers in the throat region - which
can mean higher chamber pressure, larger propulsion unit dimen-
sions and higher thrust - the boundary layer losses decrease, in
terms of percentage. In contrast, an increase in the surface
ratio also increases the losses. It is important to establish
that the trend of equation (103) remains unchanged, even using
other expressions for c_f. This has made it possible to formulate
available experimental data and the theoretical results of
extremely comprehensive computer programs with the help of a very
simple equation. Hence the design of a future propulsion unit
can be determined very efficiently with respect to the optimum
surface ratio ϵ. The precision of the result of equation (103)
is surely sufficient, if we take into consideration how difficult
it is to determine the other parameters, such as c^*, p_c, T_c, ϵ,
etc. To determine the two constants in equation (103), a series
of available experimental data and voluminous calculations were
performed with the corresponding procedures, for different media.

The results of the determination of correlation coefficients for
various working fluids are shown in Figure 31 (page 69). The
Freon-14 curve lies above those for simple gases, even though
the viscosity of H_s, for instance, is higher than that of CF_4.
Apparently, the explanation for this departure must be sought in
that during the expansion process (and the concomitant cooling
of the gases) CF_4 recondenses to small droplets (boiling point
at 1 bar approximately -130°C), leading to higher loss measure-
ments.

$$\Delta n_{bl} = \frac{k_{n,bl}}{Re_t^{0.5}} \epsilon^k$$
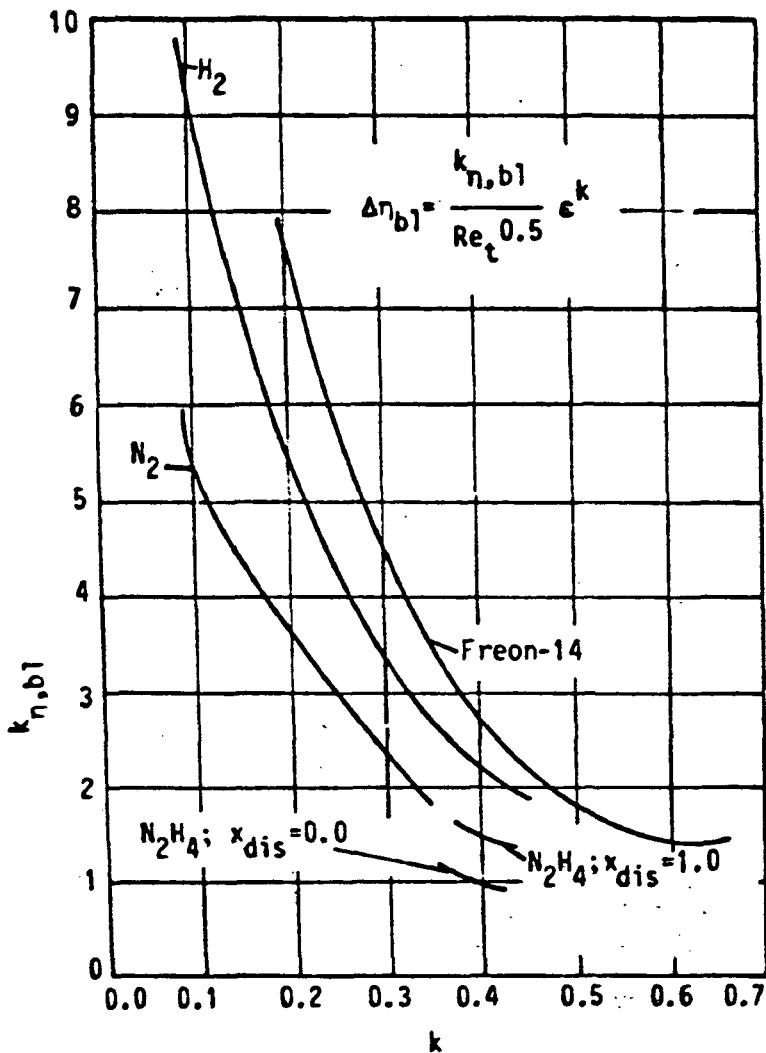
Figure 31   Course of the boundary layer loss coefficients for various types of gases, from available experimental data

In an ideal case, the curves shown in Figure 31 should come to-   /67
gether at one point, for each type of gas. If this does not occur
it is because the diagram was built using many sources, whose
individual results show considerable departures [60]. Because of
the hyperbolic nature of the curves and the mathematical quality
of equation (103) it is possible to insert pairs of $k_{n,bl}/k$ values
(by prescribing ϵ and Re_t), without the boundary layer loss Δn_{bl}
diverging substantially.

69

3 EXPERIMENTS WITH MICROPROPULSION UNITS TO BETTER CORRELATE /68
THE RESULTS OBTAINED IN SECTION 2

3.1 Requirements for the test and measurements facilities

A substantial experimental program is carried out to provide
an underpinning for the results attained in the preceding section,
to measure specific performance quantities in miniature propulsion
units. As can be anticipated from the theoretical results, severe
requirements must be placed on test ·design and measurement preci-
sion, in order to be able to identify the individual performance
losses, for instance due to boundary layer effects.

The development of detailed test facilities must start, in each
case,from the following boundary conditions and physical
quantities:

TABLE 3 Precision requirements for the measurement installation

Thrust range:	10 – 2000 mN ± 1%
Mass throughput:	10 – 2000 mg/sec ± 1%
Combustion chamber pressure:	1 – 20 bar ± 0.3%
Combustion chamber temperature:	290–300 K ± 0.5 K
Nozzle throat diameter:	0.25 – 0.8 mm ± 0.003 mm
Surface ratio:	1 – 200 ± 0.5%
Gas type:	N_2 repurified (99.99% N_2)
Measurement durations:	1 – 100 sec ± 0.1%
Safety	
Reproducibility	
Manufacture of individual components in the Chair's own shops	
Financial context	< 10,000 DM (outside financing)

3.2 Test facility description

Without the Chair for Thermodynamics (Prof. Dr. E. R. F. Winter)

70
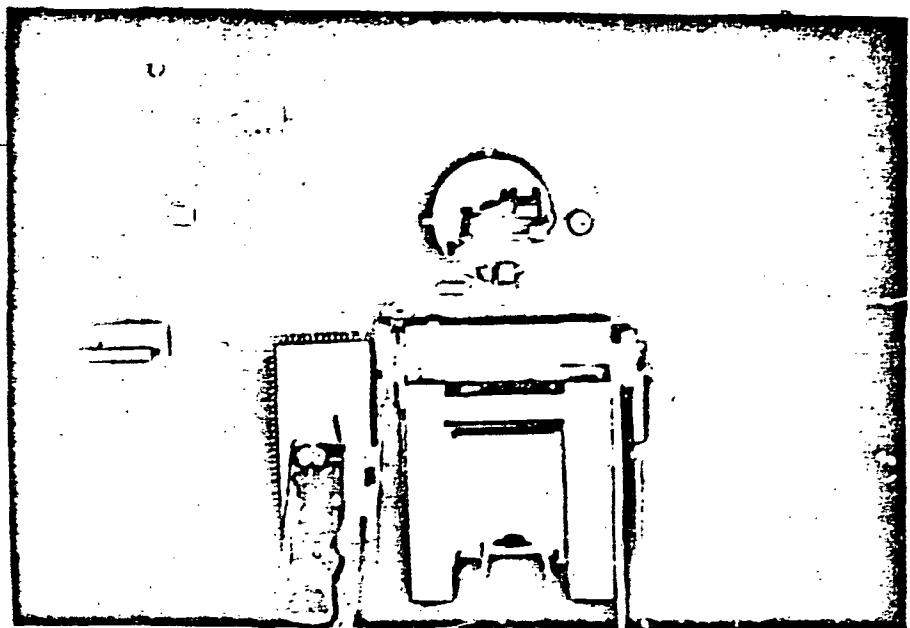
Figure 32   General view of the altitude test stand for cold gas propulsion
units

at TUM [Technical University at Munich] generously providing a
laboratory, due the extreme space scarcity at the Chair for
Space Technology this experimental study in the area of rocket
propulsion unit performance measurements would not have been
possible [55,163]. A massive frame construction was installed in
the already available (as a loan from the DFVLR [Deutsche Forsch-
ungs- und Versuchsanstalt fuer Luft und Raumfahrt = German Research
and Test Facility for Air and Space Flight]) altitude simulation
chamber. This frame holds the propulsion unit's suspension, F-
calibration device, N_2 gas supply, p_c and p_∞ measurement pipes,
temperature sensors and components of the optical thrust measure-
ment arrangement. The Figures 32 (above) and 33 (page 72) show
an overview. The N_2 supply storage (including the $\dot{m}$ measurement
system) is located outside the vacuum chamber, as are the main
components of the thrust measurement system, various electrical
supply devices and measurement value acquisition and processing
[17,20,40,52,74,75,78,98,101,155,168,169,178].
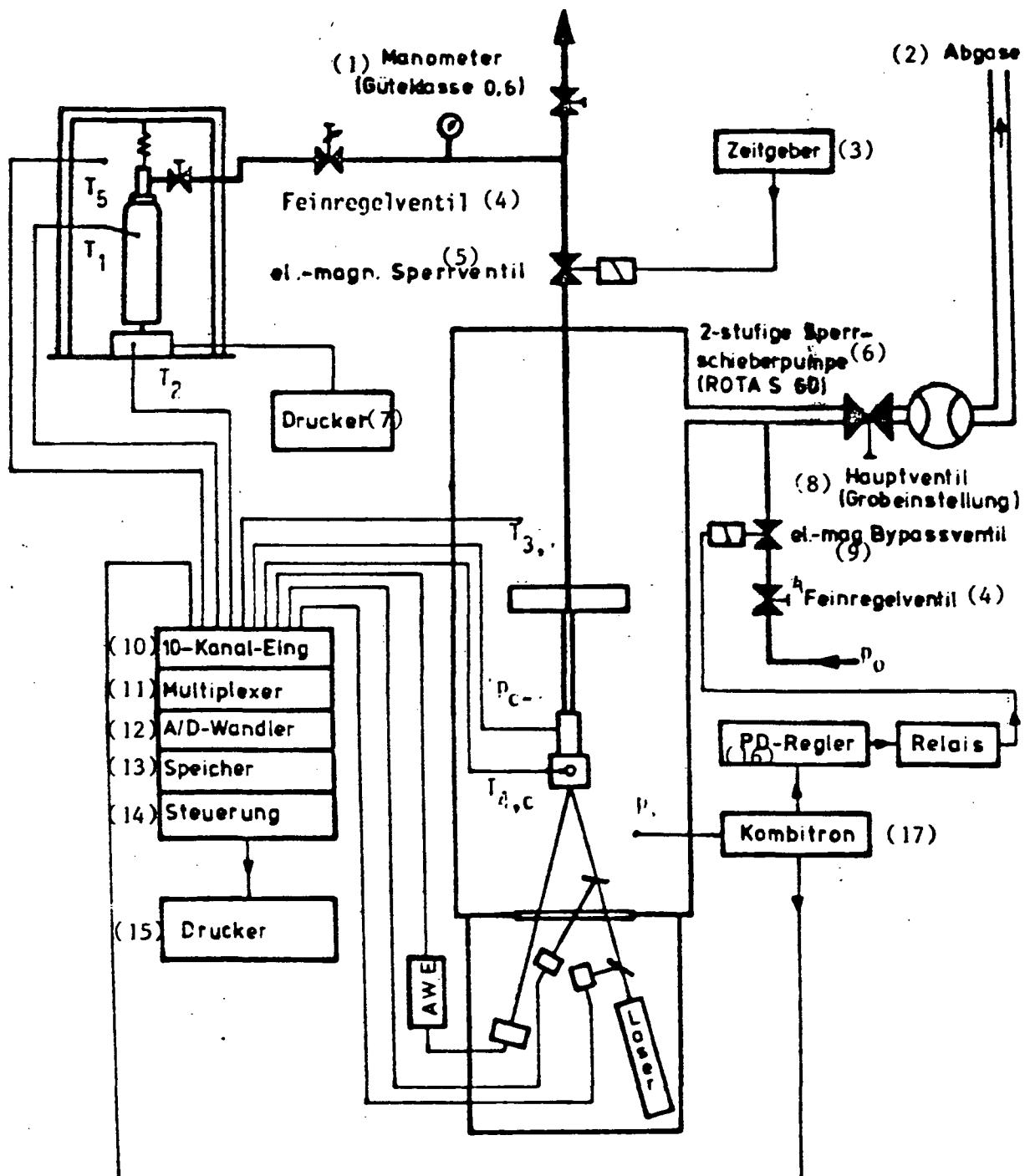
Figure 33 Test arrangement (schematic)

(please see KEY page 73)

3.2.1 Vacuum installation   /71

To compensate for the upthrust of the thrust equipment during calibration of the thrust meaurement system, the environmental pressure in the vacuum chamber (useful volume approximately 150 liters) must be adjusted to the underpressure present during the calibration phase of the "nozzle test run" to be performed subsequently. To this end, the suction of the rotary vane pump (LH-S60) can be adjusted by means of a "bypass" needle valve. A specially developed analog PD regulator (see Figure 34, below)
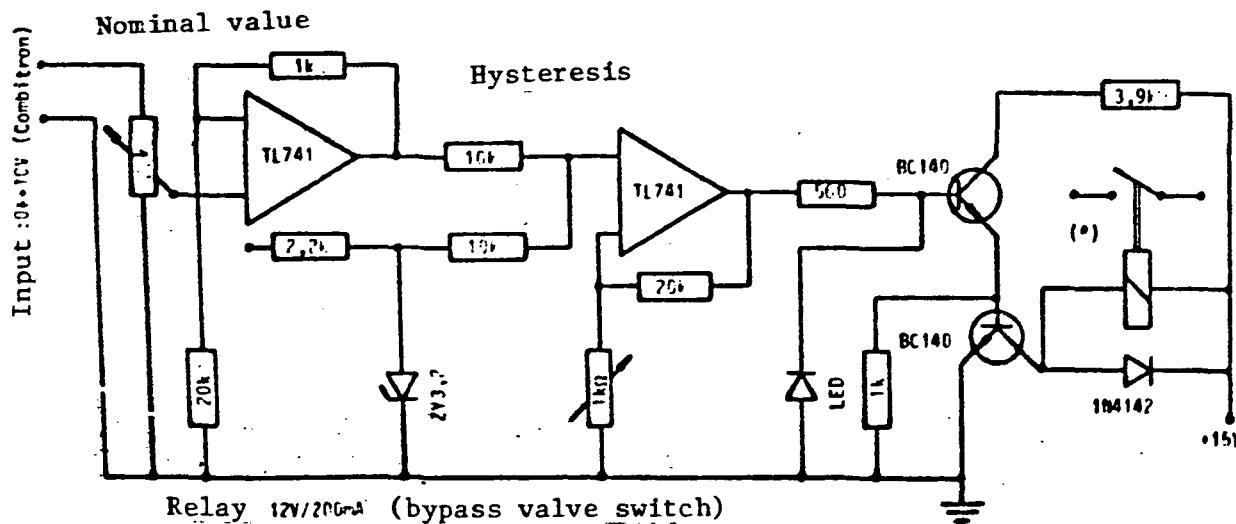
Figure 34   Circuit diagram of p_∞-adjustment (bypass valve control)

controls the "opening" and "closing", respectively, of the bypass admission of external air into the rotating vane pump's suction line. By using LH-Thermovac and LH-Penningvac pressure measurement pipes in connection with the LH Combitron supply and indicator system, the actual value of p_∞ is supplied to the control circuit (Mr. Matthern of DFVLR Oberpfaffen was kind enough

to perform the calibration of the p_∞ sensor system for us).

The p_∞ adjustment makes it possible to achieve a reproducibility of better than 1% in the pressure range of 10^{-2} - 10 Torr here under consideration, which is sufficient with respect to thrust measurement errors due to upthrust effects (see also sections 3.2.2.2 and 4.3).

3.2.2 Thrust measurement system /72

In general the thrust of a rocket propulsion system can be described as the product of the effective discharge velocity and the mass throughput:

$$F = \dot{m}\, c_{eff} \tag{104}$$

While in most test cases the propulsion unit's mass throughput can be determined with reasonable efforts, a direct, precise measurement of c_{eff} is not possible. This is due to the following reasons:

- 3-dimensional distribution of the discharge velocity
- 3-dimensional pressure distribution in the end cross-section
- Condensation shock, flow separation
- Assignment of local density and velocity distribution
- Sensor problems
- Reduced size of the nozzle geometry (in the case to be examined here)

Hence only an integral measurement of F can be used here. Because of the small forces involved, the methods used for large rocket propulsion units - using DMS sensor to measure the deformation of the thrust stand - can not be applied. While inductive displacement pick-ups could measure some of the "large" nozzles (2N) used here, their resolution is limited for the lower thrust

74

range (20 mN), and they can hence not be used. It was decided
not to use torsion balances - as they are used for small N_2H_4
single-component fuel engines (ERNO) - since they aloow the
determination of only the thrust time integral, from the total
torsion angle, rather than the temporal course of the thrust.

Because of the drift problems in the charge amplifiers that would
necessary for the nearly stationary operation case, piezoelectric
sensors can not be used. In addition, to reduce the mechanical in-
fluence of supply lines and calibration devices on the thrust   /73
measurement method, contact-free methods should be included in
a narrower selection.

- Due to the required resolution, it is not possible to
  use radar methods
- Optical interference methods are possible, but very
  demanding in their implementation and difficult in terms
  of measurements evaluation (linearity errors, counting
  problems)
- Optical "edge" and "slit" system were evaluated in pre-
  liminary testing but eliminated because of their strong
  dependence on the light source's intensity value.
- The situation is analogous for systems that translate
  the smallest deflection of thrust transverse beams into
  intensity changes, by means of the displacement of a
  polarization filter
- The F-measurement principle finally chosen is described
  in detail in Figure 35 and 36 (pages 76, and 77):

A simply polarized laser beam strikes a mirror installed on the
propulsion unit's flange, parallel to the thrust direction (first
surface mirror). The thrust frame consists of a cantilever beam
that simultaneously represents the gas supply pipe. At its free
end is the installation flange with the propulsion unit, which
generates a thrust acting vertically downwards. This causes the
pipe to be deformed along its deflection curve bending line,
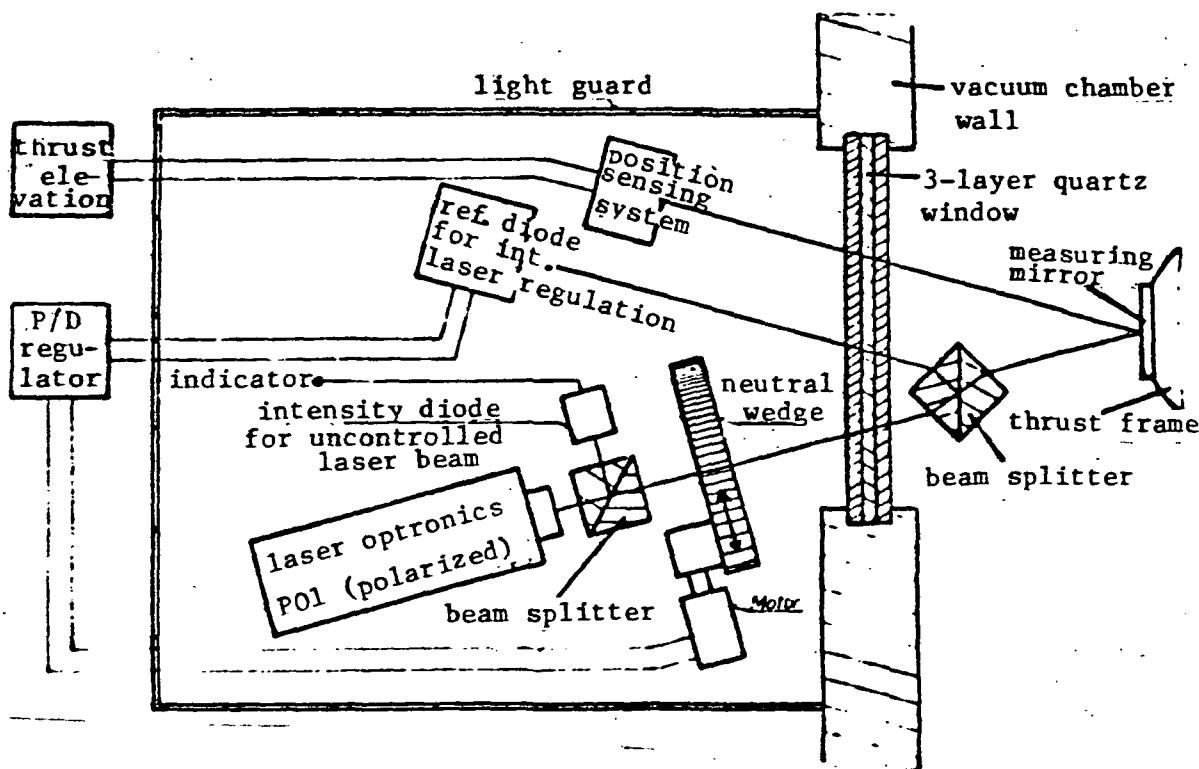
Figure 35 Laser thrust measuring system

such that the mirror alters the angle to the incident and the
reflected beam. Outside of the vacuum chamber the reflected beam
is sent to a homogeneous linear array (LSC-5D, United Technol-
ogies). This beam position measurement probe - which operates on
the Schottky principle - permits a resolution of better than
0.1 µm, using the appropriately adapted electronics (TS-Elektronik
Munich, FRG).

In spite of the required resistance of the bending pipe against   /75
internal pressure (to a maximum of 25 bar), the resolutions allows
dimensioning that pipe in such a manner that in conjunction with
the corresponding optical "lever arm" thrust forces in the range
of 20 mN to 2 N can still be measured with sufficient precision.

76
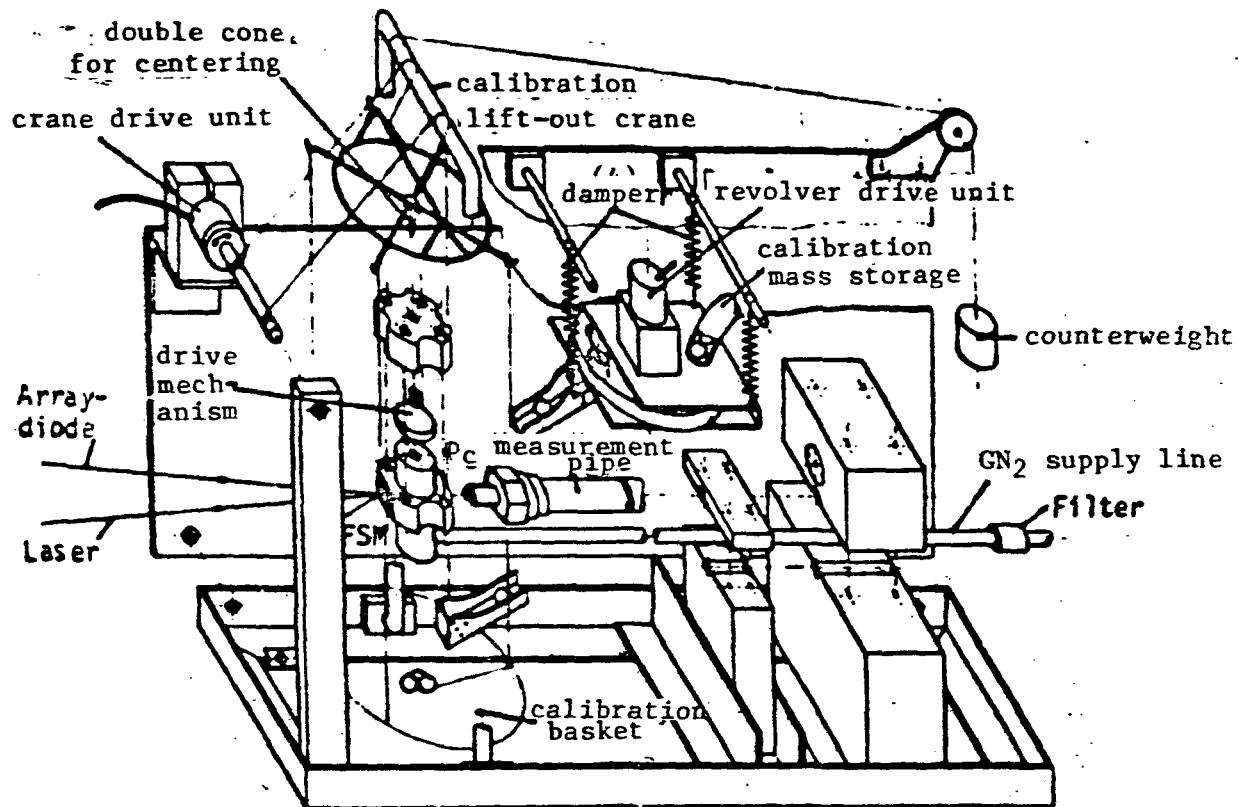
Figure 36 Mechanical test construction within the vacuum chamber (shown iso-
metrically and partially diassembled for better understanding)

Interpretation involves purely elastic resistance expressions,
which after numerous calibration measurements seems to be permis-
sible (se also section 9.1).

Since both the LSC array sensors and the necessary evaluation
electronics still require empirical values from use in day-to-day
laboratory practice - in contrast to the segmented position sensors
already used for longer periods of time - it may be assumed that
the reproducible resolution of the position measurement procedure
can still be improved upon. It does not seem necessary to point
out in detail that the method here presented is also suitable for

larger propulsion units and other problems, in which the recording of very small position changes is necessary. Although in principle the optical thrust measurement procedure is of very simple design, during implementation the edge effects causes problems whose solution is quite laborious.Diffraction and refraction influences of the laser beam, caused by optical windows and beam refraction on gas molecules, can be corrected, or even avoided by the use of polarization filters, quartz windows and the required air density control in the vacuum chamber.

The main problem occurring in the intended experiments is keeping the laser beam intensity constant.

/76
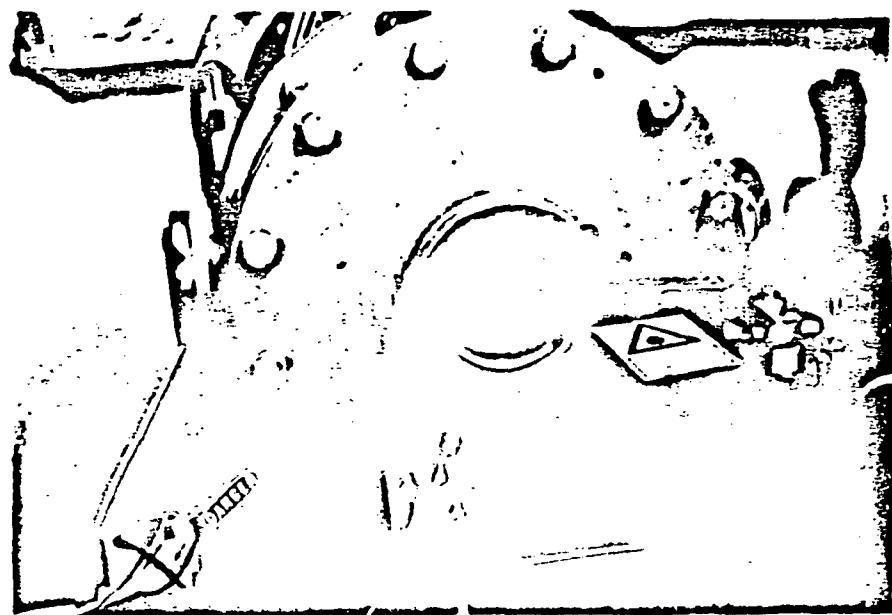
Figure 37   Laser-optical thrustmeasurement system (beam path made visible using smoke. Exposure tine: 4 minites)

78
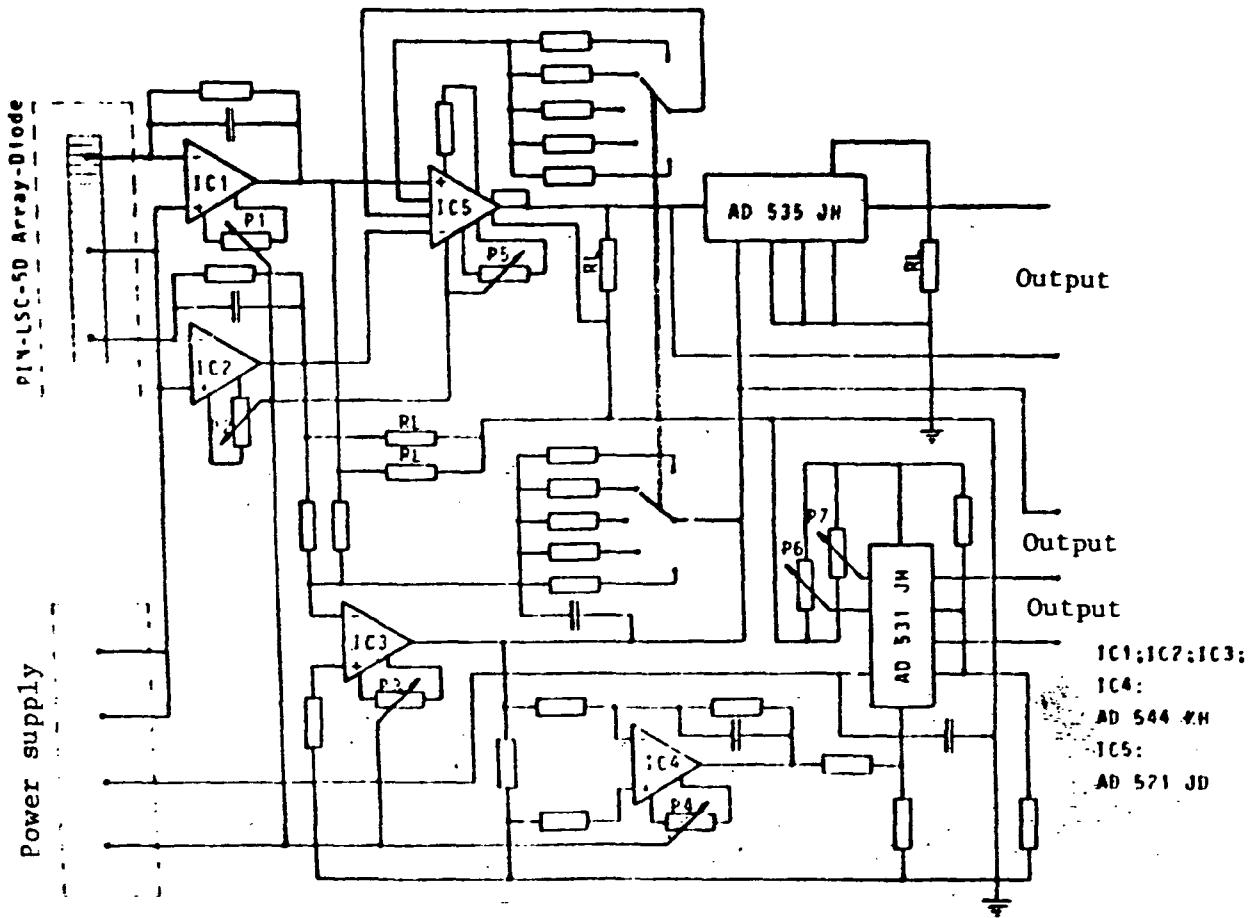
Figure 38 Laser-array diode evaluation electronics

3.2.2.1 Laser intensity control

Long and short-period variations in the laser beam output
intensity are due to line voltage variations (long-term and
short-term), temperature influences and the plasma physics
processes inside the laser tube. In the case of the He-Ne laser
system used here, the amplitude can be up to 2% of the nominal
initial output. In addition, there is the constant degradation
of the beam output due to diffusion of foreign atoms in the gas
laser's glass tube. The array diode deflection measurement
procedure is capable of linearizing and compensating for the
changes mentioned above, in a first approximation (including

the subsequent amplification and evaluation electronics). The remaining higher order interference terms, however, prove to be intolerable in their effect on the resolution and reproducibility of the thrust measurement procedure.

Hence it is necessary to develop a procedure for an active stabilization of the laser intensity. To this end, we first replaced the laser system CWR-LS-05 (with unregulated power supply), by means of the model Laser Optronics LO-101 P, whose power supply reduced the initially necessary ignition voltage of 10 kV, to a continued operating voltage of 1500 V, after the start of operation. In addition, it smoothes out intermediate-term tension variations of the supply line voltage.

We decided against the purchase of a very expensive (nearly DM 30,000) power supply, especially tailored for laser problems, since it can eliminate only certain line influences in the short and long-period fluctuation range, but does not eliminate the thermal variations of the laser intensity, or those due to plasma physics, ultimately. Among them are, for instance, the effects caused by "mistuning" of the laser mirror system at the two tube ends, caused by thermal shifts.

The intensity stabilization system finally used was shown in Figure 35, in schematic form. Via a prismatic beam splitter, 50% of the beam output is deflected towards a photodiode operating in the He-Ne band, as an "actual value" indicator (in order to compensate for the influence of the different gas densities on the diffraction of the laser beam, the beam splitter is arranged within the altitude simulation chamber). In a specially developed PID regulator (circuit diagram below, page 81), the instantaneous actual value of the laser intensity is compared to an adjustable nominal value [40]. When the appropriate adjustment difference occurs ($\approx$ 50 μV) it is amplified sufficiently so that a micro-metric control can be set in motion via a down-stream, direct current minimotor. On this mechanically prestressed control (to

symmetrical
power supply

nominal value
adjustment

PID regulator

end output stage
(neutral wedge drive)

input amplification

actual
value
U_e(photo
diode)
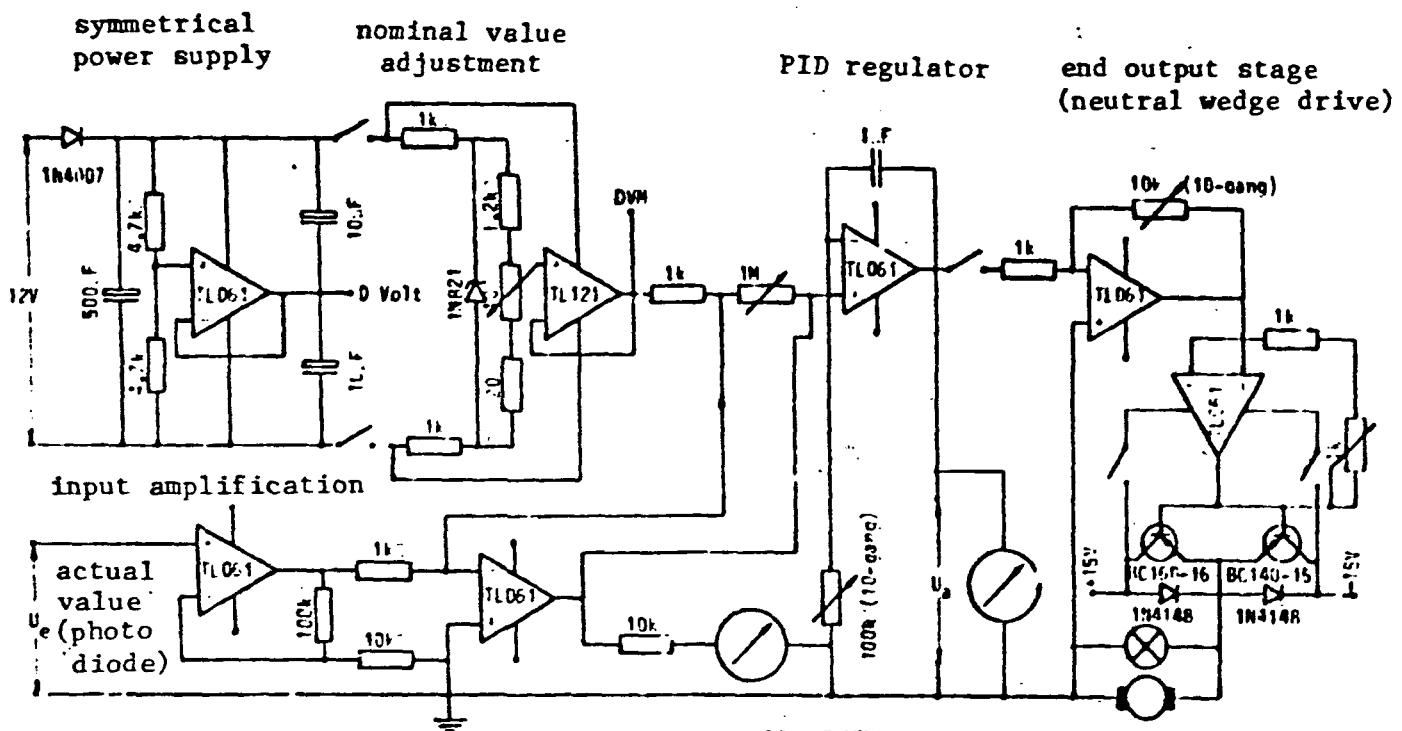
Figure 39 PID Laser intensity regulation

avoid slippage during pole reversal), there is located a
continuous neutral wedge. This optical component - which acts
as a linear filter - is placed in the beam path, between the
laser exit and the prism mentioned above. It thereby becomes
possible to correct for the smallest intensity variations and
the continuous output decrease (life-tiem dependent). The integral
portion of the regulator limits the long-term weakening to less
than   3%. The differential portion of the control electronics
makes it possible for the regulating circuit to react already at
the beginning of a steep interference flank, before maximum ampli-
tude is attained (leading effect). Large demands are placed on
the proportional part, because of the necessary amplification
factor of approximately 10^5, since circuits of these character-
istics, with amplification factors $>10^3$ tend to be dynamically
unstable. Hence, a multi-stage amplification chain should be
adopted. It is absolutely necessary, in addition, to use

"offset"-balanced operational amplifiers of a model with high
temperature stability specifications. In spite of this very
laborious detail work, in its technological implementation, we
were at first not sully successful in compensating for the very
strong short-term line fluctuations, determined by specific
local conditions (caused by the discontinuous operation of
machines of high power consumption). It thus became necessary
to operate an independent supply line (see Figure 52). It consists /79
of a 24 V, 15 A battery charger, with a 400 Ah fork-lift
accumulator and a 24 V DC/220 V, 50 Hz direct current/alternate
current inverter (200 W output power). A test/loading cycle time
of approximately 1:1 is thereby attained. The nominal block to
block time is approximately 20 h: after at the most this period
of time the laser power supply must be switched back to the
public power network, to recharge the accumulator. Since the
entire laser-optical thrust measurement system is kept under a
light-tight cover to avoid outside light influences, active cool-
ing must be provided to prevent heat accumulation near the laser,
due to the laser's own heat losses. Open water circulation circuits
are adequate for this purpose.
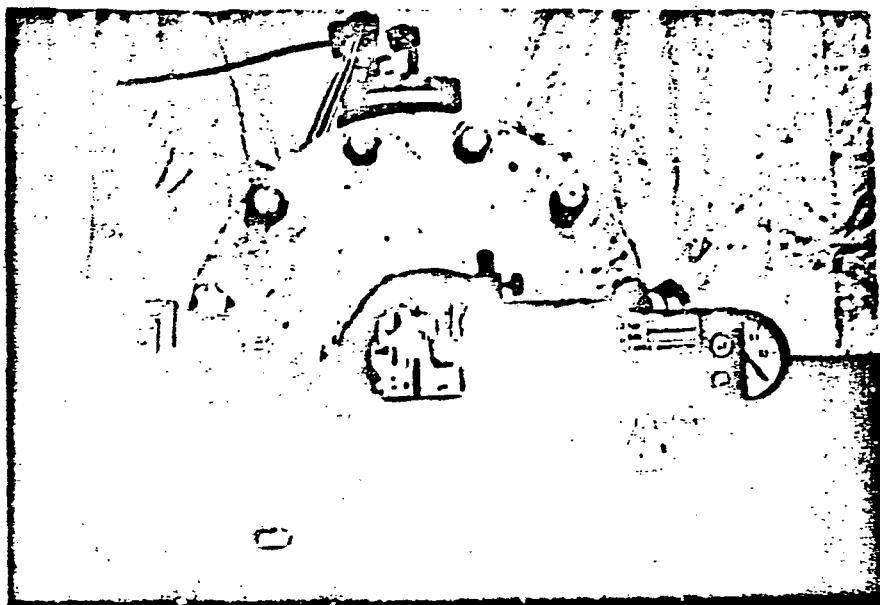
Figure 40   Portion of the thrust measurement system outside of the
vacuum chamber
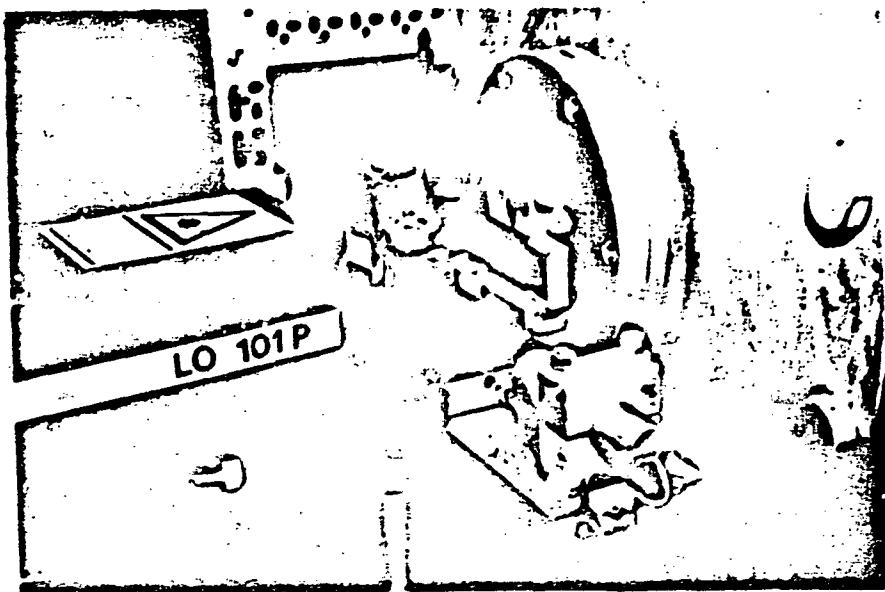
Figure 41 Neutral wedge control (active control member) for laser
intensity stabilization

3.2.2.2 Calibration device for thrust measurements

In order to calibrate the thrust measurement system, first the
environmental pressure p_∞ occurring inside the vacuum chamber
is established, in a preliminary tests, as it is under full
pump suction power and nozzle flow (leak rate) at fixed p_c. Next
the N_2 supply pipeline is interrupted and the p_∞ regulating
circuit is activated (see also 3.2.1). Thereby the environmental
pressure is fixed at the value determined above and the upthrust
influences due to residual gases in the chamber may be considered
compensated. Now the calibration basket (see Figure 43, page 84)
is introduced through the divergent nozzle portion. The basket's
positioning is so designed (double cone, point contact) that
calibration masses placed in the calibration basket can exert
only vertical components in the thrust direction and position of
the nozzle axis. By means of a revolver cassette system, arbitrary
quantities of beads of precisely know mass can be admitted to the
basket. These beads simulate the "calibration thust" for the

$V_{mess}^{(1)}$ mV
$a_{eich}^{(2)}$ g
f_{mess} mN

etc.

2nd bead in the calibration basket

1st bead in the calibration basket

calibration basket (empty) introduced

unloaded thrust frame

time

1 "mess" = measurement 2 "eich" = calibration
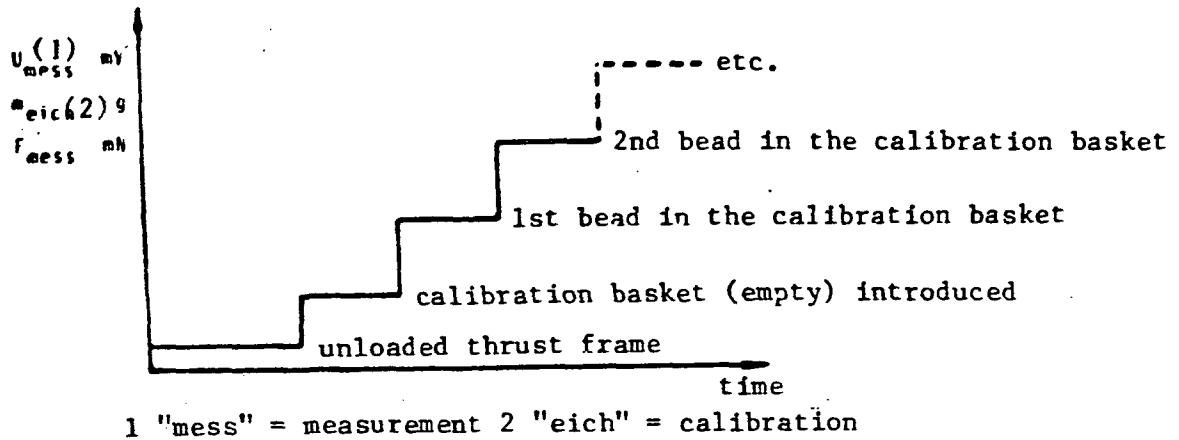
Figure 42 Qualitative course of the thrust calibration

(/82)
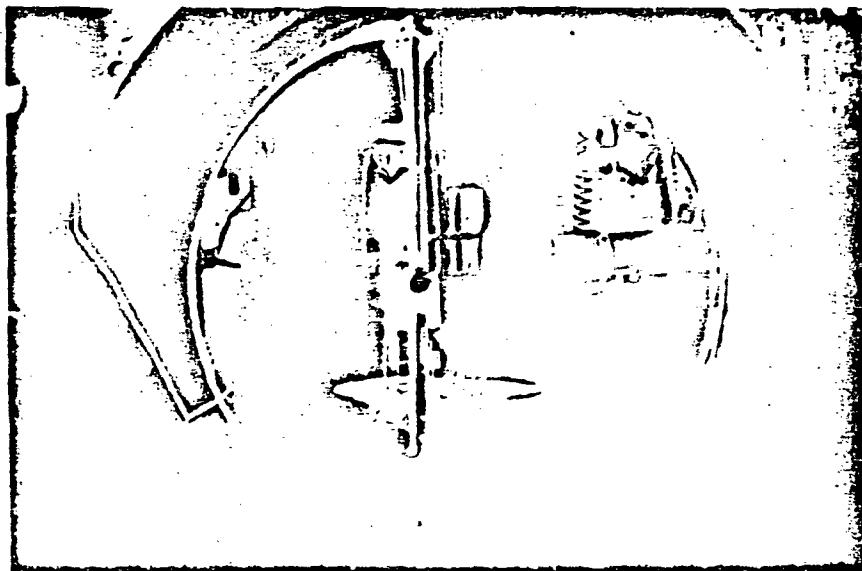
Figure 43 Propulsion unit suspension with flanged combustion chamber
pressure determination and calibration device of the thrust
measurement system

thrust measurement system. The response of the measurement system
is shown in Figure 42, above, for the individual beads falling
into the basket (Mass: typically 3 g).

84

From the step function obtained during the calibration phase
it is now possible to determine the gradient of the function
$F = f(U_{meas,thrust})$. Once the calibration measurement is com-
pleted, the calibration basket including its position cone is
removed from the propulsion unit by means of automatic controls,
so that that the precision performance measurements can be
performed immediately following. Unavoidable zero-drift in the
instruments is thereby prevented from exerting undue influence
on the precision of the measurements. For additional control,
the calibration was repeated after each measurement series.

3.2.3 Mass throughput determination

The mass throughput $\dot{m}$ is the most important limiting quantity
- next to the thrust - in the experimental determination of a
rocket propulsion unit's specific performance I_{sp}.

A large number of physical principles - which in turn can be
expressed technologically in an enormous multiplicity of forms -
could be used in its measurement. In the context of this study,
the most significant possibilities were examined either by
preliminary theoretical considerations, by borrowing existing
systems and by extensive preliminary testing. Therefore, the
listing following should be consiered only as an overall review.

3.2.3.1 Comparison of the various alternatives [28,31]

a) Throughput measurements using turbine rotor systems:
   A turbine rotor is fitted into a feed pipe, with its segmented
   axle made alternatingly of conducting and non-conducting
   material. The fluid's motion causes the turbibe to start
   rotating, and in a coil arranged around the axle,an alternating
   current is induced, whose frequency can be assigned to the
   rotation rate and hence, to $\dot{m}$. It can be shown that this equip-
   ment - which functions satisfactorily for liquids (and large
   throughput rates - does no longer operate with the required
   precision in the case of small gas volumes, among other

reasons because of slippage and compressibility problems (see section 3.1). Furthermore, the calibration is possible only if an additional system is used (see point j), below).

b) Pressure difference determination:
The resolution of the Δp measurement range here demanded requires very small slit opening diameters (in the 0.1 mm range) and hence, is strongly dependent on the discharge coefficient ψ, which is a function of combustion chamber pressure (or respectively, of the injection pressure: $p_c + \Delta p_{inj}$).

Taking into account Mertel's work [101] and after some pre- /84 liminary testing, this possibility was not further pursued.

c) Perpendicular pipe with float element:
A vertical glass tube with calibration marks is installed in the N_2 pipeline (flow direction: vertical, upwards), inside which a spherule can move, of a material selected as a function of its specific gravity and the pipe flow's dynamic pressure. Independently of reading problems, this method - often used with liquids - is not satisfactory, due to slippage and environmental effects, for small gas quantities.

d) Filling status measurement using a secondary medium (liquid):
An alternative often used in technology is a liquid column connected to the gas storage container. The pressure remaining in the container can be estimated from the displacement of the liquid level, and hence, the quantity of gas used. Based on the required specification, the thermodynamic conditions (T-P problem) proved to be badly reproducible. An electronic indication of liquid level is additionally impeded by the lack of adequate liquids (conducting, or optically evaluated, etc.).

e) Measurement of the pressure increase upon discharge into a

large container:

The possibility of determining $\dot{m}$ by recording the course of
the pressure in a large chamber of known volume, as a func-
tion of the valve setting of the rate of flow, had to be
discarded, after intensive preliminary testing. This was due
to the fact that because of the necessary valve opening times
Joule-Thomson effects and environmental temperature influences
could no longer be neglected.

f) Direct optical measurement of the velocity of flow: /85
   This alternative also had to be ruled out, because the density
   differences in the N_2 working medium were not sufficient to
   render clearly visible changes in the flow velocities within
   the pipe. The admixture of particles that would positively
   change this characteristic had to be excluded because of the
   gas purity requirements.

g) Direct inductive or capacitive measurement of the quantity
   discharged:
   Preliminary work was performed also on this concept, in con-
   nection with variation d), above. This alternative also had
   to be abandoned because of purity requirements (see also f))

h) Heated wire probes:
   After intensive collaboration with suppliers of such systems
   the integral measurements of the flow velocity and of the
   medium's density (repurified N_2) by heated wire anemometer
   procedures proved to be insufficiently precise for the small
   tube diameters here used (Ø typicallv 2 mm), as well as non-
   reproducible, because of capillary action and the influence
   of the probes on the flow itself.

i) Laser Doppler velocity meter:
   Eventually, this laser-optical method, given appropriate
   development efforts on the systems available today, will permit
   direct measurements of the flow profile in narrow tubes and of

the nozzle discharge velocity distribution. Since currently the obtainable precision is still insufficient, the application of this method had to be disallowed, in the context of this study.

j) Weighing system:
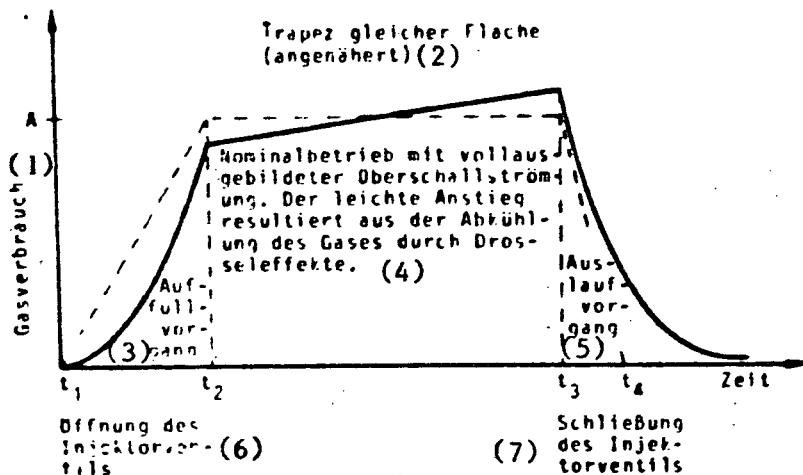
KEY 1 Gas consumption 2 Trapeze of equal surface area (approximated) 3 Filling process 4 Nominal operation at fully formed ultrasound flow. The slight increase is due to gas cooling by the throttling effect 5 Emptying process 6 Opening the injector valve 7 Closing the injector valve

Figure 44   Typical mass throughput course (time scale distorted)

All methods described would require additional calibration methods in the event of their application, ultimately based on gravimetric methods. Hence the idea arises of using such methods directly, without the intermediate steps described above. These gravimetric methods can be divided into two main groups:

- Continuous weighing → $\dot{m} = f(t)$
- Integral weighing (before and after the flow process) →

$$\int_{vor}^{nach} \dot{m}\, dt)$$

"nach" = after
"vor" = before

88

The tendency shown in Figure 44 (page 88) is decisive for the latter of these versions.

The approximation of the N_2 throughput is usually performed   /87
by application of the trapeze equation [68]

$$\int_{t_1}^{t_4} \dot{m}\, dt = A \cdot \left[\frac{(t_4 - t_1) + (t_3 - t_2)}{2} \right] = m_{vor} - m_{nach} \to \qquad (105)$$

$$A \,\hat{=}\, \overline{\dot{m}} = \frac{(m_{vor} - m_{nach}) \cdot 2}{(t_4 - t_1) + (t_3 - t_2)} \qquad (106)$$

On the one hand, the trapeze method would be sufficiently precise (i.e., the filling and emptying processes could be neglected) if the increase in $\dot{m}$ due to the throttle effect at very large differences $(t_3 - t_2)$ did not occur. On the other hand, however, it is precisely for large values of $(t_3 - t_2)$ that the throttle effect has an increasingly interfering effect, which forces keeping test times in the direction of smaller Δt values; because of the non-stationary gas consumption during switching on and off, this, in turn, worsens the precision.

In case of continuous weighings of the N_2 consumption, these effects are of subordinate importance, since one can wait for stationary conditions before taking several $\dot{m}$-values. This also makes it possible to evaluate drifts (caused by gas cooling) quantitatively.

89

3.2.3.2 Selected weighing system - PC 4400

The main problem of this measurement method is ultimately the required resolution per weighing (better than 0.01 g), with the simultaneous utilization of a relatively heavy storage container (approximately 7.5 kg). The balance eventually decided on (Mettler, Zurich; PC 4400), with a resolution of 0.001 g and /88 a measurement range to 4.4 kg, is by far the best instrument on the market, for its range. Since no systems exists with c comparably high resolution beyond the measurement range of 4.4 kg, the $\dot{m}$-measurement problem becomes therfore displaced to the precompensation of the remaining 3.1 kg of the storage container (including the reduction station and the gas supply), which can not be balanced by design changes. Safety regulations, the test times required and the mechanical design overall do not allow for a container with a total mass substantially below 7.5 kg. In the required prebalancing, a decisive advantage of the basic balancing principle of the PC 4400 chosen, finds its expression: the mass to be determined presses on a vertically freely moving cylinder, kept in its position by the action of a strong magnetic field. An optical edge establishes this position to better than 0.0001 mm and provide actual value information to a control circuit, such that it can change the coil current until the magnetic force fully compensates the force due to the weight, and the cylindrical tod again occupies its original (unloaded). This means that the PC 4400 balance weighs without displacement. Hence the coil current is a direct measure of the corresponding mass.

On this basis several prebalancing principles were examined theoretically and experimentally:

- Counterweights with roller or knife-edge bearings
  In the end it was not possible to solve the mechanical bearing problems (close collaboration with the Chair for Precision Instruments, Prof. Unterberger [176]).

90

- Upthrust body

  Immersion of hollow bodies into liquids or upthrust generation
  by means of gas-filled balloons had to be abandoned because
  of problems of reducibility due to environmental influences
  (mainly dependence of characteristic material values on T_∞

- Permanent magnet electromagnets

  These methods also had to be excluded because of their long-
  term behavior (decrease in field intensity) and dependence of
  the magnetic properties on T_∞, following very extensive pre-
  liminary testing (in addition, the balance system was affected
  by the strong compensation fields required.)

- Spring system

  Since as we mentioned above, the PC 4400 weighs without
  displacement, spring compensation is appropriate

$$F_{Feder} = \Delta L \cdot c \qquad \text{("Feder" = spring)} \qquad (107)$$

The first preliminary tests already showed that small changes
in the environmental temperature, near the spring - caused,
for instance, by convection currents - changed the spring
constant so sensitively, that reasonable measurements became
impossible In order to solve this $c = f(T_\infty)$ problem, first a
pendulum construction (see also clock pendulum) was implemented
using three compression and three tension springs, in this case,
made of the same material; its main characteristic is that it
solves the temperature stability problem with respect to the
relief spring [176]. Unfortunately the manufacturing problems
in relation to a symmetrical force introduction in the six
equally long spring proved to be too difficult.

Hence we must forego a mechanical correction of the spring
constant changes due to T_∞. The method chosen for use utilizes
a cylindrical spring with extreme insulation thicknesses

surrounding the spring itself (without touching it!) and around
the entire balance system (see also 3.2.2 and 3.4). In addition,
this compensation spring does not act directly on the block
but on a support thermally insulated from it. This prevents block
shortenings (due to cooling effects of the gas in the reducing
station) from affecting the sprin length and hence, the force   /90
of compensation. The final design is shown in Figure 32 and 47.
In addition, the balance's power supply (energy loss heat) was
provided with water cooling to maintain temperature gradients
(convection) as low as possible.
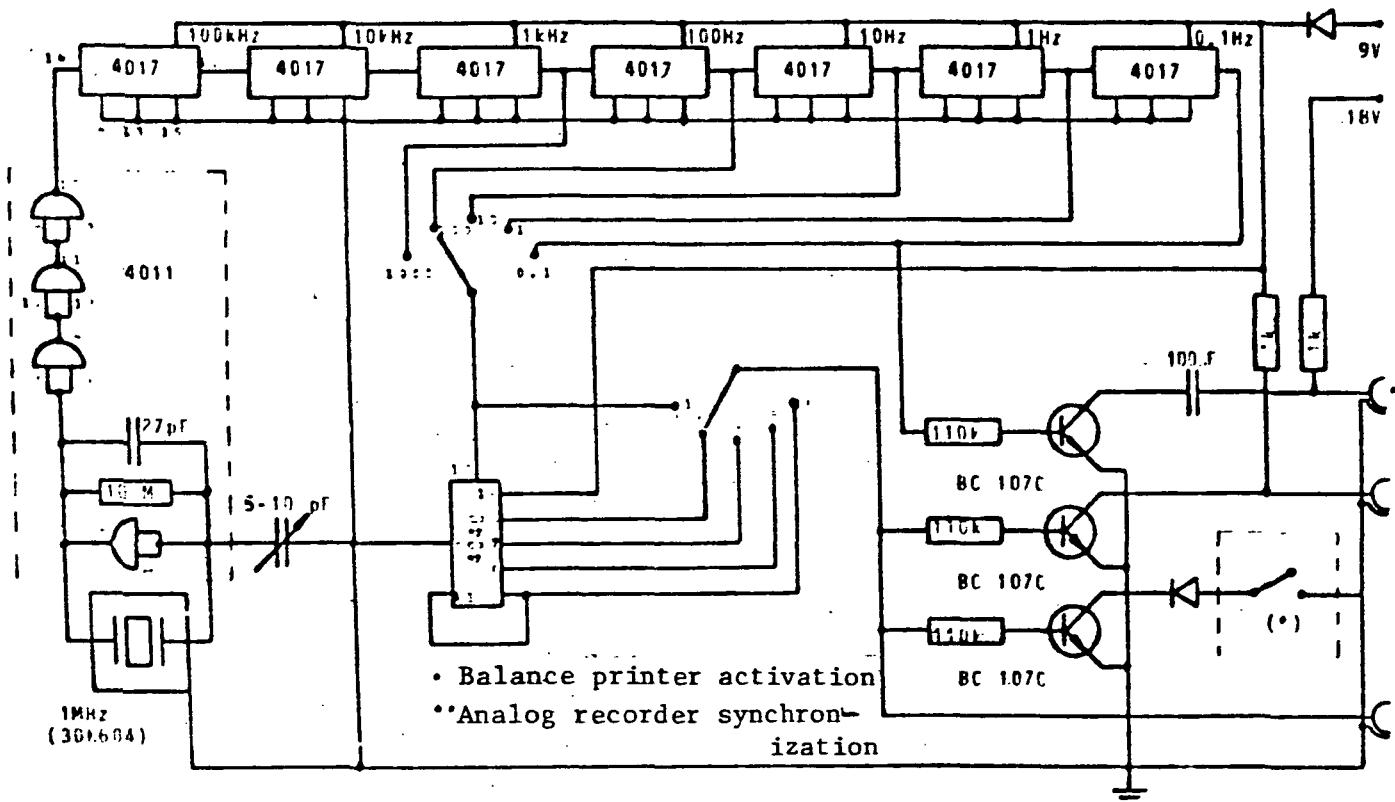
Figure 45   Balance printer control circuit diagram

For a simpler output of the balance's weight indications, these
values are issued by a printer (Mettler GA 40). The printer
system is activated by means of a quartz-stabilized control

designed by us. The circuit diagram for the printer control is shown in Figure 45, above.

3.2.3.3 Injector triggering

Switch S in:
Position 1: 1–15 secs
Position 2: 10–150 secs
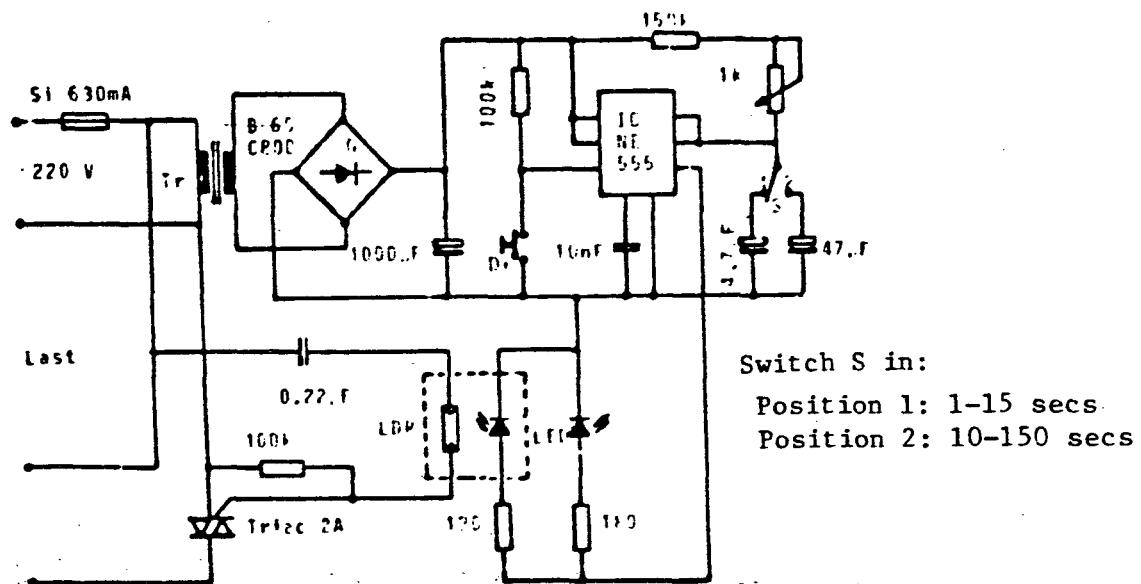
Figure 46   Circuit diagram for the injection time control

The control includes an adjustable time triggering (decadic sub-division, from 10^{-4} to 10 sec and powers from 2^1 to 2^5). This triggering controls not only the printing of the instantaneous balance weight value, but also serves as time synchronization for the remaining measurement value acquisition and processing units (see also section 3.3). In addition, a time switch was developed to allow preselection of the test time and subsequently control the injection valve. In order to avoid feedback between the electromagnetically actuated valve and the electronics, the latter is electrically isolated from the valve's actual control relais by an optic coupler.

When the injector valve is activated, the p_∞ control of the

vacuum chamber is simultaneously switched off and full pumping
power is released (see also section 3.2.2.2). Because of the
very precise test duration control it is also possible to
control the continuous $\dot{m}$-measurement here used by means of
the integral method mentioned above.
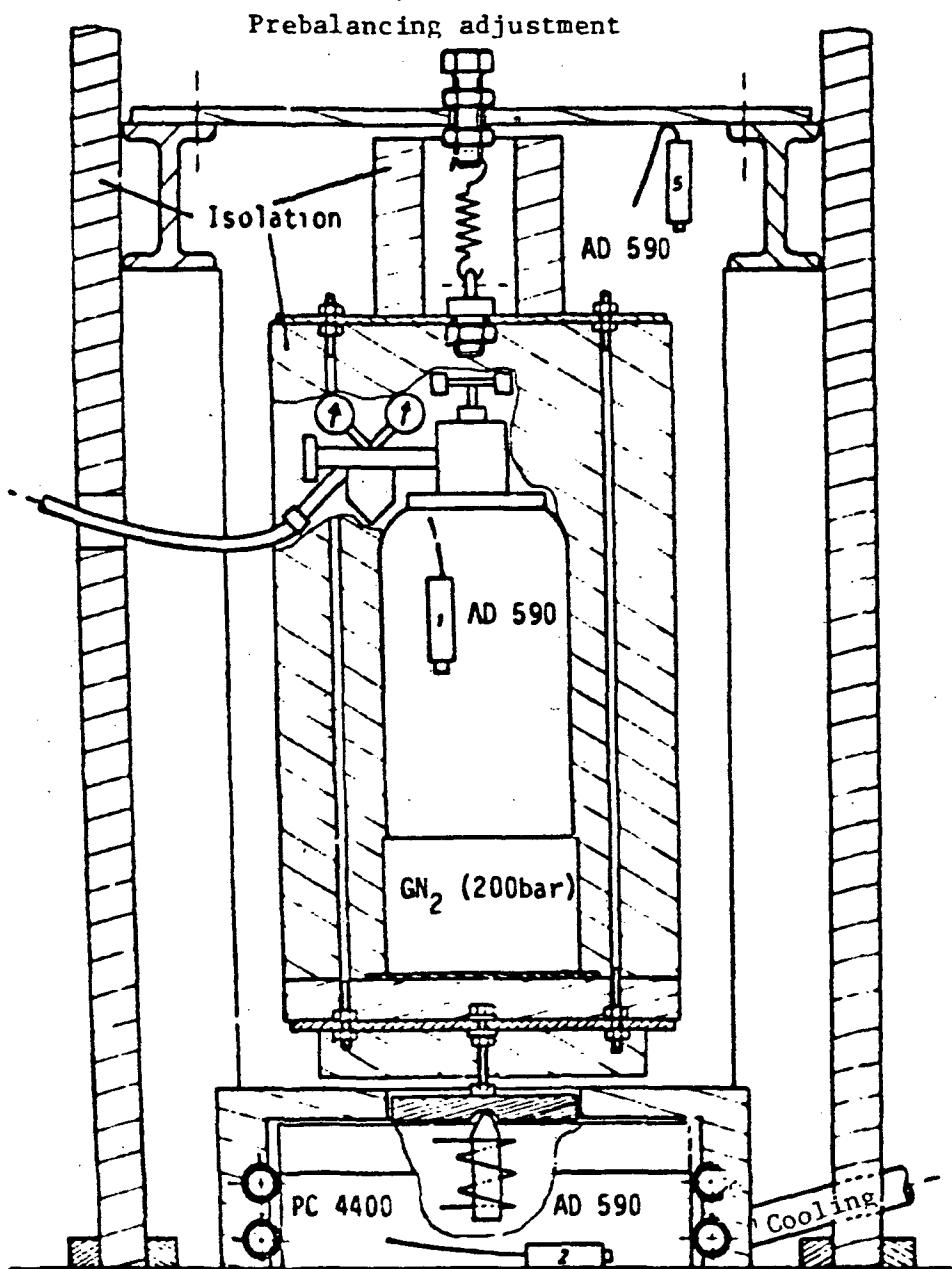
Figure 47   Mechanical assembly for throughput measurements (inside the
balance's environmental chamber

The standardization and calibration of the entir $\dot{m}$ system
was made possible using small steel beads (of known mass),
which rolled into the receiving container, located in the
isolated bottle block frame (see Figure 47, page 94), through
a flexible tubing (i.e., the inverse of the procedure for N_2
discharge in the actual precision measurement test), at pre-
cisely known time intervals. Standardization tests show that
after solving the main T_∞ problems (in relation to the spring
constant c) the $\dot{m}$-measurement construction operates very
satisfactorily.

3.2.4 Combustion chamber pressure determination

In order to determine the combustion chamber pressure, an
HMB-11 (Hottinger-Baldwin Co.) pressure sensor designed fol-
lowing an inductive method is flange-mounted perpendicularly
to the combustion chamber axis. It is connected to the chamber
by a capillary ($\emptyset$ 0.6 mm).

The pressure to be measured acts on a thin membrane, which in
turn hermetically seals off a reference volume at a pressure of
1 bar. If this membrane is deformed due to a counterpressure,
then it pushes a small piston attached to its center into an
induction coil excited by a 100 kHz alternating current. Through
a closed control circuit, the coil current is modified long
enough (see section 3.2.3) – as a function of piston displace-
ment – to return the membrane to its undeformed original posi-
tion. After suitable electronic matching, the coil current
allows a direct statement to be made regarding p_c. In contrast
to many of the customary systems, the advantage of this sensor
is the measuring probe's constant dead volume. The precision
stabilization of the P11 measurement tube supply voltage, the
100 kHz carrier frequency generator, the membrane control cir-
cuit, the measurement value amplification and its matching are
all housed in a fully integrated instrument, the HBM-MC-1A.

In order to minimize interfering pick-up and power influences, the MC-1A electronics, housed in a metal cylinder, is attached directly to the P11 pressure measurement tube. The arrangement can be seen in Figure 43. It is thereby also possible to reduce the number of external incoming leads to five cables: two for the coarsely stabilized 12 V supply, one cable for screening or grounding, respectively and two for the measurement value. Since the pressure measuring device is mechanically connected to the combustion chamber and hence also to the thrust frame, these incoming leads must be fashioned of very thin wire (that is permissible, since only very low electric power is needed) and flexibly suspended. Outside of the test chamber, the measurement value must be amplified further, for a better application to the measurement value acquisition system. An /94 overview of the entire combustion chamber pressure detection system is shown in Figure 48, below, as a circuit diagram. We
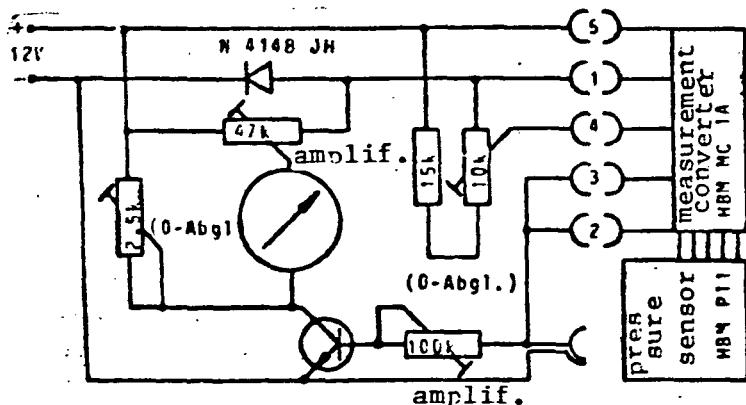
Figure 48   Measurement value amplification and adaptation of the combustion chamber pressure detection system

should remark that the utilization of sensors based on the piezoelectric effect must be avoided, since they are not well suited to stationary pressures (as they occur here, essentially), in comparison to strong, dynamic pressure variations (the problem of long-term drift in charge amplifiers.) Careful calibration

tests have shown suitable agreement with the required speci-
fications: reproducibility better than 0.3% of the measurement
range of 1 to 25 bar absolute pressure.

Due to the precise determination of the combustion chamber
pressure it is possible to determine a 1-dimensional flow rate
coefficient c_D, using a 1-dimensional mass throughput equation:
$\dot{m} = p_c A_t / c^*$, with the aid of the direct $\dot{m}$-measurement method
described in section 3.2.3

$$c_{D,1-d} = \frac{\dot{m}_{Mess,W}}{\frac{p_c A_t}{c^*}} \tag{108}$$

Typical results are shown in Section 4.

3.2.4.1 Determination of the p_c-measurement tube installation /95
        error

Departing from the simplified theory, the gas velocity inside
the combustion chamber is not identically 0, but has a finite
value. Because of this and determined by the technical boundary
conditions due to the connection of a pressure measurement probe
to a propulsion unit, the measured pressure deviates minutely
from the stagnation pressure [12]

$$\frac{p_{c,Mess}}{p_c} = 1 - (\frac{A_t}{A_M})^2 \frac{\gamma}{2} (\frac{2}{\gamma+1})^{\frac{\gamma+1}{\gamma-1}} \cdot f^2 \tag{109}$$

where A_t = throat cross-section,
      A_M = installation cross-section
      $f = \frac{1}{2} (1 + \cos \beta)$
      β = angle between sensor axis and propulsion unit axis
        (here $\beta = 0$)

With the boundary conditions applicable here, the pressure cor-
rection is merely

97

$$P_c = P_{c,Mess} \cdot 1.00000596$$

and can therefore be neglected.

In the course of the test execution it was confirmed that the initial assumption regarding the gas behaving adiabatically within the pipeline system and the combustion chamber, was correct. Because of the high heat capacity of the pipelines, made esssentially of copper, the cooling phenomena in the working medium caused by throttle effects are compensated (provided care is taken not to extend the test duration to several minutes).

3.2.5 Temperature measurements
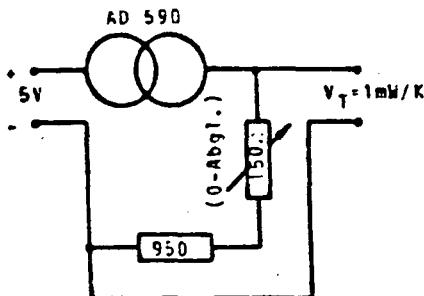
Figure 49   Power supply and measurement value adaptation of the AD 590 temperature sensors

In order to measure the N_2 gas temperature in the N_2 supply lines as well as in the combustion chamber of the cold gas propulsion unit, and at several location of the test installation to control environmental conditions, temperature sensors Model AD 590, of the Analog Devices company, are used. The decisive advantage of these models, in comparison to the customary thermo-elements consists in that both measurement amplifiers and supply voltage stabilizers - as well as a 0 °C reference temperature point - are integrated into the smallest colume (2 x 4 x 0.5 mm). The calibration and spreading followed the very simple circuit shown above.

The sensor proves to have a high resolution (better than 0.01 °C) and an extraordinary long-term stability. The linearity error is less than 0.1% and dislocations due to contact problems, as they occur with thermoelements, have not been observed. Due to the low mass of the temperature-sensitive portion of the "sensor head", the response time (to 99% of the temperature value) is < 1 sec and hence certainly adequate to the application here contemplated.

3.3 Data acquisition and data processing /97

All parameters essential to either measurement or test operation are recorded by high resolution analog recorders, for more rapid optical control (trouble shooting). Measurement variables that do not change during routine operation (such as $T_{\infty,lab}$, $P_{\infty,lab}$, P_{pump}) are rendered visible on meters. The variables necessary for performance determinations of the cold gas propulsion unit are in addition fed to the 10 channel ADC [analog to digital converter] developed at the Chair for Space Technology: it has an associated memory (capacity: 256 words 12 bits long = 4 decimal places). The circuit is shown in Figure 51 (page 101) (see also Roth, A. [127] and Neuwald, W. [111]). Following each measurement, the 10 data channels are printed out (including mean values) by means of a line printer. Through the use of modern microprocessors, the discretization errors of the ADC are at a level below 0.1%, which can be disregarded.

The block diagram below (page 100) provides an overview of data determination and output

KEY to Figure 50 (page 100)   1 combustion chamber pressure   2 Measurement tube   3 Carrier frequency amplifier   4 Amplifier   5 Tracing   6 Relay   7 laser beam control   8 Motor drive   9 internal stabilization   10 Intensity control 11 regulated laser   12 Thrust measurement   13 Measurement signal processing 14 Active band filter   15 Low pass, active/passive   16 Thrust   17 Vacuum chamber pressure measurement and control   18 PID regulator 19 Vacuum chamber pressure   20 Magnetic valve   21 Needle valve   22 Vacuum pump suction line

Brennkammerdruck (1) → Meßröhre HBM F11 (2) → Trägerfrequenz-Verstärker (3) → Verstärker (4) → Aufzeichnung Brennkammerdruck (5) (1)

Laserstrahl-Regelung (7) → Motorantrieb (8) → Laser → Interne Stabilisierung (9) → Intensitäts-Regler (10) → Aufzeichnung geregelter Laser (5) (11)
→ Aufzeichnung Motorspannung

Schub-Messung (12) → Array-Diode PIN-LSC-5D → Meßsignalverarbeitung Icsiccn (13) → aktives Bandfilter (14) → Tiefpaß aktiv/passiv (15) → Aufzeichnung Schub (16)

Vakuumkammer-Druckmessung u.-Regelung (17) → Thermovac TR 201 LH → Combitron(0 - 10V $\hat{=}$ 0-760Torr) → PID-Regler (18) → Relais (6) → Magnetventil (20) → Aufzeichnung Vakuumkammer-Druck (19) / Feinregulierventil (21) / Vakuumpumpen-Ansaugleitung (22)

Massendurchsatz-Messung (23) → Waage(induktiv Mettler PC4400 (24) → Digitalisierung Mettler GA 40 (25) → Drucker (26) → Auswertung (27)
Timer → Drucker (26)

Temperatur-Messung (Element 1 - c) (28) → Sensor → Verstärkung (4) → Kalibrier-Einheit (29) → Aufzeichnung Temperatur (30)

Versuchsdauer-Steuerung (31) → Timer(variabel) → zur Kaltgasdüse (32) → Reduzier-station (33)

Meßwerterfassung (34) → 10-Kanal A/D-Wandler (35) → Steuereinheit (37) → Speicher (38) → Rechenwerk (Mittelwerte) (39) → Auswertung (27)
→ analoge Kontrolle (36)

Figure 50   Block diagram of the data acquisition and processing method

23 Mass throughput measurement 24 Balance (inductive) 25 Digitalization
26 Printer 27 Evaluation 28 Temperature measurement 29 Calibration unit
30 Temperature 31 Test duration control 32 to cold gas nozzle 33 Reducing
station 34 Measurement value acquisition 35 10-channel ADC 36 Analog
control 37 Control unit 38 Memory 39 Computer (mean values)
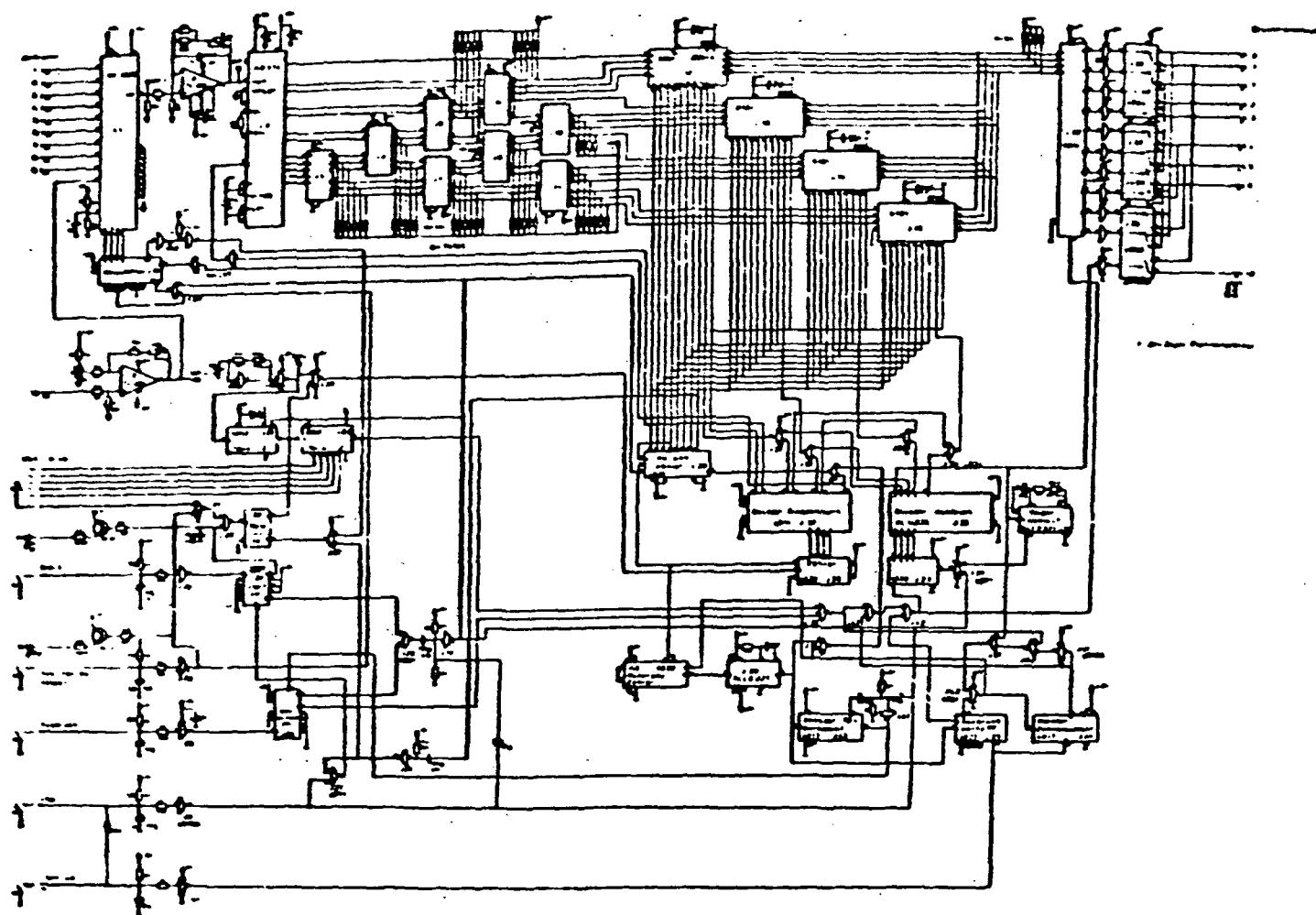
Figure 51 Block circuit diagram of the ADC and memory [27]

A problem always to be solved anew in vacuum technology is that
of electrical lead-ins through a vacuum chamber's walls. For the
task here posed, 10 measurement channels and 15 supply lines
(two of which carry 220 V AC) must be introduced into the chamber
and remain isnulated from each other. Taking the cost problem
into account, we opted for a newly developed 25-pole arrangement
(manufacturing price: approximately DM 10.00). The savings per
channel (in comparison to the customary 1-channel lead-ins such
as those of the Leybold Heraeus company) is approximately
DM 1,400.00

3.4 Additional devices to reduce negative local influences /100

The strong short-term variations in the laboratory line voltage
(caused by the non-stationary power consumption of large external
test facilities) force the utilization of the autonomous source
of alternating power already described in section 3.2.2.1 (see
Figure 52). In order to reduce the temperature effects, espe-
cially on the thrust and mass throughput measurements, the test
arrangement is thermally isolated from the environment. To this
end, a compelte "house" made from 10 cm thick styrofoam blocks,
was built around the vacuum chamber and the laser device. In
addition, temperature variations within the laboratory were
reduced by insultaing the face of the windows and switching off
the air conditioning unit, which operated much too irregularly.

During "test-free" periods the "house", including all working
openings, is kept open, thus reducing to a minimum the tempera-
ture difference between the "house content" and the laboratory.
Priot to the start of the test, the nozzle to be studied is
built into the vacuum chamber and subsequently the thrust measure-
ment chamber and the "house" are closed. The strongly insulating
effect of the styrofoam insures that the effect of any small
temperature differences between the vacuum chamber and the
laboratory, during the test phase, can be ignored. In addition,

this covering performs the functions of a wind screen, something absolutely essential because of the resolution required of the thrust measuring device.

battery charger Philips: PE 1235 30V,11A	peak-stabilized accumulator 24V,400Ah,Deta (12 Zellen a'2V)	AC/DC converter Sadowski: U 114 ~220V,50Hz,250VA	Laser Laser-Optronic: LO - 101 P

~220V,50Hz   1mW
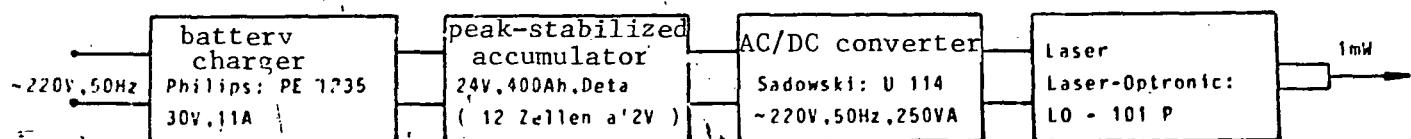
Figure 52   Independent 220 V AC power supply
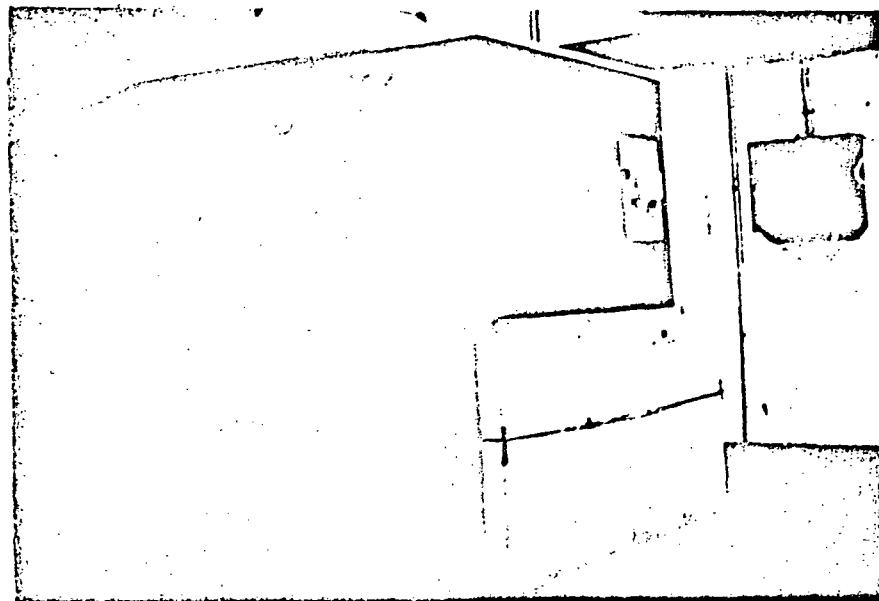
Figure 53   Environmental chamber

Influences due to stationary mechanical floor vibrations - such as those caused by a rotary sliding vane vacuum pump, for instance - can be canceled by using appropriately chosen mechanical dampers. Spontaneous strong disturbances such as those from traffic on the street, however, make it advantageous to perform any precision measurements during the night hours.

The measurements of the effect of ε on the development of the boundary layer losses require the divergent nozzle length to be changed, without affecting the remaining dimensions, especially in the throat area. The initially examined way of building the nozzle in slices, using thing thin foils of linearly increasing bore diameter. was impractical in its realization, since a multiplicity of very thin foild would have to be used, to avoid edge effects. In addition, accurate centering was not sufficiently possible. The alternative of boring the nozzle using precision drills or form cutters was closely examined and then discarded, following discussion with the appropriate companies. Neither the small bore dimensions nor the defined transition geometry in the nozzle throat area (backtaper) can be achieved in this manner.Arc erosive methods were also ruled out. While the craters produced thereby could subsequently be smoothed by grinding and polishing, satisfactory backtapering can not be obtained in this case, either.

The galvanoplastic manufacturing method finally chosen uses a common core, fashioned in one piece, for both the convergent and the divergent portions of the nozzle. This core is machined "flying" on a small, precision turning machine (by a method for which a patent is currently being sought). Figure 54 shows the main characteristics of this manufacturing step.

The forming blades here used were sharpened by scanning a strongly enlarged former plate, which in turn was fashioned using a profile projector. (The manufacture was kindly undertaken by the Wendel Co. of Eichenau, near Munich.)

Only the flying processing insures that the core does not break /104 at the narrowest cross-section (A_t) - the narrowest value attained was 0.23 mm - since backrest clamping and secondary drive methods were eliminated due to exxcessively large misalignment).

Forming blade

Original stock   (subsequently)
Nozzle outlet

Advance
direction

z

Detail z of the blade geometry

R1

R2
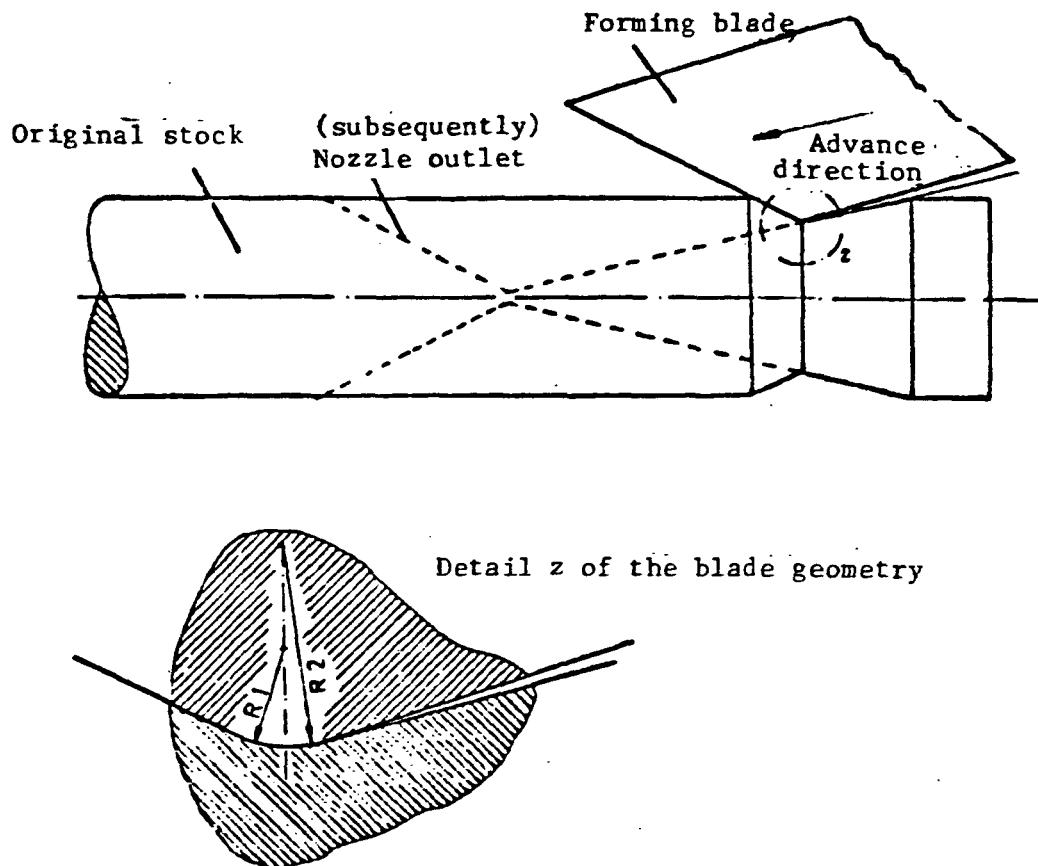
Figure 54 Schematic of the nozzle core's manufacture

Following manufacture of the core, a 3 mm wall thickness is electrodeposited from a copper electrolyte bath. After removal from the plating bath, the external contour of the propulsion unit is fashioned in copper and subsequently the core is removed by gently twisting and carefully pulling apart at both ends. In order to make possible the simple mounting and demounting of the propulsion unit, each copper nozzle is fitted into an installation flange and welded to it (for tightness). The individual steps in the nozzle manufacture are illustrated in Figure 55, page 106. Once a measurement series is completed, for a certain
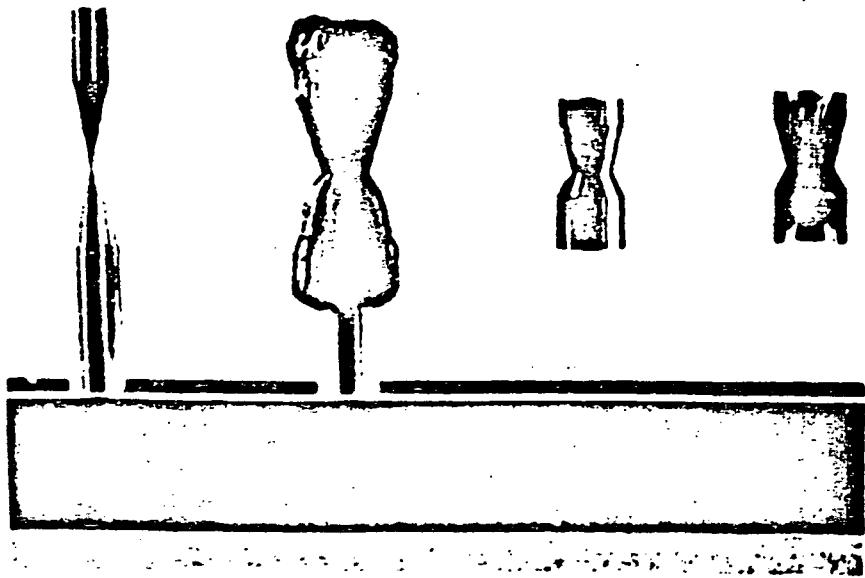
Figure 55 Nozzle manufacturing steps (model embedded in casting resin)

surface ratio ϵ, the propulsion unit is converted - with the aid of a specially made holding device - to the next length or ϵ step, by machining.

Table 4 (page 107) lists the main dimensions of the 12 propulsion units examined.
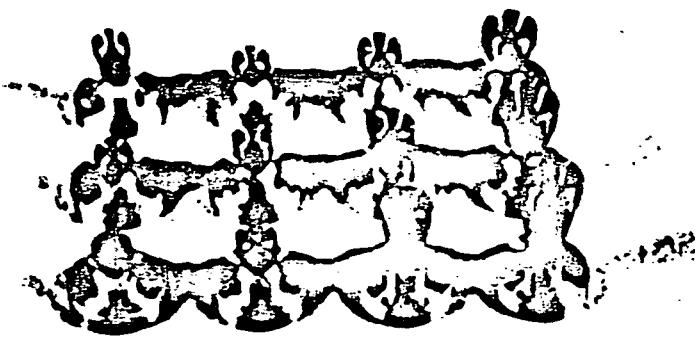
Figure 56 Original view of the 12 propulsion units examined
(prior to first machining)

106

TABLE 4   MAIN GEOMETRIC DIMENSIONS OF THE 12 NOZZLES EXAMINED (NOZZLE NO. 1 WAS DAMAGED JUST PRIOR TO COMPLETING ITS MANUFACTURE)

Nozzle Nr.:	R_T (mm)	Bk_L (mm)	Bk_R (mm)	α_e (°)	D_{200} (mm)	l_{200} (mm)	ϵ_{200} (-)	D_{100} (mm)	l_{100} (mm)	ϵ_{100} (-)	D_{50} (mm)	l_{50} (mm)	ϵ_{50} (-)	D_{25} (mm)	l_{25} (mm)	ϵ_{25} (-)	D_{10} (mm)	l_{10} (mm)	ϵ_{10} (-)
2	0,142	5,0	2,0	15,0	3,89	15,19	187,89	2,84	13,22	99,65	1,93	11,47	46,31	1,41	10,48	24,59	0,85	9,48	8,96
3	0,138	5,0	2,0	20,0	3,87	13,67	196,96	2,80	12,14	102,73	1,96	10,96	50,34	1,37	10,15	24,81	0,97	9,44	12,54
4	0,153	3,663	2,0	10,0	4,28	20,78	195,66	3,09	17,31	101,64	2,17	14,68	50,54	1,51	12,84	24,53	0,93	11,20	9,30
5	0,176	5,0	2,0	15,0	4,92	17,08	194,06	3,55	14,48	100,71	2,54	12,54	51,88	1,78	11,09	25,49	1,11	9,84	9,95
6	0,166	5,0	2,0	15,0	4,68	16,59	198,07	3,33	14,05	100,00	2,39	12,22	51,68	1,66	10,84	25,03	1,03	9,71	9,68
7	0,165	5,0	2,0	20,0	4,59	14,62	192,39	3,31	12,85	99,85	2,40	11,51	52,89	1,68	10,49	25,72	1,00	9,61	9,18
8	0,206	3,443	2,0	10,0	5,79	25,41	196,58	4,13	20,70	99,88	2,93	17,26	50,58	2,07	14,78	25,21	1,29	12,62	9,82
9	0.215	5,0	2,0	15,0	5,87	18,70	186,36	4,31	15,77	100,47	3,07	13,38	51,11	2,16	11,61	25,30	1,34	10,12	9,73
10	0,223	5,0	2,0	20,0	6,18	16,45	191,75	4,47	14,11	100,00	3,21	12,30	51,73	2,25	10,96	25,36	1,38	9,79	9,56
11	0,306	3,092	2,0	10,0	8,42	30,94	188,51	6,09	24,43	98,54	4,41	19,45	51,72	3,08	15,64	25,22	1,72	11,85	7,93
12	0,322	5,0	2,0	15,0	9,12	24,40	200,15	6,51	14,92	101,87	4,59	15,77	50,66	3,22	13,23	24,95	2,02	11,03	9,86
13	0,324	5,0	2,0	20,0	9,03	20,24	194,28	6,53	16,72	101,47	4,59	14,03	50,29	3,25	12,17	25,13	2,00	10,51	9,57

Microscopic examinations of the nozzle throat area before and
after the test series showed that there was no substantial wear
and hence, change in geometrical dimesnions. The evaluation was
based on images from the MPI* Heidelberg electron microscope,
provided by graduate engineer Peter Lell. Figure 57 shows the
throat area, while Figure 58 represents a strongly magnified
portion of the nozzle's external contour.
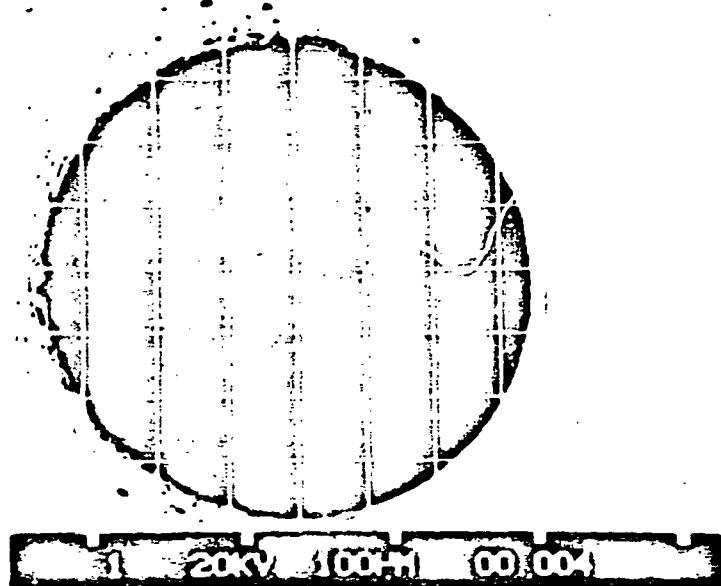
Figure 57 Scanning electron
microscope image of the throat
area (Magnification, X 200)
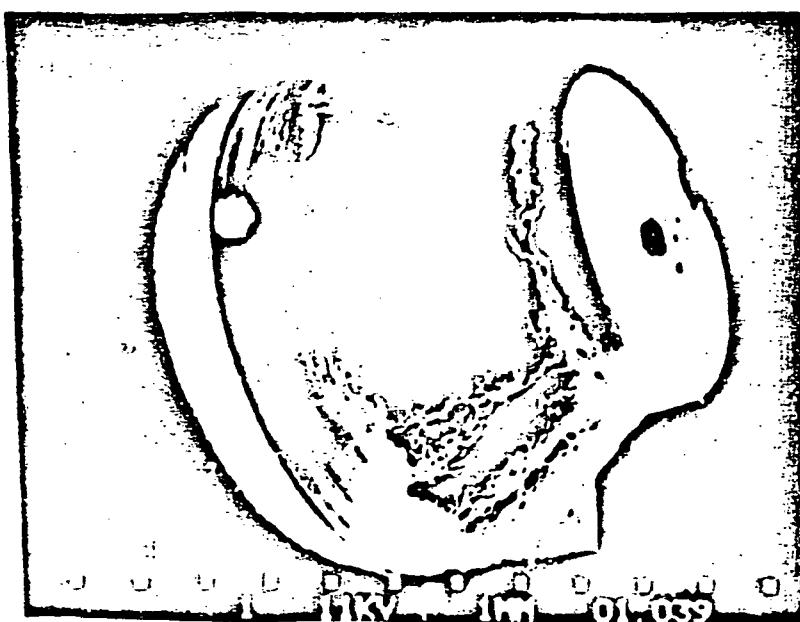
Figure 58 Partial
view of the external
contour

* No expansion provided in the foreign original
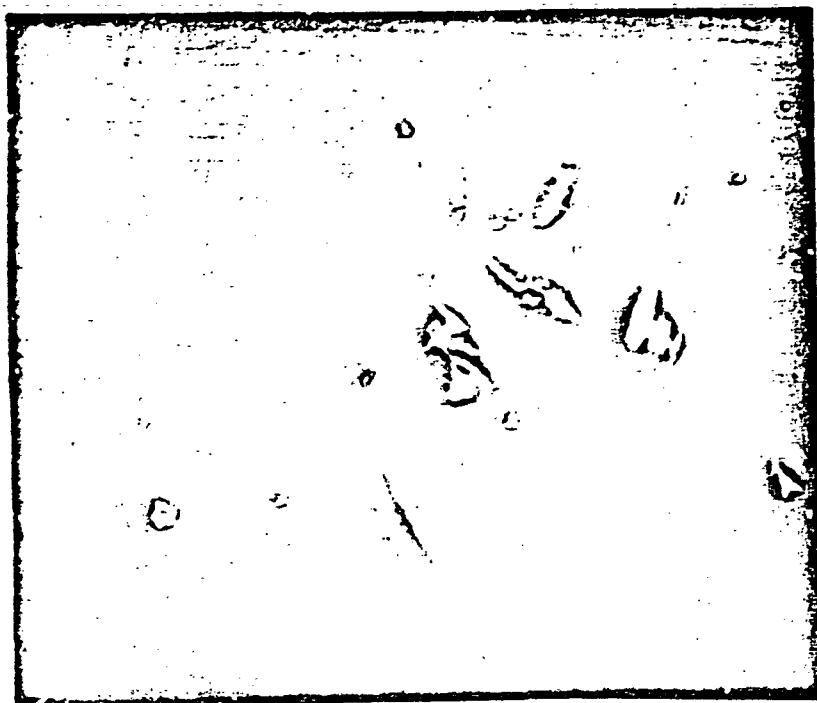
Figure 59 View of a complete propulsion unit
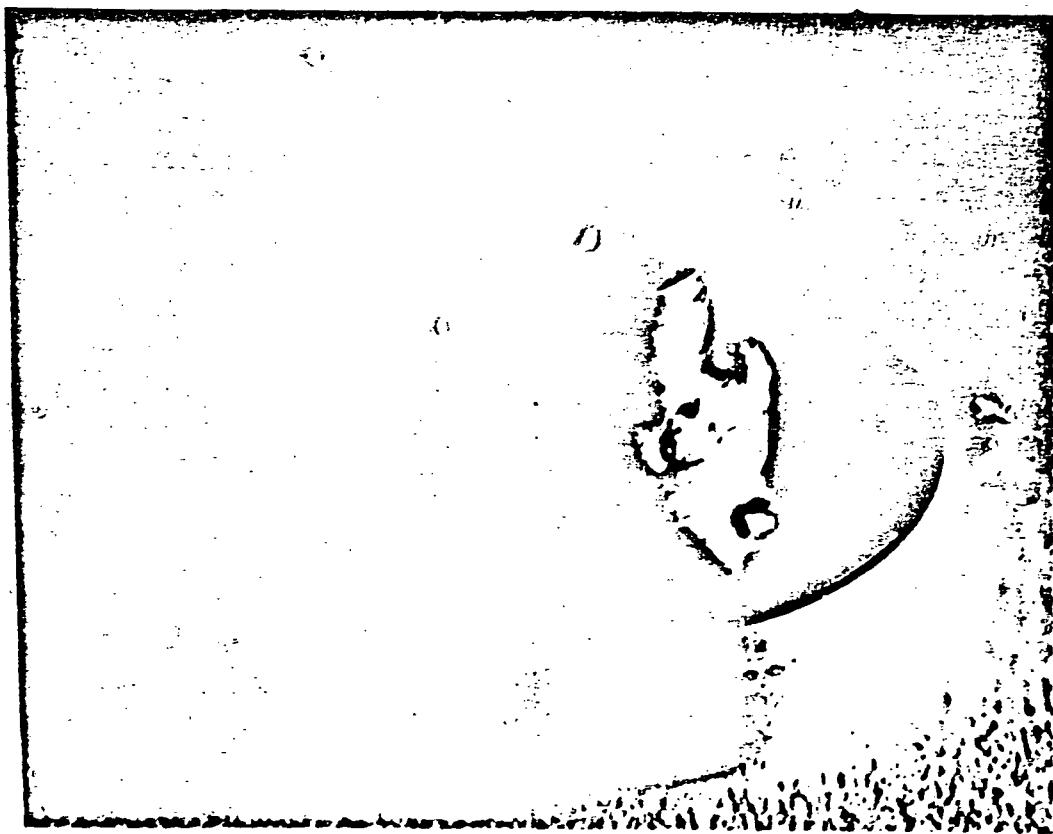
Figure 60 View of the complete propulsion unit

4.1   Review of the test extension

The twelve cold gas propulsion units were measured in five test
series.After each of these series the nozzle's end cross-section
was reduced by mechanical means (ε-steps: 200, 100, 50, 25, 10)
and measured by microscopy. Within a given test series, five
combustion chamber pressures were applied four times each,[*] for
a total of 1200 individual tests. Few of the interferences with
the measurement arrangement during a given test - caused mostly
by eccentri loading of the $\dot{m}$-balance of the N_2-bottle frame -
could be eliminated to complete the test. The installation of a
sufficient number and size of readily accessible work openings
proved to be extraordinarily positive (see section 3.4). Due
credit must be given the T_∞ stabilization, in this sense. Any
subsequent experimental efforts should include the following
improvements, to increase precision and facilitate test execution:

- fully airconditioned test space
- separate data acquisition room
- supply systems (mains operated power supply) outside of
  the test chamber
- more stable building construction
- low-traffic external environment

See also section 3.4, in this regard.

For a more ready control and handling of the large quantity of
measurement values, in the subsequent calculations, we used
the following nomenclature:

---

[*] 20, 15, 10, 5, and 2 bar

Nozzle number   Combustion chamber pressure (coarse adjustment)   ε-step   Sequential test number, for a given nozzle, at the same pressure and at constant ε

Example :   5.10   0   1

2	02	0 = 200	1
3	05	1 = 100	2
4	10	2 = 50	3
5	15	3 = 25	4
6	20	4 = 10	:
.			
:			
13			
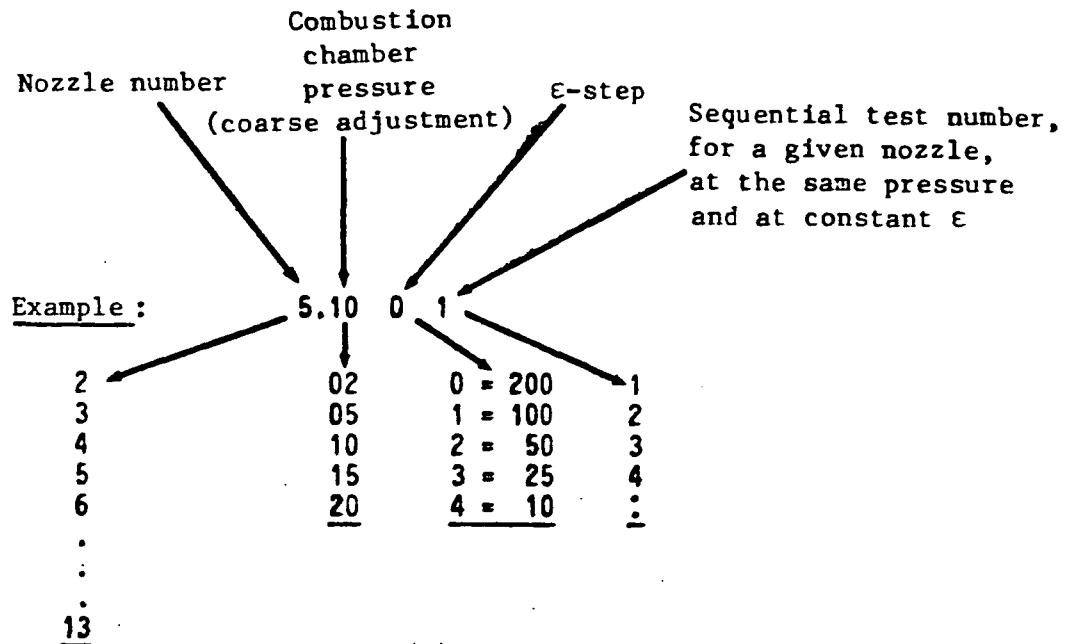
4.2 Evaluation of measurement results by means of typical examples

The output from the measurement acquisition system arranges all experimental data according to the test number described above and makes them available to an evaluation program. Figure 78 (see section 9.2) shows an input listing for such a test run. Here all measurement variables are examine for their order of magnitude and units, and corrected (for instance, the thrust measurement value is corrected for the Bourdon effect; the p_c value for $p_{\infty, vac\ chmbr}$). Next, especially tailored to the corresponding test number, the theoretical performance prediction EGVP is started, such that in the end a data package arranged in parallel has been generated, with the theoretical and experimental performance parameters. In order to render the quantity of data thus created more tractable - by means of an interactive (i.e., terminal controlled) graphics program -
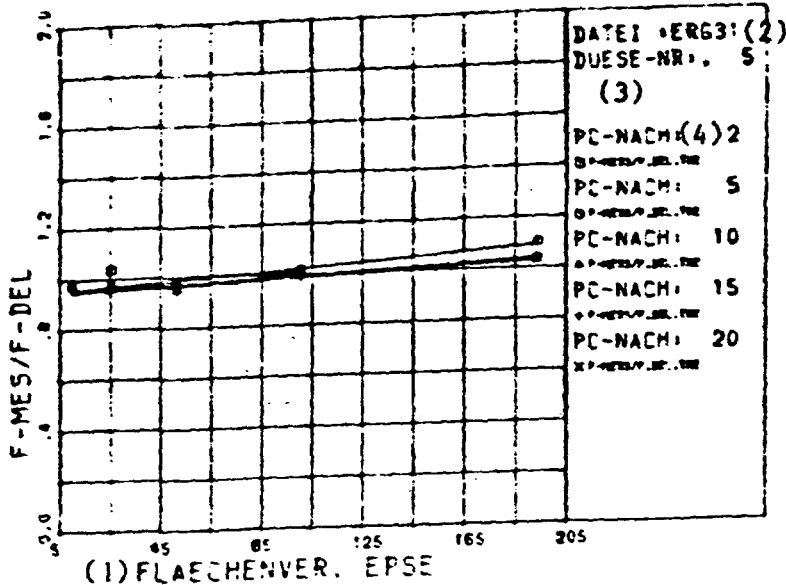
111

Figure 61 Ratio of measured to predicted thrust, plotted as a function of ϵ, with p_c as parameter
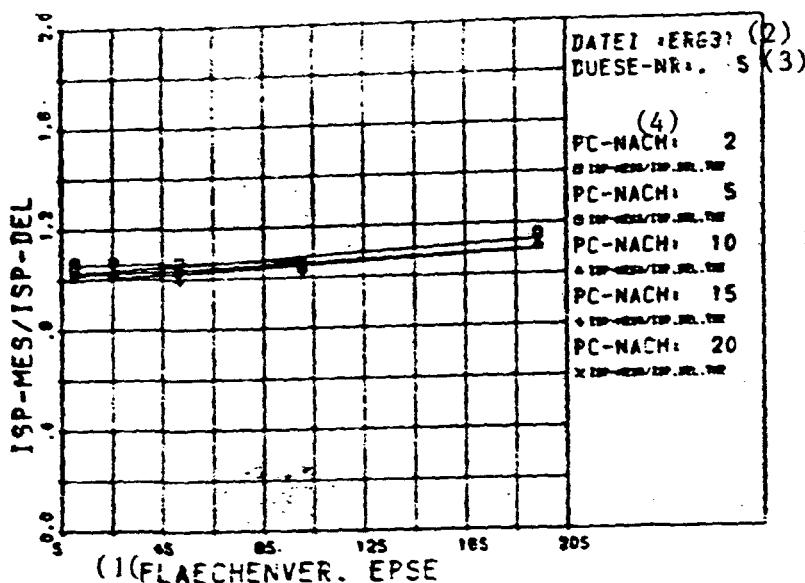
Figure 63 Ratio of measured to predicted impulse, plotted as a function of ϵ, with p_c as parameter

KEY   1 Surface ratio ϵ 2 Data package: result 31   3 Nozzle No. 4 from

the data are plotted. Not only can the scale of resolution be arbitrarily changed, but it is also possible to perform changes in the equalization curve, with respect to individual measurement points. Each of the 40 values per test run can be chosen to be x, y or a parameter point. Due to the interactive input
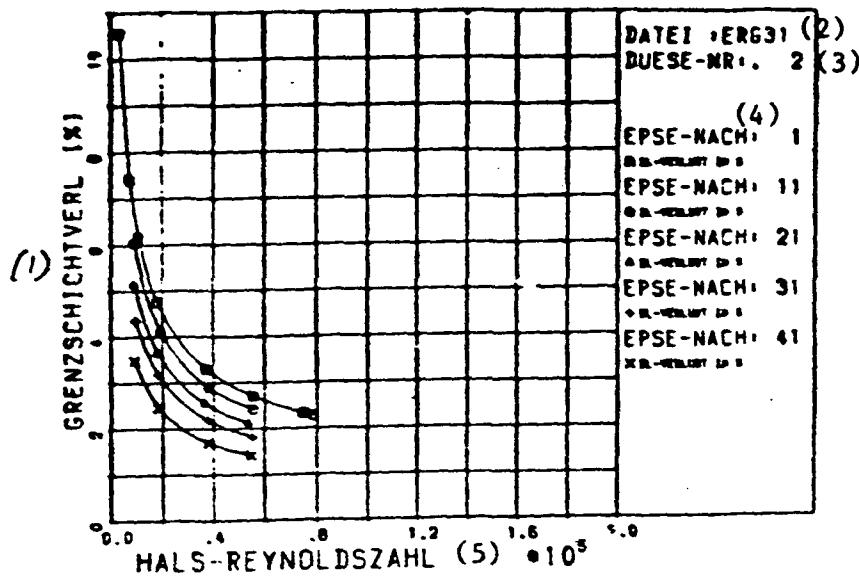
Figure 62 Boundary layer loss
as a function of the throat-
Reynolds number, with ε as
parameter
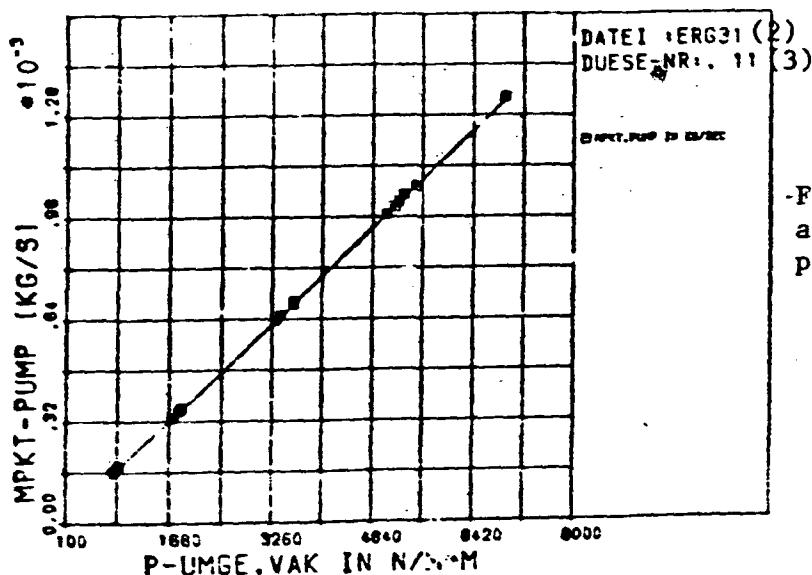
Figure 64 Pump throughput as
a function of the environmental
pressure in the vacuum chamber

KEY   1 Boundary layer loss   2 Data package: result 31   3 Nozzle No. 4 from
5 Throat Reynolds number

from the graphics terminal, previous verification of the results
can help in decisively reducing paper waste due erroneous output.

Figure 65 Mass throughput as a function of p_c with ε as parameter

Figure 66 Measured over predicted mass throuput, with p_c as parameter
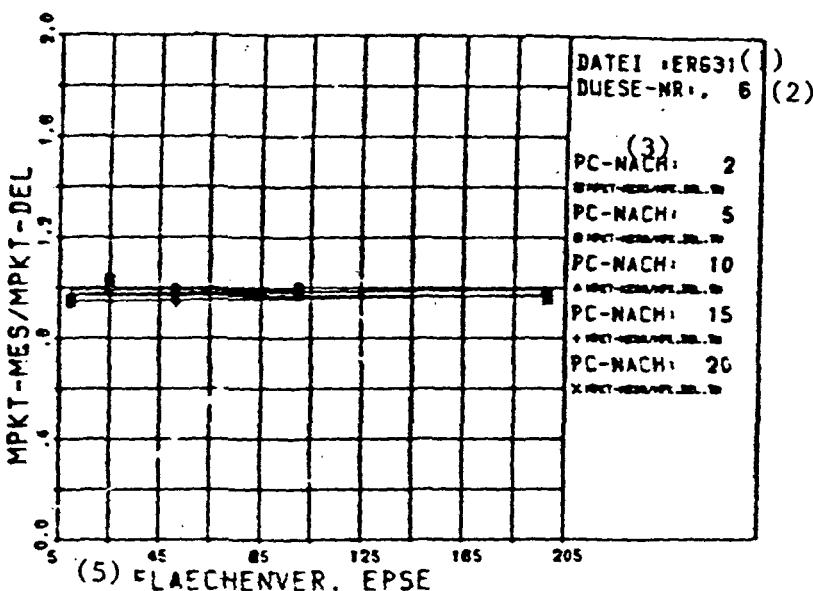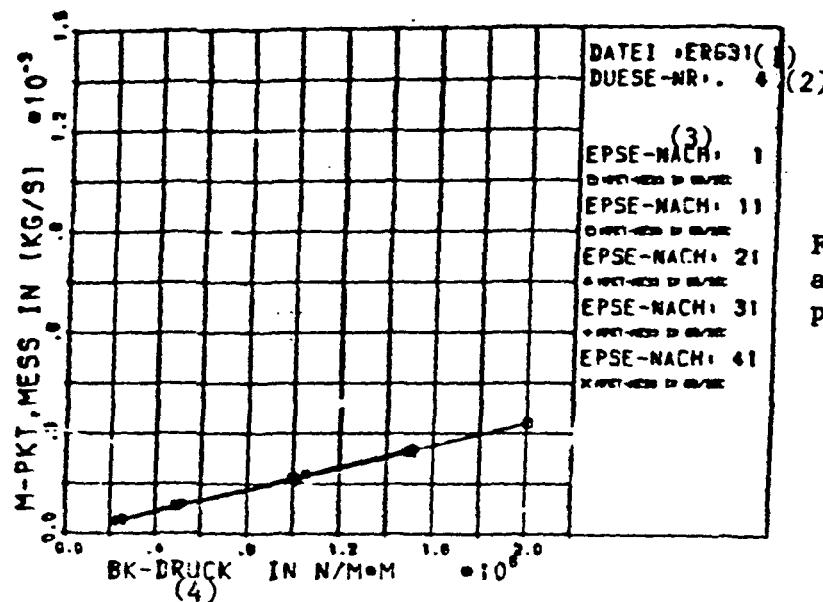
KEY   1 Data package: Result 31 2 Nozzle No. 3 from 4 Pressure 5 ε

Figures 61 to 73 show typical trends in the measurements after evaluation.

In contrast to the corresponding diagrams of the $\dot{m}$-ratio

Figure 67 Mass throughput as a function of pump throughput

Figure 68 Measured thrust as a function of measured mass throughput
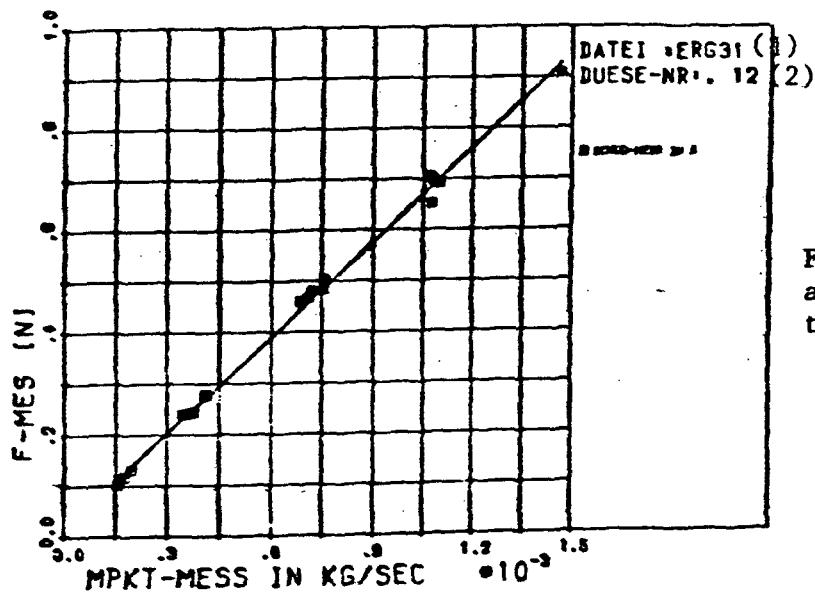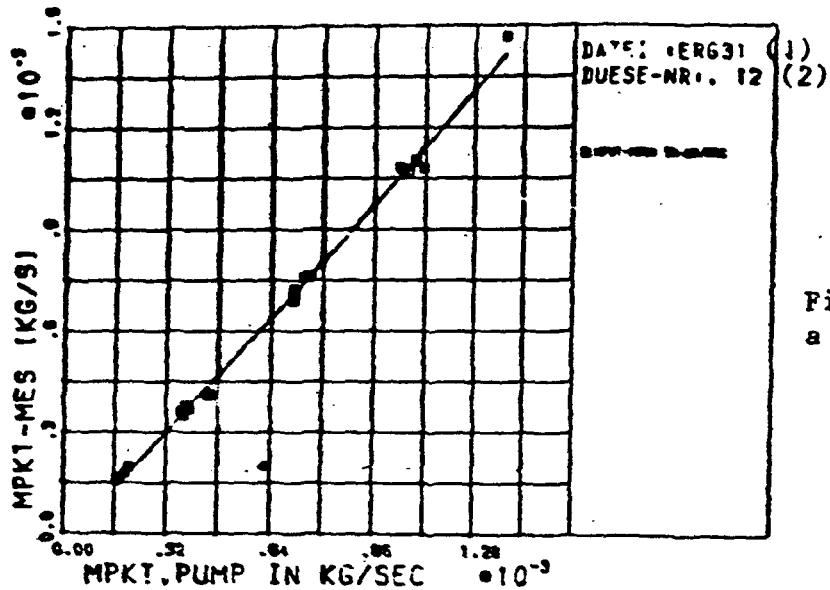
KEY   1 Data package: Result 31   2 Nozzle number

$(\dot{m}_{mess}/\dot{m}_{del,the})$, which shows good agreement between the measured and the predicted values of c_D over the entire range of ε, we can see from Figures 61 and 63 (page 112) - which describe the

115
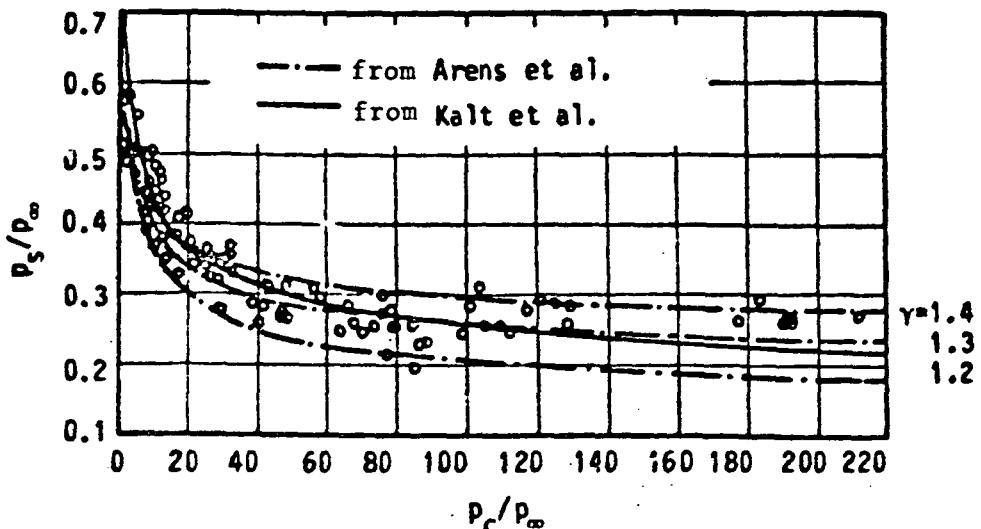
Figure 69 Flow separation ratio as a function of nozzle/environmental
pressure

thrust and impulse behavior, respectively - that there is a
certain displacement in direction > 1.0 for the higher ranges
of ε. The explanation for this is as follows: the theory of
performance prediction calculated here, at first, started from
the premise (for lack of other information), that also for the   /113
case of smaller nozzles the so-called "Summerfeld criterion"
would be valid, with respect to flow separation during over-
expansion. For the case $p_e < 0.4 \ p_\infty$, flow separation results
and → impulse losses. Since in all 12 of the micronozzles
examined the measured thrust at $\varepsilon > 100$ was greater than for
Summerfeld 0.4 (including all losses), we may infer that for
the small propulsion units under discussion here, this factor
is smaller than 0.4. This means later separation of the flow
from the wall and hence, a more widely usable ε-range. Due to
the very flexible evaluation program mentioned earlier, it is
possible to change the Summerfeld factor until good agreement
can be obtained. The results of that particular investigation
show a value of up to 0.15.
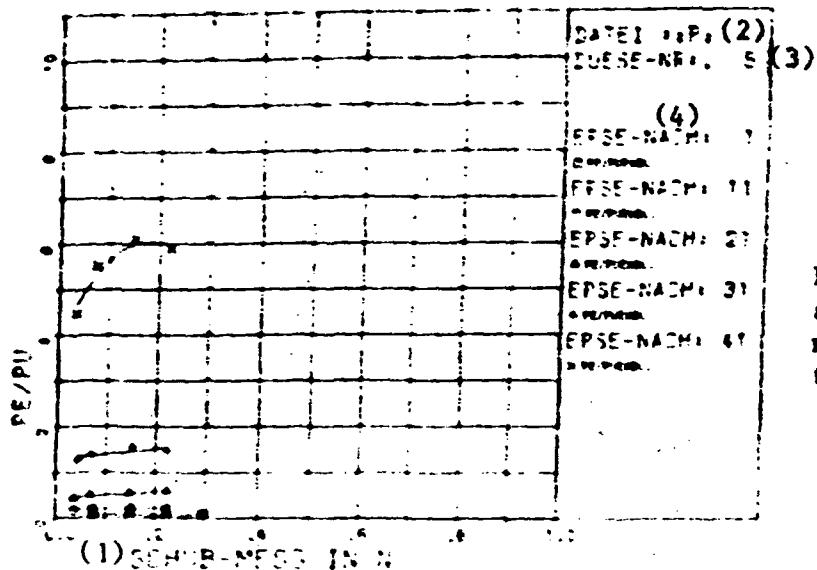
Figure 70 Ratio of end pressure to vacuum chamber environment pressure as a function of thrust, with ε as parameter
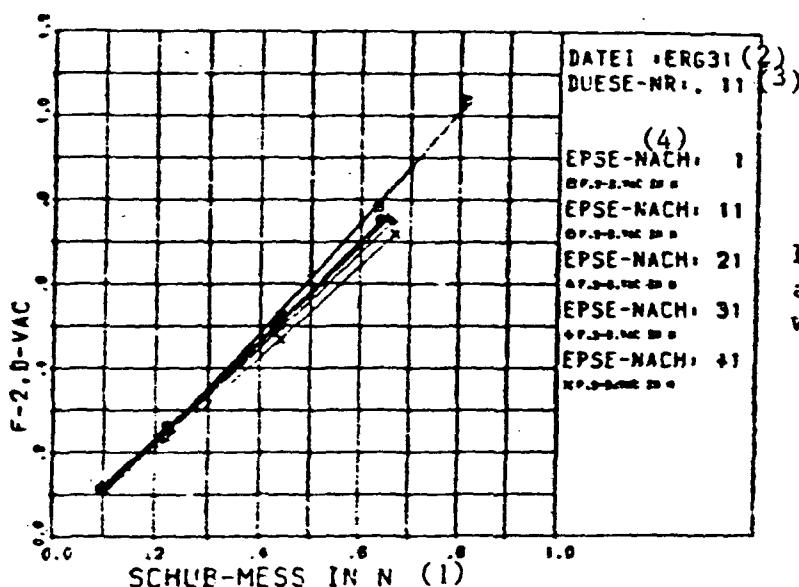
Figure 71 Measured thrust as a function of predicted thrust with ε as parameter

KEY   1 Thrust measurement   2 Data package: Result 31   3 Nozzle No. 4 from

The physical explanation of this discrpancy might be sought in that due to the greater influence of boundary layer formation in the case of extremely small propulsion unit dimensions (in contrast to full-scale propulsion units), the residual pressure

117
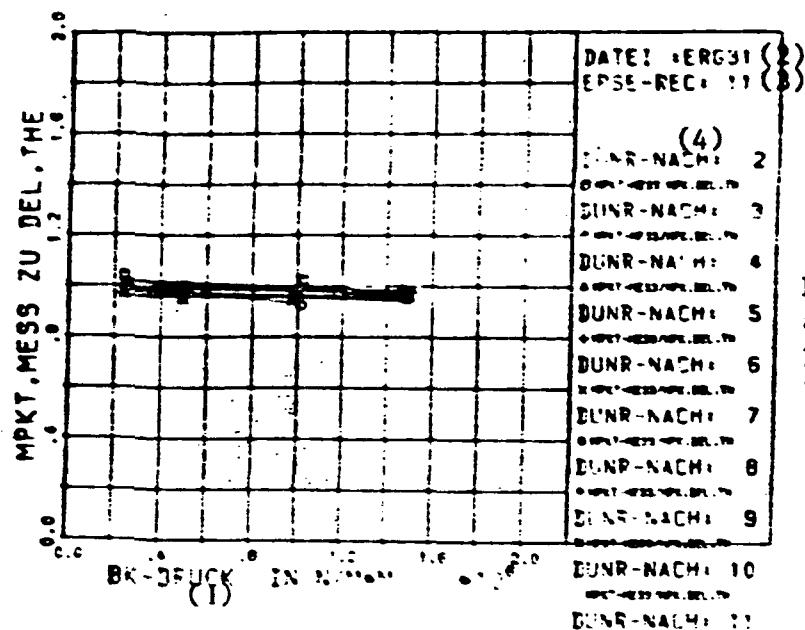
Figure 72 Throughput ratio as a function of combustion chamber pressure, with nozzle number as the parameter
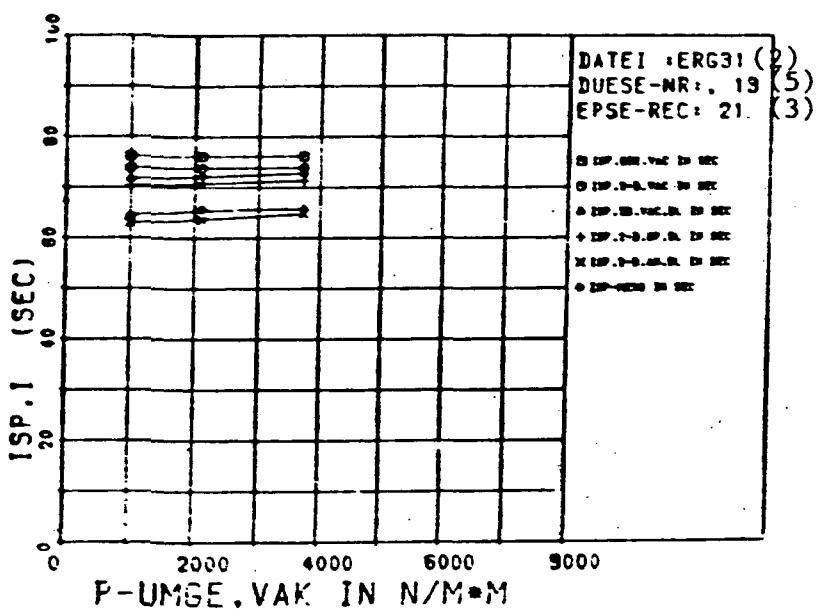
Figure 73 Specific impulse as a function of $p_{\infty,vac\ chbr}$ for the third estep

KEY   1 Pressure   2 Data package: Result 31   3 ε   4 from   5 Nozzle No.

near the wall is higher than in purely potential flow. However, since separation occurs only when the wall pressure falls considerably below the environmental pressure (precisely for large

nozzles: factor 0.4) outside of the nozzle, here this point is displaced backwards, in the direction of a larger surface ratio (see also [19,25,49,90,95,108,118,122-124,139-143,145,154,157]).

We find indications of a tendency to deviate froma factor of 0.4 already in Kalt [80]. Figure 69 (page 116) shows a decrease in the separation factor to below 0.2 for increasing pressure ratio p_c/p_∞ and decreasing isentropy exponent γ. The expression

$$\frac{p_{sep}}{p_\infty} = \frac{2}{3}\left(\frac{p_c}{p_\infty}\right)^{-0.2} \qquad (110)$$

(corresponds to the solid line, in Figure 69)

is a good approximation to the separation pressure ratios found. /114

(/116)
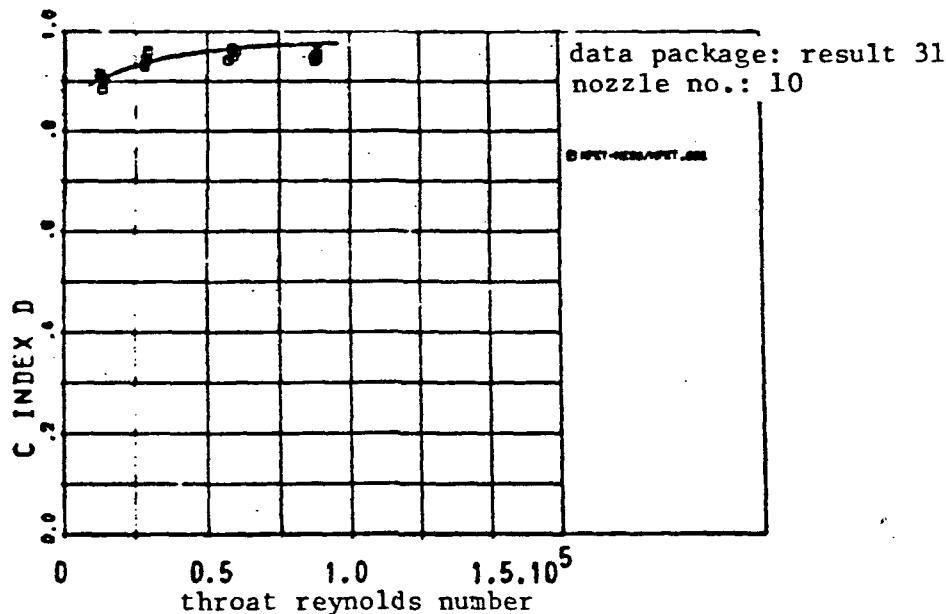
Figure 74 Throat throughput coefficient c_D as a function of the throat Reynolds number

The mass throughputs of the propulsion units and of the vacuum pumps, shown in these Figures, indicate a very precise agreement with the theory and provide a good control on the required pump constancy for different $p_{\infty,vac\ chbr}$ values. This is the only

way to verify a statement regarding stationary test conditions, as required here (and as we already assumed, at the start).

The courses of the boundary layer losses as a function of throat Reynolds number, shown in Figure 62 (page 112), are in good agreement with the theory described in section 2.5. They also make it clear that in the case of micronozzles the $\Delta \eta_{bl}$ losses have a substantially larger effect (by a factor of up to 10) than, for instance, in booster propulsion units.

Since in the determination of the theoretical/experimental characteristic magnitudes of a propulsion unit, necessary to a performance comparison, not all of them can be measured directly (for instance I_{sp}, c_{eff}, c^*, C_F), ant statement about the limits of error must involve Gauss' law of error propagation.

Since the ODE functions are already quite complicated, is is obvious that their partial derivation - necessary for Gauss' method - will become rather cumbersome. Therefore, numerical results can no longer be obtained by quick estimates, but will require EDP [electronic data processing]. On the basis of reading errors and the standard deviations of individual measurement variables, we obtain the following table of input quantities for the program (see page 122).

The subsequent Figure 75 (page 123) shows a typical printout   /118
for a completetest. In addition to the Gaussian error, in each case also the maximum error is shown that results from linear superposition. We should add that the computation time (CPU [central processing unit] time required) for the error program is of the same order of magnitude as that required for the entire boundary layer program.

TABLE 5 LISTING OF INDIVIDUAL ERRORS

$\Delta \dot{m}_{Balance}$	$\leq 0.005 \cdot 10^{-3}$ kg
Δp_{∞}	≤ 1 %
Δp_c	≤ 0.4 %
ΔT_c	≤ 0.2 k
ΔT_{∞}	≤ 0.2 k
$\Delta \gamma$	≤ 0.1 ‰
Δm_{mol}	≤ 0.03 ‰
Δm_{calib}	≤ 0.02 ‰
$\Delta \alpha_e$	$\leq 0.1°$
$\Delta \epsilon$	≤ 0.7 %
ΔL_{pipe}	≤ 0.02 %
$\Delta F_{upthrust}$	≤ 0.5 % will be compensated
$\Delta m_{Gas,}$ in the thrust frame	≤ 0.17 %
$\Delta F_{Bourdon}$	≤ 1.0 %will be compensated(171)
$\Delta E_{f(T)}$	≤ 0.4 %
ΔElectronics	≤ 0.3 % for 30 sec test duration
ΔF_{Σ}	≤ 0.9 %

*

(0)   **(1)**

(illegible)   ...IC4SUISHE?   9.2001

.... **(2)**

			"PGE8U'(4)	SE9ESSENE? DPUC4SA1R (5)	SE9ESC(4E? SCMUP (6)
(3) 145.351	204.40?	73.0''	25.500	.024	44.44?

(0) (illegible)   3.01124   **(7)** -1.49397?

(illegible) (TWIST)   9.0'''

		(8) I INVTINSWEPT	**(9)** MAX.FENLEP(2)	**(10)** EFMLE GAUSS(2)
P. = PE(.="A.?(3	PEN	919.751767	9.662771	9.77791?
(illegible) **(0)** (illegible)	4W	.760677	1.915501	1.954515
(illegible)	C0	.722009	2.337+9?	1.377654
(illegible) **(12)**	..	1.667771	.7*2362	.694909?
(illegible) **(13)**	C.I''	4''.73636'	.449630	.411354
(illegible) **(14)**	CS	691.732607	.13*254	.971952
(illegible) **(15)**	FD?	.623624	2.625130	3.131549
(illegible) **(16)**	IS*1	43.131079	7.311398	1.77?64?
(illegible) **(16)**	IS*2	43.14735?	3.226520	1.199093
(illegible) **(16)**	IS*3	43.760280	3.345501	1.846049
(illegible) **(16)**	IS*4	43.752494	3.751033	1.557659

KEY   0 Illegible   1 Test number   2 Input data   3 Surface ratio   4 Environment pressure   5 Measured throughput   6 Measured thrust   7 Error   8 Function value 9 Maximum error   10 Gaussian error   11 Mass factor   12 Thrust coefficient 13 Effective velocity   14 Characteristic velocity   15 Thrust   16 Specific impulse

Figure 75   Error protocol printout for Test No. 9.2001

The agreement between the predicted mass throughput coefficient c_D and that determined experimentally, is very satisfactory (see Figures 72 and 74). The predicted specific propulsion unit impulse data (especially $I_{sp,del}$) have been clearly confirmed by measurements, in the range of $\epsilon = 10$ to 100 and $p_c = 2$-10 bar. Beyond $\epsilon = 100$ and $p_c = 10$ bar, some uncertainty should be assumed in the overall statement, because $p_e << p_\infty$ and due to the associated flow separation effects. We expect an improvement in future experiments, using vacuum pumps of higher suction capacity and developing a new method for the direct determination of the separation site on the nozzle wall, and of the separation pressure, p_{sep}. From the point of view of engineering manipulation, the model used for boundary layer calculations may be considered satisfactory, since it allow sufficient prediction precision over a wide range of propulsion unit sizes and operating conditions. Taking into consideration the simplified equation discussed in section 2.2.10, a fast answer in regard to $\Delta\eta_{bl}$ can be obtained in subsequent applications. Further improvements seem possible, in the future, in the measurement system; in connection with improved computer programs it should become possible to further improve the reliability of the statements obtained using 2.2.10. The results obtained in the present case, for stationary operation behavior, can also be extended to pulse operation (as is often the case in attitude control tasks). The digital acquisition of measurement values and their subsequent processing and comparison with theoretical predictions represents a considerable simplification of efforts and makes it possible to eliminate large sources of error often encountered in manula calculations.

It is possible, using the nozzle manufacturing method described,
to produce not only conical nozzles with throar diameters in
the 0.1 mm diameter range, but also optimized "bell nozzles",
with specific impulses up to 2% higher. It can be shown that
their application in future satellite systems (especially if
the lifetime is > 5 years) can result in the saving of several
kg of fuel (for a 1 ton satellite mass, for instance), which in
turn increases the payload capacity. Since as of this date it
is hardly possible to further reduce the structural factors,
and a limit is going to be reached in the near future also for
specific electronic masses, a decrease in the orbit and attitude
adjustment fuel requirements is absolutely necessary.

The non-contact thrust measurement procedure here developed can
be utilized also in other areas, in which the precise measurement
of not directly accessible test objects is necessary.

The use of non-displacement weighing systems with simultaneous
prebalancing of the storage container is an area usable in measure-
ment technology (resolution: nearly six orders of magnitude of
contnuous mechanical processes), which is urgently needed to
continue development of precise throughput measurement instruments
and their calibration. By using the impulse-specific characteristic
variables determined in the precision measurements, it is possible
no only to more precisely adapt the extensive explicit computer
programs, but also those more easily handled in the rapid design
of propulsion units, providing "rule of thumb" but usable equa-
tions. In the continuation of these performance measurements
using larger vacuum pumps (higher suction capacity), these results
can be extended to large (>150) nozzle surface ratios.

The results of this effort can be used not only in space travel
per se, but conceivably also in the development of gas dynamics
laser systems or the U-235 enrichment by nozzle-separation methods.

8 REFERENCES

1 Abbett, M. J. Boundary Condition Calculation Procedure for Inviscid Supersonic Flow Fields, Cincinnati, CA 1973·

2 Adler, D., et al. The Performance of a Hydrazine Engine with an Improved Catalyst. Technion-Israel Institute of Technology, Haifa, Israel 1975

3 Back, L. H., et al. Comparison of Measured and Predicted Flows through Conical Supersonic Nozzles with Emphasis on the Transsonic Region. Jet Propulsion Laboratory (JPL), Pasadena, CA 1965

4 Back, L. H., et al. Detection of Oblique Shocks in a Nozzle with a Circular-Arc Throat. JPL, 1966

5 Back, L. H., et al. Flow Phenomena and Convective Heat Transfer in a Conical Supersonic Nozzle. JPL 1967

6 Balzer, D. L.; Brill, Y. C., Scott, W. R. and Sing, P. Y. The Monopropellant Hyrazine Reaction Control System for the RCA SATCOM Satellite. RCA Astroelectronics Division, Princeton NJ 1976

7 Barber, B. C. Flow Field Computation in the Heater and Nozzle of a Power Augmented Electrothermal Hydrazine Thruster. Farnborough 1977

8 Barber, B. C. Laminar Flowfield Computation in Axisymmetric Nozzles. Procurement Executive, Ministry of Defense, Farnborough 1977

9 Bartz, D. Turbulent Boundary Layer Heat Transfer from Rapidly Accelerating Flow of Rocket Combustion Gases. Advances in Heat Transfer, Vol. 2, Academic Press, New York 1965

10 Bassner, H., et al. Geosynchronous Spacecraft Orbit Control By an Electrical/Chemical Thruster Combination. Raumfahrt-forschung 20, 1976

11 Bellman, R. A Variational Problem with Constraints in   /122
    Dynamic Programming. J.Soc.Indust.Appl.Math., 1965

12 Bjorklund, R. A., et al. Handbook of Recommended Practices
    for the Determination of Monopropellant Rocket Engine Per-
    formance. AFRPL-TR-79-24, JPL-79-32, 1979

13 Blitzer, L., et al. Effect of Ellipticity of the Equator
    on 24-hour Nearly Circular Satellite Orbits. Space Technology
    Laboratories, Los Angeles, CA 1962

14 Bloomer, H. E., et al. Experimental Study of Effects of
    Geometric Variables on Performance of Conical Rocket Engine
    Exhaust Nozzles. NASA TN-D-846, 1961

15 Boldman, D. R., et al. Laminarization of a Turbulent Boundary
    Layer as Observed from Heat Transfer and Boundary Layer Meas-
    urements in Conical Nozzles. Lewis Research Center, Ohio,
    NASA TN-D-4788, 1968

16 Bonnet, W. S. and Evans, R. M. Boundary Layer Integral Matrix
    Procedure (BLIMP): Verification of Models. Aerotherm Final
    Report 77-239, NASA, Mountain View CA, 1977

17 Brosinger, W. Konstructive Beitraege zur Schubmessung in
    Kaltgastriebwerken [Constructive contributions to thrust meas-
    urement in cold gas propulsion units]. RT-SA 79/14, 1979

18 Callens, R. A. and Murch, C. K. Electrothermal Hydrazine
    Thruster Analyses and Performance Evaluation. NASA, Maryland/
    Redondo Neach CA, AIAA 72-1152 (1972)

19 Chank, K., Separation of Flow (Chapter 6), Catholic Univer-
    sity of America, Washington DC, 1966

20 Chrestin, D. and Ringer, K. Laser-optisches Mess-system zum
    beruehrungslosen Messen von Proben [Laser-optical measurement
    system for the non-contact measurement of specimens], TU
    Hannover, Pruef- und Mess-systeme GmbH, Mannhein (FRG)
    BMFT-FB-T-80-145, 1980

21 Clark, K. E.   Survey of Electric Propulsion Capability.
Princeton University, NJ, AIAA 74-1082 (J. Spacecraft), 1975

22 Cline, M.   A Computer Program for the Computation of Two-   /123
dimensional, Time-dependent, Inviscid Nozzle Flow. Los
Alamos Scientific Laboratory, 1977

23 Cline, M.   The Computation of Twodimensional, Viscous Nozzle
Flow. Los Alamos Scientific Laboratory, 1977

24 Cohen, C. B. and Reshotko, E.   Similar Solutions for the
Compressible Lamonar Boundary Layer with Heat Transfer and
Pressure Gradient. Lewis Flight Propulsion Laboratory, Cleve-
land OH, 1956

25 Coleman, D., et al.   Study of the Pressure Rize Across Shock
Waves Required to Separate Laminar and Turbulent Boundary
Layers, NASA TN-2770, °952

26 Crocco, L.   A Suggestion for the Numerical Solution of the
Steady Navier-Stokes Equation, Princeton University. N. J.
1976

27 Cuffel, R. F., et al.   Transsonic Flowfield ina a Supersonic
Nozzle with Small Radius of Curvature. JPL 1969

28 Dillinger, H.   Konstruktive Beitraege zur Massendurchsatz-
messung, RT-SA 80/3, 1980

29 Donnelly, R. J., et al.   Nonequilibrium Thermodynamics Vari-
ational Techniques and Stability. University of Chicago, 1965

30 Douglas, J. Jr.   On the relation between Stability and Con-
vergence in the Numerical Solution of Linear Parabolic and
Hyperbolic Differential Equations. J.Soc.Indust.Appl.Math.
1956

31 Duermeier, S.   Durflussmengenmessung mittels Messblende [The
measurement of mass throughput by means of measurement ori-
fices]. RT-SA 79/11, 1979

32 Earn, H. C. Flight Performance of a High Impulse Monopropellant Thruster. Lockheed, Sunnyvale CA, J. Spacecraft and Rockets 1976

33 Edwards, B., et al. Nonequilibrium Nozzle Flow of a Nitrogem-Hydrohen Mixture. AIAA Jouranl, 13 (1975)

34 Ehricke, K. A. Perturbations of a Satellite Orbit: /124
Orbital Precession and Satellite Motion about an Oblate
Primary. Space Flight Dynamics, Vol. I and II, P. van
Nostrand Company, New York 1959 and 1962

35 Elliott, D. G., Bartz, D. R. and Silver, S. Calculation of
Turbulent Boundary-Layer Growth and Heat Transfer in Axisymmetric Nozzles. JPL, 1963

36 Elmendorf, H. M., Sackheim, R. L. and Carlson, R. A. Development of a 5 lbf Second Generation Hydrazine Thruster. TRW
Defense and Space Systems Group, Redondo Beach, California
AIAA 76-627, 1976

37 ERNO RAUMFAHRTTECHNIK GmbH. Design, Development and Qualification of a Power Augmented Electrothermal Hydrazine
Thruster (PAEHT) for Satellite North-South Station Keeping.
Dinal Report ESTEC-Contract No. 3014, Bremen (FRG) 1978

38 Kampe de Feriet, J. Introduction to the Statistical Theory
of Turbulence (IV). J.Soc.Indust.Appl.Math. 1955

39 Fisher, D. Analytic Short Period Lunar and Solar Perturbations of Artificial Satellites. NASA Goddard Space Flight
Center, Greenbelt, MD 1972

40 Foellinger, O. Regelungstechnik [Automatic Control Technology], Elitera Verlag, Berlin 1972

41 Forsyther, G. F. Computing Constrained Minima with Lagrange
Multipliers. J.Soc.Indust.Appl.Math. 1955

42 Frankenbach, K. Theoretische Bestimmungen des Geschwindigkeitsbedarfs zur Bahn und Lageregelung eines geostationaeren
Satelliten [Theoretical determination of the velocity

requirements for orbital and attitude control of geostation-
ary satellites], TU Munich, TR-DA 80/2, 1980

43 Frick, R. H. and Garber, T. B. Perturbations of a Synchronous
    Satellite Due to Triaxiality of the Earth. The RAND Corpora-
    tion, 1962

44 Frick, R. H. Perturbations of Equatorial Satellites Due to
    Equatorial Ellipticity. NASA Technical Memorandum RM-3861,
    Santa Monica, CA 1963

45 Gehringer, W. Theoretische Untersuchungen der Grenzschicht- /125
    verluste in Lageregelungstriebwerken [Theoretical investiga-
    tion of boundary layer losses in attitude control propulsion
    units]. RT-SA 79/13, 1979

46 Gehringer, W. Theoretische Beitraege zur Leistungsvorhersage
    kleiner Raketentriebwerke [Theoretical contribution to the
    performance prediction of small rocket propulsion units].
    RT-DA 80/3, 1980

47 Gordon, S. and McBride, B. Computer Program for Calculations
    of Complex Chemical Compositions and Rocket Performance. NASA-
    SP-273, 1973

48 Grabbi, R. and Murch, C. K. High Performance Electrothermal
    Hydrazine Thruster (HIPETH) Development. AiAA 76-656, Redondo
    Beach CA 1976

49 Greenwood, T., Seymour, D., et al. Analysis of Liquid Rcoket
    Engine Exhaust Plume. Huntsville AL 1971

50 Gross, K. Personal communication. NASA-MSFC, Huntsville AL
    1978

51 Guderly, K. G. The Role of Rao's Postulate in the Optimiza-
    tion of Thrust Nozzles of a Given Length. Wright-Patterson
    Air Force Base, Ohio 1970

52 Halamek, W. Konstruktive Beitraege zur Leistungsvermessung
    kleiner Kaltgasduesen [Constructive contribution to perform-
    ance measurements in small cold gas nozzles]. RT-SA 79-10,
    1979

53 Hall, J. G. and Treanor, C. E. Nonequilibrium Effects in Supersonic Nozzle Flows. AGARD, Cornell Aeronautic Laboratory, Buffalo NY, 1967

54 Hayn, D. Optimierung einer Lavalduese durch Variation der geometrischen Abmessungen [Optimization of a Laval Nozzle by variation of its geometrical dimensions]. TU Munich, LRT-SA-16, 1976

55 Hayn, D. Constructive und experimentelle Beitraege zur Kontamination tiefgekuehlter IR-Optiken [Constructive and Experimental contributions to the contamination of deep-colled IR optics]. Chair for Thermodynamics C, TU Munich, DA 77/3, 1977

56 Hayn, D. and Schmucker, R. H. Performance of Low-thrust Attitude Control Engines, Part 1: Nozzle Flow and Performance Prediction. TU Munich, RT-TB 77/5, 1977

57 Hayn, D., Stein, U. and Schmucker, R. H. Performance of /126 Low-Thrust Attitude Control Engines, Part 2: Hydrazine Engines. Theoretical Performance and Transport Properties of Reaction Products. TU Munich, RT-TB 77/6, 1966

58 Hayn, D. Stein, U. and Schmucker, R. H. Performance of Low-Thrust Attitude Control Engines, Part 3: Power Augmented Hydrazine Engines. Performance the Thermodynamic Properties of Reaction Products. TU Munich, RT-TB 77/7, 1977

59 Hayn, D. and Schmucker, R. H. Performance of Low-Thrust Attitude Control Engines, Part 4: Correlation Equation for Experimental Boundary Layer Losses, TU Munich, RT-TB 77/4, 1977

60 Hayn, D. and Schmucker, R. H. Performance of Low-Thrust Attitude Control Engines, Part 5: Thrust Loss Determination by Test Data Correlation. TU Munich, RT-TB 78/1, 1978

61 Hayn, D. and Schmucker, R. H. Performance of Low Thrust Attitude Control Engines, Part 6: Computation of Boundary Layer Losses. TU Munich RT-TB 78/2, 1978

62 Hayn, D. and Schmucker, R. H. Leistungsvorhersage elektro-
    thermisch aufgeheizter Hydrazintriebwerke [Performanc pre-
    diction of electrochemically heated hydrazine propulsion
    units]. TU Munich, RT-KB 78/5, 1978

63 Hayn, D., Braitinger, M. amd Schmucker, R. H. Performance
    Prediction of Power Augmented Electrothermal Hydrazine
    Thrusters. TU Munich, Bayern Chemie, Muenchen-Ottobrunn,
    AIAA-78-1064, 1978

64 Hayn, D. Offenlegungsschrift DE 3029499 A1 Int.Cl. C25
    D1/10 [Disclosure document]. German Patent Office, 1982

65 Hendricks, W. L., Kurzius, S. C. and Mikatarian, R. R. Com-
    parisons Between LAMP Theoretical Predictions and Experimental
    Spectroscopic and Chemical Laser Performance. Lockheed,
    Huntsville, AL, AIAA 77-656, 1977

66 Hinz, H. K. Optimum Low-Thrust Near-Circular Orbital Trans-
    fer. Grumman Aerospace, Bethphage NY, 1963

67 Hirschmann, D., Operationsverstaerker Anwendung [Operational
    Amplifier Applications]. Franzis-verlag, Munich (FRG) 1978

68 Hoell, J. M., et al. Velocity and Thrust Measurements in /127
    a Quasi-Steady MPD-Thruster. NASA Langley Research Center,
    Hampton, VA, AiAA 70-1080, 1970

69 Hopkins, D. F. and Hill, D. E. Effect of Small Radius of
    Curvature on Transsonic Flow in Axisymmetric Nozzles. Duglas
    Aircraft Corporation, Santa Monica CA, 1966

70 Huebsch, H. P. Fortran-Programm zur Berechnung kompressibler
    laminarer und turbulenter Grenzschichten fuer beliebige Gas-
    zusammensetzungen. Teil I: Programmbeschreibung. Teil II:
    Programmlisting und Beispiele [FORTRAN program for the cal-
    culation of compressible laminar and turbulent boundary layers
    for arbitrary gas compositions. Part I: Program description.
    Part II: Program listing and examples. TU Munich, RT-SA 81/9,
    1981

71 Huff, V. N., et al. General Method and Thermodynamic Tables for Computation of Equilibrium Composition and Temperature of Chemical Reactions. NACA Report 1037, 1050

72 Huzel, D. and Hyang, D. Design of Liquid Propellant Rocket Engines. NASA SP-125, 1971

73 Hyde, J. C. and Gill, G. S. Liquid Rocket Engine Nozzles. Rockwell International, NASA Lewis Research Center, Cleveland OH, 1976

74 Inden, W. Experimentelle Ergebnisse mit Kaltgasminiaturtreib-werken im Bereich 10^{-3} bis 10^{-1} Newton fuer die Satelliten-lagerregelung [Experimental results with cold gas miniature thrusters in the range 10^{-3} to 10^{-1} Newton, for satellite attitude adjustment]. ERNO Raumfahrttechnik, 1971

75 Jaekel, E. K. Performance Characteristics of Coldgas Jets at Millinewton Thrust Level in Steadystate and Intermittent Operation. ESRO TR-14 (ESTEC), Noordwijk 1974

76 Jansson, R. E. and Edwards, I. Theoretical Performance of Ammonia, Hydrogen and Biowaste Resistojets. University Southampton, England 1972

77 Jansson, R. E., et al. Design, Development and Qualification of a Power Augmented Electrothermal Hydrazine Thruster (PAEHT) for Satellite North-South Station Keeping. Department of Chemistry, University Sounthampton, 1976

78 Juengling, J. Konstruktive Beitraege zur Leistungsmessung /128 von kleinen Laval-Duesen [Constructive contributions to the performance measurement of small Laval-nozzles]. TU Munich, RT-SA 81/1, 1981

79 Kalil, F. and Martikan, F. Derivation of Nodal Period of an Earth Satellite and Comparisons of Several First Order Secular Oblateness Results. The Martin Company, Baltimore MD 1963

80 Kalt, S., et al. Conical Rocket Nozzle Performance under Flow-Separated Conditions. J. Spacecraft and Rockets 2 (3), 1965

81 Kamel, A. and Tibbits, R., Some Useful Results on Initial
    Node Locations for Near-Equatorial Circular Satellite
    Orbits. Philco-Ford Corporation, Palo Alto CA, 1972

82 Kamel, A. et al. East-West Stationkeeping Requirements
    of Nearly Synchronous Satellites due to Earth's Triaxiality
    and Luni-Solar Effects. Philco-Ford Corporation, Palo Alto
    CA, 1973

83 Keyte, G. E., et al. The Use of Augmented Electrothermal
    Hydrazine Thrusters in Stationkeeping Application. RAE,
    Farnborough, England 1974

84 Kliegel, J. R. and Levine, J. N. Transsonic Flow in Small
    Throat Radius of Curvature Nozzles. Dynamic Science, Monrovia
    CA, 1969

85 Koelle, D. E. Entwicklungstrends kuenftiger Nachrichten-
    satelliten [Development trends in future communication satel-
    lites]. MBB Unternehmensbereich Raumfahrt, Ottobrun, DGLR
    Jahrestagung, 77-022, 1977

86 Koelle, H. H. Handbook of Astronautical Engineering. McGraw-
    Hill, New York 1961

87 Krause, H. G. L. The Secular and Periodic Perturbations of
    the Orbit of an Artificial Earth Satellite. 7th IAF Congress
    Rome (Italy) 1956

88 Kuenzly, J. D. Study of Monopropellants for Electrothermal
    Thrusters. NASA CR-144683, Redondo Beach CA 1974

89 Kuluva, N. M. and Hosack, G. A. Supersonic Nozzle Discharge   /129
    Coefficients at low Reynolds Numbers. Rocketdyne/Rockwell
    Canoga Park CA, AIAA Journal, Spet. 1971

90 Lawrence, R. A. Symmetrical and Unsymmetrical Flow Separa-
    tion in Supersonic Nozzles. Research Report No. 67-1, Southern
    Methodist University, Institute of Technology, Dallas TX, 1967

91 Lewis, C. H. Numerical Methods for Nonreacting and Chemically
    Reacting Laminar Flows - Tests and Comparisons. Blacksburg,
    VA, 1971

92 Loeb, H. et al. Betriebs- und Leistungsdaten des elektrischen Triebwerks RIT 35 [Operational and performance data for the electric thruster RIT 35]. German Air and Space Travel Congress 78-108, 1978

93 Lubowe, A. G. Orbital Behavior of Large Synchronous Satellites. Bell Telephnone Laboratories, Whippany NJ, 1966

94 Luke, Y. L. Remarks on the τ-method for the Solution of Linear Differential Equations with Rational Coefficients. J.Soc.Indust.Appl.Math., 1955

95 Mager. A. Approximate Solution of Isentropic Swirling Flow Through a Nozzle. J. American Rocket Society, 1961

96 Mangler, W. Das Impulsverfahren zur naeherungsweisen Berechnung der laminaren Grenzschicht [The impulse method for the approximate calculation of the laminar boundary layer]. Goettingen (FRG), ZAMM 5/6, 1944

97 Mangler, W., Ein Verfahren zur Berechnung der laminaren Grenz-schicht mit beliebiger Druckverteilung und Waermeuebergang fuer alle Machzahlen [A method for the calculation of the laminar boundary layer with arbitrary pressure distribution and heat transfer, for all Mach numbers]. Farnborough, Eng-land, Zeitschrift fuer Flugwissenschaften 1/2, 1956

98 MBB-UR Qualified Satellite Control Hardware: Propulsion Sys-tems - Engines - Electronics - Sensors. 1974

99 Mac Cormack, W. The Effect of Viscosity in Hypervelocity Impact Cratering. Cincinnati, 1969

100 McNally, W. J. FORTRAN Program for Calculating Compressible /130 Laminar and Turbulent Biundary Layers in Arbitrary Pressure Gradients. NASA TN-D-5681, Lewis Research Center, 1970

101 Mertel, R. Untersuchungen ueber die Tragfaehigkeit von statisch arbeitenden kreisfoermigen Luftlagern und ueber die Durchflusskennlinie von kleinen Duesendurchmessern bei hohen Druecken. Dissertation [Studies on the bearing capacity of statically operating, circular air bearings, and on the

throughput characteristic of small nozzle diamters at higher
pressures. Thesis]. TU Munich, 1977

102 Midgal, D., Klein, K. and Moretti, G. Time-Dependent Cal-
culations for Transsonic Nozzle Flow. Grumman Aerospace, 1969

103 Mikatarian, R. R. Turbulent Dissipation Effects on Chemical
Laser Performance. Lockheed, Huntsville AL, AIAA 74-547, 1974

104 Mikatarian, R. R. and McDanal, A. J. Analytical and Experi-
mental Correlation of the HF Chemical Laser Flow Data. Lock-
heed AIAA 75-39, 1975

105 Mond, M. Ein Programm zur Berechnung von zweidimensionalen
instationaeren kompressiblen Innenaustroemungen [A program
for the calculation of two-dimensional, non-stationary,
compressible internal flow]. TU Munich RT-SA 80/7 (1980)

106 Moretti, G. and Abbett, M. J. A Time-Dependent Calculational
Method for Blunt Body Flows. Westbury, NY 1966

107 Moretti, G. A Critical Analysis of Numerical Techniques:
the Piston-Driven Inviscid Flow. Polytechnical Institute of
Brooklyn, 1969

108 Murch, C. K., Broawell, J. E. and Silver, A. H. Low Thrust
Nozzle Performance. Redondo Beach CA, 1968

109 Murch, C. K. and Hunter, C. R. Electrothermal Hydrazine
Thruster Development. TRW Systems Group. Redondo Beach, CA
1972

110 Musen, P. On the Long-Period Lunar and Solar Effects on the
Motion of an Artificial Satellite. Goddard Space Flight
Center. NASA Greenbelt, MD, 1961

111 Neuwald, W. Konstruktibe Beitraege zur Entwicklung und
Herstellung eines Messwerterfassungssystems [Constructive
contributions towards the development and manufacture of
a measurement value acquisition system]. TU Munich, RT-SA
81/4, 1981

112   Noetzold, D.   Kontouroptimierung von Schubduesen mit   /131
      hochenergetischen, chemisch relaxierenden Stroemungen durch
      Anwendung des Prinzips von Bellman [Contour optimization
      for thrust nozzles using highly energetic, chemically relax-
      ing flows, by applying Bellman's Principle]. Stuttgart Uni-
      versity, 1974

113   Omori, S., Gross, K. W. and Krebsbach. A.   Supplement to
      the ICRPG Turbulent Boundary Layer Nozzle Analysis Computer
      Program. MSFC, Huntsville AL, NASA TM-X-64663, 1972

114   Oswatisch, K.   Gas Dynamik [Gas Dynamics]. Springer Verlag,
      Vienna (Austria) 1952

115   Peaceman, D. W. and Rachford, H. H., Jr.   The Numerical
      Solution of Parabolic and Elliptic Differential Equations.
      J.Soc.Indust.Appl.Math., 1955

116   Pfeffer, H. A.   The ESA Activities in the Field of Hydrazine
      Monopropellant Technology for Satellite Auxiliary Propulsion.
      ESA, Noordwijk, Netherlands, AIAA 75-1227, 1975

117   Pfister, N.   Fortranprogramm zum Berechnen kompressibler,
      laminarer und turbulenter Grenzschichten mit willkuerlichen
      Druckgradienten [FORTRAN program for the calculation of com-
      pressible, laminar and turbulent boundary layers with arbi-
      trary pressure gradients]. TU Munich, RT-SA 79/16, 1979

118   Powell, W. B.   Simplified Procedures for Correlation of Ex-
      perimentally Measured and Predicted Thrust Chamber Perform-
      ance. NASA TM-33-548, Pasadena CA, 1973

119   Promoli, E. and Schmucker, R. H.   Berechnung der zweidimen-
      sionalen reibungsfreien Duesenstroemung nach dem Charakter-
      istikenverfahren einschliesslich zugehoerigem Fortranrechen-
      programm [Calculation of two-dimensional, inviscid nozzle
      flow by the characteristics method, including the corres-
      ponding FORTRAN computer program]. TU Munich, RT-TB 80/4, 1980

120   Pugmire, T. K.   Performance and Space Application Potentials
      of Electrothermal Reactors. AVCO Systems Division, Welming-
      ton, MA, 1974

121 Pugmire, T. K., Macklis, H. and Sackheim, R. L. Application of Power Augmented Hydrazine Thrusters, TRW Defense and Space Systems Group, Redondo Beach CA, AIAA 78-1065 1978

122 Rae, W. J. Some Numerical Results on Viscous Low-Density Nozzle Flows in the Slender Channel Approximation. Cornell Aeronautic Laboratory, Buffalo NY, AIAA Journal $\underline{9}$, 1971

123 Ransom, V. H., Thompson, H. D. and Hoffman, J. D. Three- /132 dimensional Supersonic Nozzle Flowfield Calculations. Purdue University, Lafayette IN, 1970

124 Rao, G. V. R. Recent Developments in Rocket Nozzle Configurations. J. American Rocket Society, 1961

125 Ratliff, A. W. and Thoenes, J. Mixing Reacting Flows in Chemical Laser Cavities with Lateral Pressure Gradient Effects. Lockheed, AIAA 74-225, 1974

126 Reinkenhof, J. and Schmucker, R. H. Correction Factor for Heat Flux in an Expansion Nozzle. DFVLR, Lampoldshausen 1976

127 Roth, A. Beitraege zur Entwicklung und Herstellung eines Messwerterfassungssystems [Contributions to the development and manufacture of a measurement value acquisition system] TU Munich, RT-SA 81/3, 1981

128 Ruppe, H. O. Introduction to Astronautics, Vols. I and II, Academic Press, New York 1966/67

129 Ruppe, H. O. Die grenzenlose Dimension - Raumfahrt [The boundless dimension: Space travel], Vols. 1 and 2, ECON-Verlag, Dusseldorf 1980/1982

130 Sackheim et al. Performance Trends in Spacecraft Auxiliary Propulsion Systems. AIAA J. Spacecraft and Rockets $\underline{17}$ (5) 1980

131 Sagirow, P. Satellitendynamik [Satellite Dynamics], Bibliographisches Institut, BI-719/719a, 1970

132 Sansevero, V. J., et al. On-Orbit Performance of the

Hydrazine Reaction Control Subsystem for the Communications
Technology Satellite. AIAA 78-1061, 1978

133 Sauer, R. Charakteristikenverfahren fuer raeumliche achsen-
symmetrische Ueberschallstroemung [Characteristics method
for spatially axial-symmetrical supersonic flow. Aerodynamic
Institute of the Institute of Technology, Aix la Chapelle,
Yearbook 1941

134 Sauer, R. Einfuehrung in die theoretische Gasdynamic [Intro-
duction to theoretical gas dynamics]. Springer Verlag,
Berlin 1960

135 Saunders, L. M. Numerical Solution of the Flowfield in   /133
the Throat Region of a Nozzle. NASA, 1966

136 Schlichting, H. Grenzschicht-Theory [Boundary Layer Theory]
Braun-Verlag, Karlsruhe (FRG), 1965

137 Schmitz, H. D. Entwicklungstrends vom Lage und Bahnreglungs-
systemen fuer Nachrichtensatelliten der dritten Generation
[Development trends in attitude and orbit control systems
for third generation communications satellites]. ERNO Raum-
fahrtstechnik GmbH, Bremen (FRG), 1978

138 Schmucker, R. H. Hybridraketenantriebe [Hybrid rocket pro-
pulsion units]. Goldmann-Verlag, Munich (FRG) 1972

139 Schmucker, R. H. A Procedure for Calculation of Boundary
Layer Trip Protuberances in Overexpanded Nozzles. NASA-MSFC
Astronautics Laboratory, NASA TM-X-64843, 1973

140 Schmucker, R. H. Stroemungsvorgaenge beim Betrieb ueber-
expandierter Duesen chemischer Raketentriebwerke [Flow pro-
cesses during the operation of overexpanded nozzles of
chemical rocket propulsion units]. TU Munich, LRT-TB-10,
1973   7

141 Schmucekr, R. H. Stroemungsvorgaenge beim Betrieb ueber-
expandierter Duesen chemischer Raketentriebwerke [Flow pro-
cesses during the operation of everexpanded nozzles of
chemical rocket propulsion units] - Seitenkraefte durch

unsymmetrische Abloesung [Lateral forces due to asymmet-
rical flow separation]. TU Munich, LRT-TB-10, 1973

142 Schmucker, R. H. Stroemungsvorgange beim Betrieb ueber-
expandierter Duesen chemischer Raketentriebwerke - Methoden
zur gezielten Stroemungsabloesung und Seitenkraftverring-
erung [Flow processes during the operation of everexpanded
nozzles of chemical rocket propulsion units - Methods for
the purposive flow separation and lateral force reduction].
TU Munich, LRT-TB-11, 1973

143 Schmucker, R. H. Side Loads and Their Reduction in Liquid
Rocket Engines (Int. Astronautical Congress, Baku USSR).
TU Munich, LRT-TB-14, 1973

144 Schmucker, R. H. Zweidimensionales Stroemungsfeld einer
achsensymmetrischen Lavalduese, ALGOL Rechenprogramm und
Bedienungsanleitungen [Twodimensional Flow Field of an Axi-
symmetrical Laval nozzle, ALGOL computer Program and Opera-
ting Instructions]. TU Munich, LRT-TB 22

145 Schmucker, R. H. Status of Flow Separation Prediction in
Liquid Propellant Rocket Nozzles, NASA TM-X-64890, 1974

146 Schrenk, O. Eine anschauliche Herleitung des Impulssatzes /134
der Grenzschichttheory [A descriptive derivation of the
impulse theorem in the boundary layer theory]. ZFW 1/2, 1956

147 Schulze, N. Lavalduesenstroemung: Vergleichende Betrach-
tungen eindimensionaler und zweidimensionaler Berechnungs-
methoden [Laval nozzle flow: comparative considerations on
unidimensional and twodimensional calculation methods].
Federal Armed Forces University, Munich, 1976

148 Schwende, M. A. Development of a Bipropellant Orbit Injec-
tion and Attitude COntrol System. MBB-UR, AIAA 78-1092, 1978

149 Schwende, M. A. Praezisions-Zweistoff-Antrieb fur Raumfahrt-
anwendungen [Precision two-component propulsion units for
space travel applications]. MBB, Unternehmungsbereich Raum-
fahrt, Conference TU Munich, 1978

150 Shapiro, A. H. The Dynamics and Thermodynamics of Compressible Fluid Flow, Vols. I and II. Ronal Press Company, New York, 1953/1954

151 Sharp, G. R. Thruster Subsystems Module for Solar Electric Propulsion. NASA Lewis Rsearch Center, Cleveland OH, AIAA 75-406, 1975

152 Shrivastava, S. K. Orbital Perturbations and Stationkeeping of Communications Satellites. Indian Institute of Sciennce, Bangalore, 1978

153 Sinha P., et al. Flowfield Analysis of Plumes of Two-Dimensional Underexpanded Jets by a Time-Dependent Method. New York University, Bronx NY, 1971

154 Spisz, E. W., et al. Thrust Coefficients of Low-Thrust Nozzles. NASA TN-D-3056, 1965

155 Steitz, W. and Tokar, G. Auslegung und Konstruktion einer Vakuumschubmessanlage in 1-Newton Bereich [Design and manufacture of a vacuum thrust installation in the 1-Newton range]. TU Munich, RT-SA 78/5, 1978

156 Stott, D. The Electrothermal Hydrazine Thruster. Hawker-Siddeley Dynamics, Ltd., 25th IAF Congress, Amsterdam 1974

157 Sutton, G. P. and Ross, D. M. Rocket Propulsion Elements John Wiley, New York, 1976

158 Thoenes, J. and Ratliff, A. W. Chemical Laser Oscillator /135 Model. Lockheed, AIAA 74-644, 1973

159 Thompson, P. A. Eine Realgas-Version der gasdynamischen Formeln von de St. Venant und Wantzel [A Real Gas Version of de St, Venant and Wantzel's Gas Dynamics Equations]. MPI fuer Stroemungsforschung, Goettingen 1978

160 Thompson, P. A. and Sullivan, D. A. Exact and Approximate Equations for Real Fluid Isentropic Flow. MPI fuer Stroemungsforschung. Goettingen, 1978

161 Truckenbrodt, E., Stroemungsmechanik [Flow Mechanics], Springer-Verlag, 1968

162 TRW Systems Monopropellant Systems. Redondo Beach CA 1972

163 Tuzinsky, W. Kryo-Kontamination und Thermalhaushalt eines ballongetragenen Infrarot-Telekops [Cryo-contamination and thermal balance of a ballon-carried infrared telescope] Thesis. TU Munich, 1979

164 Wagner, C. A. The Drift of a 24-Hour Equatorial Satellite Due to and Earth Gravity Field through 4th Order. Goddard Space Flight Center, Greenbelt MD, NASA TN-D-2103, 1964

165 Waltz, A. Stroemungs- und Temperaturgrenzschichten [Flow and Temperature Boundary Layers]. Verlag G. Braun, Karlsruhe (FRG), 1966

166 White, B. D. Velocity Required for Intercept with Perturbations. Agoura CA, 1979

167 Whitefield, D. L. and Lewis, C. H. Boundary-Layer Analysis of Low-Density Nozzles, Including Displacement, Slip and Transverse Curvature. Arnold Air Force Station, TN/Virginia Polytechnic Institute, Blacksburg VA, 1970

168 Wich, G. Konstruktion und Entwicklung zur Leistungsmessung von Miniaturtriebwerken [Design and Development to Performance Measurements of Miniature Propulsion Units]. TU Munich RT-SA 79/5, 1979

169 Wich, J. Konstructive Beitraege zur Schubmessung von Mikrotriebwerken [Constructive Contributions ro Thrust Measurements on Micropropulsion Units]. TU Munich, RT-SA 81/16, 1981

170 Winkler, W. and Grigull, U. Waermeuebergang turbulenter   /136 kompressibler Grenzschichtstroemungen mit starken negativen Druckgradienten (Waermeuebergang in einer Lavalduese) [Heat Transmission of Turbulent, Compressible Boundary Layer Flow with Strong Negative Pressure Gradients (Heat transfer in a Laval Nozzle)]. TU Munich, 1977

171 Wuest, W. Die Berechnung von Bourdonfedern [The Calculation of Bourdon Tubes], VDI Forschungsheft 489, 1962

172 Young, D. Iterative Methods for Solving Partial Differential Equations of Elliptic Type. Harvard University 1950

173 Zee, C.-H. Effects of Earth Oblateness and Equator Ellipticity on a Synchronous Satellite. Grumman Aerospace Corp., New York, 1970

174 Zee, C.-H. Effects of the Sun and the Moon on a Near-Equatorial Synchronous Satellite. Grumman Aerospace Corp., New York, 1971

175 Zehle, H. Rumpfmanuskript Raummechanik; Fassung SS 1973 [Basic manuscript on Space Mechanics; version SS 1973], TU Berlin

176 Zenger, K. Konstruktive und experimentelle Beitraege zur Massendurchsatzmessung von kleinen Lavalduese [Constructive and experimental contributions on the mass throughput measurement in small Laval nozzles]. TU Munich (FRG), RT-SA 80/22, 1980

177 Zielband, H. and Parkinson, R. C. Heat Transfer in Rocket Engines. AGARD-AG-148-71, 1971

178 Zirpel, M. Operationsverstaerker [Operational amplifiers] Franzis-Verlag, Munich (FRG) 1977

179 Zucrow, M. J. and Hoffman, J. D. Gasdynamics, Vols. I and II. J. Wiley, New York, 1976/1977

COMMERCIAL CATALOGS   /137

180 Analog Devices, 1980
181 Buerklin-Elektronik, 1980
182 Conrad-Elektronik, 1980
183 Hottinger Baldwin, 1980
184 Laser Optronic, 1980
185 Leybold Heraeus, 1980
186 Physik Instrumente, 1980
187 Spindler & Hoyer, 1980
188 United Technologies, 1980

9.1   Design of the cantilever beam
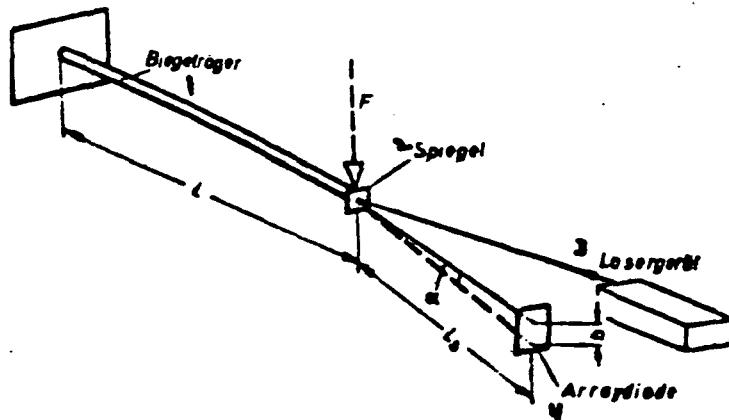
KEY   1 Bending carrier   2 Mirror   3 Laser instrument   4 Array diode

Figure 76   Arrangement of the bending carrier with mirror, laser instrument
            and array diode

Specified quantities:

$G \quad = 15 \text{ N (weight of nozzle and harness)}$

$L_{max} = 250 \text{ mm}$

$L_s \quad = 0.5 \text{ m}$

$S \quad = 1 \text{ N (thrust)}$

$a \quad = 10 \text{ μm}$

$b_{max} = 1.5 \text{ mm}$

$\Delta S \quad = 10^{-2} \text{ N}$

For the bending line $w(x)$ we have, for small deformations with
a line load $\underline{q}$ due to the carrier's own weight:

$$E I w^{IV} = - q$$

/139

Following quadrouple integration

$$E I w = - \frac{1}{24} x^4 q - \frac{1}{6} x^3 F + \frac{1}{2} x^2 C_1 + C_2 x + C_3$$

With the boundary conditions

$$w(0) = w'(0) = w''(L) = 0$$

the integration constants become

$$C_3 = 0$$
$$C_2 = 0$$
$$C_1 = L F + \frac{1}{2} qL^2$$

We then have, for the bending line and its inclination

$$w(x) = \frac{1}{E I}\left[-\frac{1}{24} qx^4 - \frac{1}{6} x^3 F + \frac{1}{2} x^2 (L F + \frac{1}{2} qL^2) \right]$$

$$w'(x) = \frac{1}{E I}\left[-\frac{1}{6} qx^3 - \frac{1}{2} x^2 F + x (L F + \frac{L^2}{2} q) \right]$$

At the location of the mirror, $x = L$ and we have

$$w'(L) = \frac{F L^2}{2 E I}$$

(here we assume $q = 0$ and $F = G + S$)

The angular change of the reflected laser beam will be twice the change of the slope in the bending line, due to the laws of reflection:

$$\alpha = 2\left[w'(L)_{G+S} - w'(L)_G \right] \cong \frac{L^2}{E I} \cdot S$$

The path $\underline{b}$ traversed by the laser beam's point of impact on the array diode is

$$b = L_s \tan \alpha$$

145

Since $\underline{b}$ is very small compared to L_s and therefore α is very small, $\tan \alpha = \alpha$ and hence,

$$b = \frac{L_s L^2}{E I} \cdot S$$

The carrier must satisfy the following conditions:

1) The deformation must be large enough to attain the desired precision

$$a < \frac{L_s L^2}{E I} \cdot \Delta S$$

2) The deformation must be smaller than the size of the array diode allows

$$b_{max} > \frac{L_s L^2}{E I} S_{max}$$

3) No plastic deformation of the tube under thrust or its own weight, respectively

$$\sigma < \sigma_{zul}$$

From 1) and 2):

$$\frac{b_{max}}{S_{max} L_s} > \frac{L^2}{E I} > \frac{a}{\Delta S L_s}$$

with

$$\sigma_{max} = \frac{M_{max}}{W_b} = \frac{F L}{W_b} \qquad \text{and} \qquad I_{Kreisrohr} \approx \pi s r_m^3$$

(Kreisrohr = circular tube)

146

or

$$w_b \approx \pi s r_m^2 \qquad \text{as well as}$$

(Anticipating the result)

("Stahl" = steel)

$L \qquad = 200 \text{ mm}$

$\Delta S \qquad = 10^{-2} \text{ N}$

$L_s \qquad = 0,5 \text{ m}$

$\sigma_s \qquad = \dfrac{N}{mm^2}$

we obtain: $I \simeq 100 \text{ mm}^4$; if a 1 mm wall thickness is chosen, then

$$r_m = \sqrt[3]{\frac{I}{\pi s}} \approx 3,2 \text{ mm}$$

$$\sigma_{max} < \frac{F L}{\sqrt[3]{\pi s \ S_{max}^2 \ L^4 \ L_s^2 \ b_{max}^{-2} \ E^{-2}}} \sim L^{1/3}$$

or

$$\sigma_{max} < C \cdot E^{2/3}$$

From this we realize that L must be chosen as large as possible /142 (within the vacuum chamber).

For the certainty against plastic deformation we have

$$S_{plast} > \frac{\sigma_s}{\sigma_{max}}$$

With the design magnitudes listed above, S_{plast} becomes $\simeq 2.7$, i.e., no weight compensation is necessary!

147

Of the materials examined, steel had the best qualities, in addition to its preference because of ready availability and simple processing (can be welded).

The nozzle holding flange welded to the free end of the cantilever beam (tube), including p_c tube (see Figure 77, page 150) remains clearly below 15 N, in weight, in the final design; hence the design calculations remain valid (with respect to S_{plast}). In addition the resolution of the array diode system could be considerably increased (see section 3.2.3).

Einzelheit X

p_c-Druck-
messbohrung

Schnitt A-B
3

4 Triebwerk

5 Aufnahme der p_c-Mess-
röhre

7 N_2-Zuleitung

6 Teil 3 Ansicht Y

8 Teil 2

9

10 Bohrungen dienen der Arretierung
des Kragbalkens während des Trieb-
werkaustausches
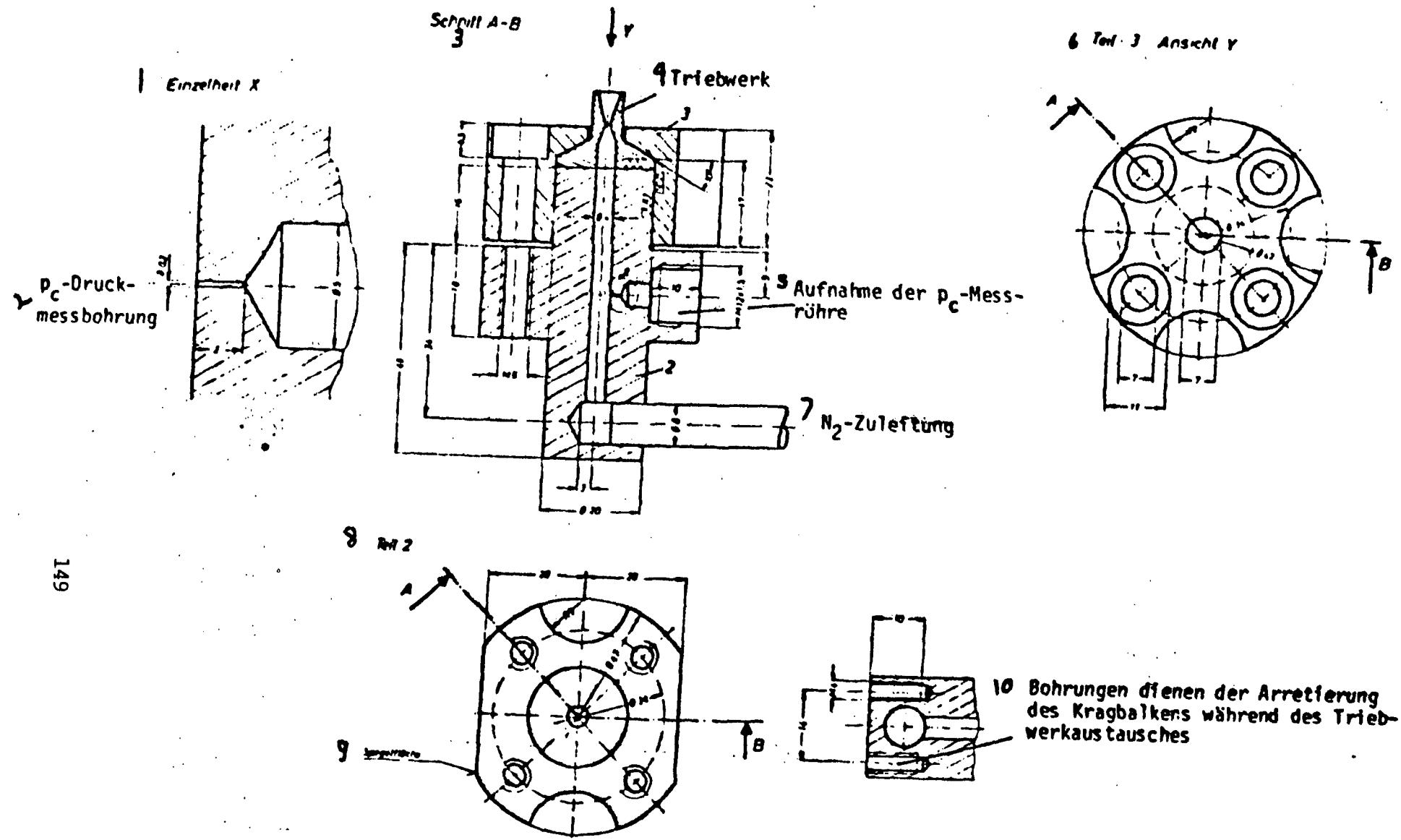
KEY   1 Detail X   2 p_c pressure measurement boring   3 Section   4 Thruster   5 p_c meas. tube receptacle
6 Part 3 View Y   7 N_2 inflow line   8 Part 2   9 [Illeg.]   10 Boreholes serve to arrest the cantilevered
beam during the propulsion unit exchanges

Figure 77   Thruster receiving flange
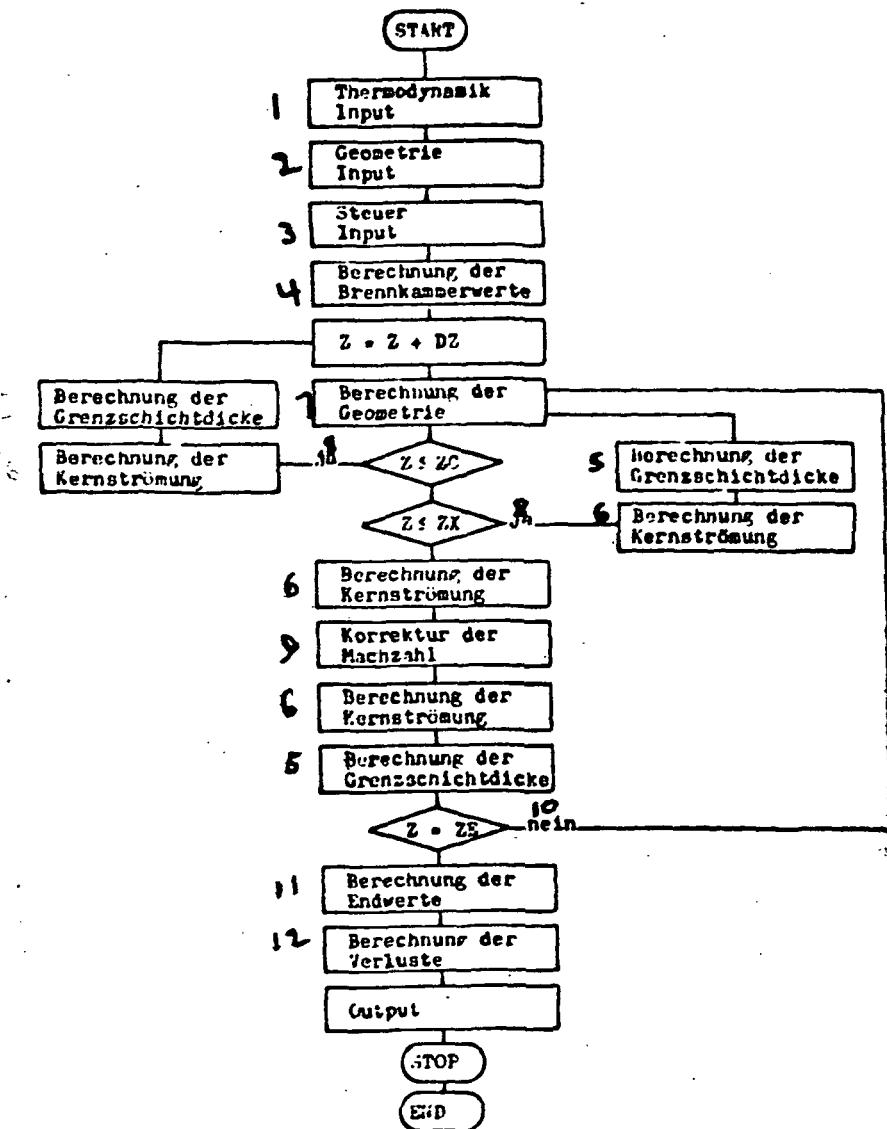
KEY   1 Thermodynamic input   2 Geometry input   3 Control input   4 Calculation of combustion chamber values   5 Boundary layer thickness calculations 6 Core flow calculations   7 Geometry calculations   8 yes   9 Mach number correction 10   No   11 End value calculation   12 Loss calculations

Figure 78   Computer program flow diagram

9.3 Test protocol

Versuch : 5 / 10 / 01											Datum : 22.4.1981	
3 $T_{Flasche}$		**4** $T_{c,Brennkam.}$		**5** $T_{\infty,Vakuum}$		**6** $T_{0,Raum}$		**7** T_{Waage}		**8** $T_{N2-Kamma}$		
(mV)	[K]	(mV)	[K]	(mV)	[K]	(mV)	[K]	(mV)	[K]	(mV)	[K]	
0.2894	291.2	0.2998	296.5	0.2921	294.6	0.2947	293.9	0.2918	300.3	0.2884	291.6	
P_0	P_c	P_∞ (+6 V !)		$\Delta\dot{m}_{vor}$	$\Delta\dot{m}_{nach}$	$\dot{m}_{Vers.}$	$\dot{m}_{korr.}$	$F_{o,v,DVM}$	$F_{o,n,DVM}$	F_{DVM}	$F_{i/0}$	
[Torr]	[bar]	[V]	[Torr]	[g/s]	[g/s]	[g/s]	[g/s]	(mV)	(mV)	(mV)	(mV)	
714.8	10.055	8.21	9.04	-0.0025	0.0015	0.2161	0.2156	+37.14	+37.19	+67.23	+67.22	
ΔF	Schub	ε	r_t	Bk_1	Bk_ϕ	α_e	$dF/d(mV)$	Bemerkungen :		$P_{c,v}$ = 0.1002		
(mV)	[g]	[-]	[mm]	[mm]	[mm]	[°]	(g/mV)			$P_{c,n}$ = 0.1001		
										$P_{c,m}$ = 0.2007		
30.067	16.071	194.0656	0.176	5.0	4.0	15.0	0.5357	$P_{c,A/D}$=0.2009				

KEY   1 Test No. 2 Date 3 Bottle 4 Combustion chamber 5 Vacuum 6 Room 7 Balance
8 N_2 chamber 9 Thrust 10 Remarks

Figure 79 Example of test protocol (5.1001)

9.4 Cost analysis (180 + 188)

Balance and printer (Mettler)	DM 7,700
Laser 101P (Laser Optronic)	1,400
Components for measurement data acquisition	600 (approx)
P_c measurement tube and amplifier	450
PIN-LSC array diode system (incl. evaluation syst.)	1,800
Neutral wedge	190
Micrometer drive motor	80
Vacuum minimotor	140
Temperature measurement sensors (6)	180
Molding knife for nozzle manufacture	1,500
Nozzle manufacture (galvanoplastics)	280
N_2- 2 liter bottle (2)	300
1 transfer tube (special manufacture)	210
Small parts (approx.)	500
Working gas (approx.)	600
Documentation (approx.)	700
Total (approx.)	DM 16,630*

* Of this, approximately DM 11,500 are outside financing

████████   Born in ████████████████ as son of civil engineer
Erich Hayn and his wife Ruth, born ██████

06-03-70   Graduation from the mathematical-scientific high school
           Max von Laue, Koblenz

07-01-70/ Basic training for tank grenadier at Unna, Westphalia
09-30-70

10-01-70/ Special Weapons Technical Batallion, Koblenz (service
10-31-70   grade: Ppal. lance Corporal)

10-21-71   Matriculation at TU Munich, Technical Area Mechanical
           Engineering

07-01-72   Start of collaboration in the WARR [wissenschaftliche
           Arbeitsgemeinschaft Raketentechnik und Raumfahrt =
           scientitif study group for rocket engineering and space
           flight]

04-23-74   Preliminary diploma in Mechanical Engineering

1974-1976 Technical spokesman for aeronautic and astronautical
           technologies

1974-1976 WARR director; development of a liquid rocket thruster

07-23-76   Married Ilsa Isabella Schgaguler

03-31-77   Concludes thesis at Chair C, Thermodynamics, on a laser
           interferometric measurement method

05-10-77   Receives degree in Aeronautical and Astronautical Engi-
           neering

since   Employed at the Chair for Astronautical Engineering of
06-01-77   TU Munich

06-01-77/ Collaboration with the ERNO company, Bremen (FRG), in
07-01-78   an ESA project for the PAEHT thruster

09-12-77   Decoration by the management of the DGLR [Deutsche
           Gesellschaft fuer Luft- und Raumfahrt = German Society
           for Aero and Astronautics] for the above activity, as
           Director of the WARR